SIMULATION OF SEISMIC REAL AND VIRTUAL DATA USING THE 3D FINITE-DIFFERENCE TECHNIQUE AND REPRESENTATION THEOREM

A Dissertation

by

XIUJUN YANG

Submitted to the Office of Graduate Studies of
Texas A&M University
in partial fulfillment of the requirements for the degree of

DOCTOR OF PHILOSOPHY

August 2008

Major Subject: Geophysics

SIMULATION OF SEISMIC REAL AND VIRTUAL DATA USING THE 3D FINITE-DIFFERENCE TECHNIQUE AND REPRESENTATION THEOREM

A Dissertation

by

XIUJUN YANG

Submitted to the Office of Graduate Studies of
Texas A&M University
in partial fulfillment of the requirements for the degree of

DOCTOR OF PHILOSOPHY

Approved by:

Chair of Committee,	Luc T. Ikelle
Committee Members,	Daulat D. Mamora
	Yuefeng Sun
	Hongbin Zhan
Head of Department,	Andreas Kronenberg

August 2008

Major Subject: Geophysics

ABSTRACT

Simulation of Seismic Real and Virtual Data Using the 3D Finite-Difference Technique and Representation Theorem. (August 2008)

Xiujun Yang, B.S., University of Science and Technology of China;

M.S., Indiana University

Chair of Advisory Committee: Dr. Luc T. Ikelle

Seismic modeling is a technique for simulating wave propagation through the subsurface. For a given geological model, seismic modeling allows us to generate snapshots of wave propagation and synthetic data. In my dissertation, for real seismic events I have chosen to implement the finite-difference modeling technique. When adequate discretization in space and time is possible, the finite-difference technique is by far one of the most accurate tools for simulating elastic-wave propagation through complex geological models.

In recent years, a significant amount of work has been done in our group using 2D finite-difference modeling. For complex salt structures which exploration and production industries meet today, 2D finite-difference modeling is not sufficient to study subsalt imaging or the demultiple of subsalt models. That is why I have developed a 3D finite-difference modeling code.

One of the key challenges that I have met in developing the 3D finite-difference code is to adapt the absorbing boundary conditions. Absorbing boundary conditions are needed to describe the infinite geological models by limited computing domain. I have validated the 3D finite-difference code by comparing its results with analytic solutions. I have used 3D finite-difference program to generate data corresponding to 3D complex model which describes salt and subsalt structures of Gulf of Mexico. The resulting data include reflections, diffractions and other scattering phenomena. I have also used finite-difference program in anisotropic context to show that we can

effectively predict shear-wave splitting and triplication in the data.

There are new sets of events that are not directly recorded in seismic data, they have been called virtual events. These events are turning to be as important as real events in modern data processing. Therefore we also have to learn how to model them. Unfortunately, they cannot yet be modeled directly from finite-difference. Here I will describe how to model these events by using cross correlation type representation theorem. As illustration of how important of virtual events for seismic data processing, I also described an internal multiple attenuation technique which utilized virtual events.

ACKNOWLEDGMENTS

I would like to sincerely thank my academic advisor, Dr. Luc Ikelle for his teaching, mentoring, guidance and support that have been fundamental to my growth as a professional geophysicist. In particularly I would like to thank him for helping me define my goal and for providing insight into the research problem.

I would also like to express my gratitude to my committee members Dr. Hongbin Zhan, Dr. Daulat Mamora, and Dr. Yuefeng Sun for their support and helpful comments.

I express my special thanks to all the CASP members who helped me, as well as all the sponsors of the CASP project that made this and other research possible.

Finally, to my husband Shuqian Dong for his support and patience during this long journey.

TABLE OF CONTENTS

Page

CHAPTER Page

Page

LIST OF FIGURES

FIGURE Page

FIGURE Page

FIGURE Page

CHAPTER I

INTRODUCTION

THE FINITE-DIFFERENCE TECHNIQUE

Finite difference is a technique which allows us to numerically solve partial differential equations. Wave equations that we will describe in chapter II are examples of partial differential equations which can be solved by the finite-difference technique. This is a very powerful technique with broad scientific applications, including classical mechanics, aero-dynamics, meteorology, geophysics, etc.

Since the 1970s, earthquake seismologists and petroleum seismologists have made finite-difference solutions to wave equations as an integral part of the investigations of earth responses. In petroleum seismology in particular, finite difference is a well-established tool today for testing algorithms and for modeling the seismic data.

The ultimate aim of developing the finite-difference technique is to produce a 3D version code, but so far this is not well developed. The main reason that 3D finite-difference has left behind is tremendous complexities involved with 3D geologies that modern exploration and production industries are looking for. Obviously the computing cost involved in 3D finite-difference technique is the key force impeding its use. The availability of affordable high-performance computers and the development of user-friendly interfaces will probably make the 3D finite-difference technique a more widely used tool in scientific and industrial community in coming decades. So I believe that the prototype of the 3D finite-difference code developed in this dissertation will help to accelerate this process.

One of the interesting things about finite-difference modeling is that we can input parameters just as we do in real acquisitions in the field. Similarly, we can

---

This dissertation follows the style and format of Geophysics.

output all the quantities recorded in seismic acquisition today, and much more. More specifically, the user interface in my code consists of three sets of parameters: the geological model that we would like to use to generate data; source and receiver positions, type of source used to generate seismic wave (explosion, drop weight, etc.); the physical quantities recorded (pressure, particle velocity).

With finite-difference modeling we can go beyond standard data acquisition. It is a very instructive tool to understand how waves propagate underground. Therefore I have a structured interface in my code such that one can output snapshots of wave propagation in addition to seismic data. In chapter II, I will show several examples of these snapshots and indicate how easily they can be used to describe very complex phenomena, such as shear-wave splitting and triplication. Let me emphasize that with the finite-difference technique, we can explain these phenomena without the complex mathematics generally associated with them.

The difference between my 3D finite-difference modeling and real acquisition is that the numerical instability may cause finite-difference modeling code to fail. This numerical instability can be overcome by making sure that we discretize the medium such that we have at least five grid points per wavelet and by using a time step which is much smaller than the 2 ms, sample interval used in standard data acquisition. In chapter II we describe the mathematics of this condition in detail.

Another important difference between finite-difference modeling and real data acquisition is that geological model in finite-difference modeling is limited in space. Therefore we have to introduce an absorbing boundary condition to avoid the numerical reflections from the artificial boundaries. We have used a technique proposed by (Cerjan et al., 1985) to overcome this problem. We will describe this technique and its application to 3D finite-difference modeling in chapter II in detail.

VIRTUAL EVENTS

Modern exploration targets resource below the salt bodies and the basalt layers. Seismic energy below these bodies is generally very weak and often invisible to seismic data acquired by conventional data acquisition. One of the emerging ideas is that we like to put sources and receivers deep in the ground rather than on the surface. Unfortunately, we cannot do this physically, so we are trying to construct a new set of events from seismic data which allows us to simulate the source and receivers inside the ground. These events are now called virtual events. Figure 1 shows an example of virtual events. Notice that the last bend in this event does not follow the standard interpretation of Snell's law; moreover the simulated wave moves back in time. In chapter IV, we will show some snapshots illustrating this phenomenon.

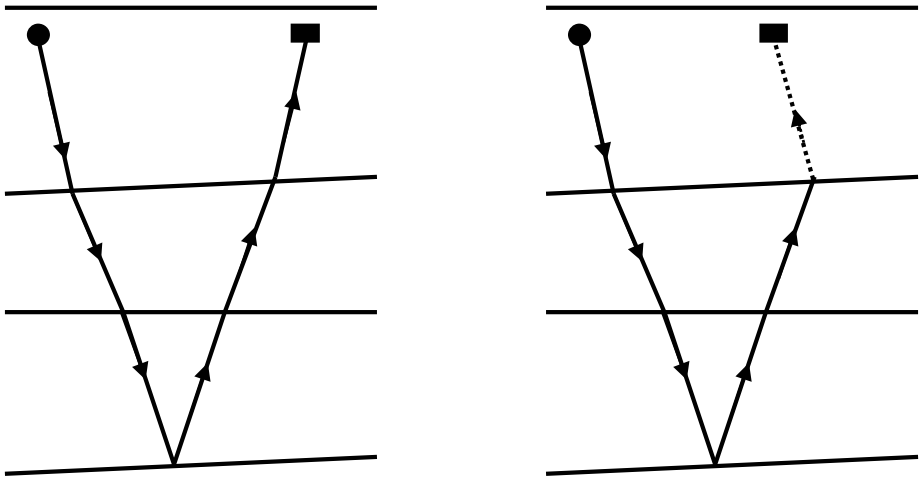

Fig. 1. Examples of seismic real and virtual events. In these scattering diagrams, the process of wave propagation begins on the left and ends on the right. The solid line represents waves traveling forward in time, and the dotted line represents waves traveling backward in time. (left) a seismic real event, (right) a seismic virtual event. Note that the last bend in the virtual event does not follow the standard interpretation of Snell's law.

As all data acquired, in seismic data processing we would like to have the capability to simulate them for the same reason we simulate finite-difference data. Therefore it is important to figure out a way to simulate virtual events. Some of my colleagues

in the CASP project are looking at ways to model virtual events using finite-difference modeling by creating anisotropic materials for which the group direction and phase direction of wave propagation are very different. In this dissertation, I have selected to use the representation theorem for simulating virtual events. In chapter V we will describe the mathematics as well as provide numerical examples using the representation theorem, more specifically crosscorrelation-type representation theorem. We will also discuss the multiple-attenuation approach using virtual events. In the same chapter, examples are shown to illustrate that virtual events are useful in data processing.

DISSERTATION STRUCTURE

This dissertation includes modeling seismic real events by using a 3D staggered-grid finite-difference technique and modeling seismic virtual events by using the crosscorrelation type representation theorem. Each chapter contains part of the results of the topics.

Chapter II provides a detailed derivation of the 3D staggered-grid finite-difference technique. Free-surface boundary and absorbing boundary condition are applied in the 3D finite-difference modeling program. Stability and grid dispersion are also discussed. The 3D finite-difference modeling code is verified with analytical solution in homogeneous medium.

Chapter III provides additional numerical examples to verify the 3D finite-difference modeling results. The basic physics principles are used to analyze the modeling results.

Chapter IV shows two of the practical applications of the finite-difference modeling tool. First, the application of the finite-difference modeling in improving the illumination of a complex salt model will be shown. Then modeling shear-waves splitting and triplication in anisotropic medium using the 3D finite-difference technique

will be followed.

Chapter V introduces a new set of events that are not directly recorded in seismic data, they have been called virtual events. The virtual events can be modeled by using the crosscorrelation type representation theorem. In this chapter an internal multiple attenuation technique that utilizes virtual events will also be described, internal multiple attenuation results using a 2D synthetic data will also be shown.

Chapter VI summarizes the conclusions of the dissertation work.

CHAPTER II

3D FINITE-DIFFERENCE FORMULATION

My goal in this chapter is to provide a detailed derivation of the 3D finite-difference technique, which I have used to develop the code in Appendix A. I will start by recalling the basic equations of wave propagation; then I will discuss how the partial derivatives of these equations can be approximated by finite-difference technique. I will introduce the notion of the staggered grid, which I have used for discretizing media parameters, stresses, strains and particle velocities. I will provide mathematical formulae for choosing the grid size and time step which ensures the numerical stability of my code. I will also discuss boundary conditions. I will validate these various derivations by comparing my results to an analytic solution when possible, or through basic physics principles.

BASIC WAVE EQUATIONS

The wave propagation is governed by Newton's law of motion and by stress-strain relations.

Newton's law of motion

Newton's law of motion can be written as follows:

$$\rho(\mathbf{x})\frac{\partial v_i(\mathbf{x},t)}{\partial t} = \frac{\partial \tau_{ij}(\mathbf{x},t)}{\partial x_j} + F_i(\mathbf{x},t) \qquad i,j = 1,2,3. \tag{2.1}$$

where $\rho = \rho(\mathbf{x})$ is the density, $\mathbf{v} = v_i(\mathbf{x},t)$ are the components of particle velocity, $\mathbf{x} = [x_1, x_2, x_3]^T$ is the position, and t is the time. The repeated subscript indicates summation. The left-hand side of the equation describes the mass multiplied by acceleration, and the right-hand side of the equation show internal forces and external forces. More precisely, the internal forces are the stresses $\boldsymbol{\tau} = \tau_{ij}(\mathbf{x},t)$, and external

forces are the body force $\mathbf{F} = F_i(\mathbf{x}, t)$.

Stress-strain relations

The stress-strain relationship is given by

$$\tau_{ij}(\mathbf{x}, t) = c_{ijkl}(\mathbf{x}) e_{kl}(\mathbf{x}, t) + I_{ij}(\mathbf{x}, t) \qquad i, j, k, l = 1, 2, 3. \tag{2.2}$$

where tensor $\mathbf{I} = I_{ij}(\mathbf{x}, t)$ represents external stresses, and $\mathbf{e} = e_{ij}(\mathbf{x}, t)$ represents strain, which is related to velocity as follows:

$$\frac{\partial e_{ij}(\mathbf{x}, t)}{\partial t} = \frac{1}{2}\left(\frac{\partial v_i(\mathbf{x}, t)}{\partial x_j} + \frac{\partial v_j(\mathbf{x}, t)}{\partial x_i}\right) \qquad i, j = 1, 2, 3. \tag{2.3}$$

$c_{ijkl} = c_{ijkl}(\mathbf{x})$ is the stiffness tensor. It is a $3 \times 3 \times 3 \times 3$ fourth-rank tensor. In isotropic case the stiffness tensor can be written as

$$c_{ijkl}(\mathbf{x}) = \lambda(\mathbf{x}) \delta_{ij} \delta_{kl} + \mu(\mathbf{x}) \left(\delta_{ik} \delta_{jl} + \delta_{il} \delta_{jk}\right) \qquad i, j, k, l = 1, 2, 3. \tag{2.4}$$

where $\lambda = \lambda(\mathbf{x})$, $\mu = \mu(\mathbf{x})$ are the Lamé parameters, and δ_{ij} is the Kronecker delta function:

$$\delta_{ij} = \begin{cases} 0 & \text{for } i = j \\ 1 & \text{for } i \neq j \end{cases} \qquad ij = 1, 2, 3. \tag{2.5}$$

Because of the symmetry of stress ($\tau_{ij} = \tau_{ji}$) and the symmetry of strain ($e_{ij} = e_{ji}$) , only six of these equations (2.2) are independent. It is common to write the stiffness tensor in the so-called compact notation by using

$$11 \to 1 \quad 22 \to 2 \quad 33 \to 3 \quad 32 = 23 \to 4 \quad 31 = 13 \to 5 \quad 21 = 12 \to 6 \,, \tag{2.6}$$

so that the $3 \times 3 \times 3 \times 3$ tensor c_{ijkl} can be represented by a 6×6 matrix.

In the isotropic case, by using the abbreviated notations, the stiffness tensor can

be expressed in matrix form as follows:

$$[C] = \begin{bmatrix} \lambda+2\mu & \lambda & \lambda & 0 & 0 & 0 \\ \lambda & \lambda+2\mu & \lambda & 0 & 0 & 0 \\ \lambda & \lambda & \lambda+2\mu & 0 & 0 & 0 \\ 0 & 0 & 0 & \mu & 0 & 0 \\ 0 & 0 & 0 & 0 & \mu & 0 \\ 0 & 0 & 0 & 0 & 0 & \mu \end{bmatrix} . \tag{2.7}$$

INITIAL AND BOUNDARY CONDITIONS

To completely describe the problem of modeling wave propagation, we need to specify initial and boundary conditions for wave equations in (2.1) and (2.2). The initial conditions are that the stress and particle-velocity fields and their time derivatives are null before the seismic source is fired. These can be written as

$$\begin{aligned} v_i = \partial_t v_i = 0, \qquad & t \leq 0, \qquad i = 1,2,3. \\ \tau_{ij} = \partial_t \tau_{ij} = 0, \qquad & t \leq 0, \qquad i,j = 1,2,3. \end{aligned} \tag{2.8}$$

The boundary conditions for the problem of modeling seismic wave propagation are the free-surface boundaries: air-solid in the case of land seismic and air-water in the case of marine seismic. Here we assume a flat free-surface boundary at a depth of $z = 0$. Then stresses are zero at the free surface.

$$\tau_{zz}\,(x,y,z=0,t) = \tau_{xz}\,(x,y,z=0,t) = \tau_{yz}\,(x,y,z=0,t) = 0\ . \tag{2.9}$$

MODELING IN PETROLEUM SEISMOLOGY

Sources and data

Wave equations in (2.1) and (2.2) consist of a system of first-order differential equations. We can group these equations in a second-order differential equation by substi-

tuting equation (2.2) into equation (2.1), and we arrive at this (Ikelle and Amundson, 2005):

$$\rho(\mathbf{x})\frac{\partial^2 u_i(\mathbf{x},t)}{\partial t^2} - \frac{\partial}{\partial x_j}\left[c_{ijkl}(\mathbf{x})\frac{\partial u_k(\mathbf{x},t)}{\partial x_l}\right] = F_i(\mathbf{x},t) + \frac{\partial I_{ij}(\mathbf{x},t)}{\partial x_j} \qquad i,j,k,l = 1,2,3. \tag{2.10}$$

where $\mathbf{F} = F_i(\mathbf{x},t)$ and $\mathbf{I} = I_{ij}(\mathbf{x},t)$ are the source terms, and $\mathbf{u} = u_i(\mathbf{x},t)$ is particle displacement, which is related to velocity as follows:

$$v_i(\mathbf{x},t) = \frac{\partial u_i(\mathbf{x},t)}{\partial t} \qquad i = 1,2,3. \tag{2.11}$$

In finite-difference modeling we also alter the system of first-order differential equations because it involves only first-order derivatives and does not explicitly include derivatives respective to media parameters. The latter is particularly important because the media we are dealing with in geology are discontinuous, whereas the other quantities involved in equation (2.1) and (2.2) are continuous. Notice that we also assume that the rock is linearly elastic. That is, the model in the subsurface can be isotropic, anisotropic, and heterogeneous. However, we did not include nonlinear elastic properties or attenuation.

Seismic modeling consists of solving wave equations for particle velocities, stresses, and strains for a given system of sources $\{F_i, I_{ij}\}$ and geological model c_{ijkl}. In real seismic acquisition, we assume that the sources are point sources. Therefore they can be defined as $\phi(t)\delta(\mathbf{x}-\mathbf{x_s})$, where $\mathbf{x_s}$ is the point-source location, and $\phi(t)$ is the source signature on various polarization. In land seismic, the weigh drop for example, can be defined as follows:

$$\begin{cases} I_{ij} = 0 \qquad \text{for} \quad i,j = 1,2,3 \\ F_1 = F_2 = 0 \\ F_3(\mathbf{x},t) = \phi(t)\delta(\mathbf{x}-\mathbf{x_s}) \end{cases} . \tag{2.12}$$

In towed-streamer acquisition, the explosive source can be defined as follows:

$$\mathbf{I} = \begin{bmatrix} -P & 0 & 0 \\ 0 & -P & 0 \\ 0 & 0 & -P \end{bmatrix}, \qquad F_1 = F_2 = F_3 = 0 \ , \tag{2.13}$$

with

$$P = \phi(t)\delta(\mathbf{x} - \mathbf{x_s}) \ . \tag{2.14}$$

We also used point receivers, which sense pressure especially in marine and particle velocities in both marine and land. Other characteristic of wave equations stresses, and strain are not yet commonly recorded in seismic acquisition.

Importance of seismic modeling

With seismic modeling we can go beyond standard data acquisition. Seismic modeling allows us to generate snapshots in addition to seismic data. These snapshots represent one of the fundamental ways of understanding the information contained in seismic data. With snapshots we can easily identify P-wave and S-wave events that can be used to differentiate between solids and fluids. In chapter III, we will show several examples of these snapshots and indicate how easily they can be used to describe very complex phenomena such as shear-wave splitting and triplication.

The importance of seismic modeling is not limited to a basic understanding of seismic data; it can also be used to design surveys, with the objective of illuminating the particular area of the subsurface for which conventional designs may not be adequate. The data generated by numerical modeling can also be used to validate new imaging techniques (as the answer is known) and to benchmark existing algorithms. Seismic interpreters in the field also use seismic modeling data to validate the geological description of the subsurface, derived from the real data.

SOLVING WAVE EQUATIONS BY THE STAGGERED-GRID FINITE-DIFFERENCE TECHNIQUE

Our goal in this section is to numerically solve the wave equations in (2.1) and (2.2). To facilitate the derivations, we will here limit ourselves to the isotropic case. The extension to anisotropic case is straightforward, the only difference is that we have to deal with longer stress-strain relationship equations. We will describe our finite-difference technique for solving the following wave equations.

Wave equations

(i) Newton's law of motion:

$$\begin{aligned}
\rho(\mathbf{x})\partial_t v_x(\mathbf{x},t) &= \{\partial_x \tau_{xx}(\mathbf{x},t) + \partial_y \tau_{xy}(\mathbf{x},t) + \partial_z \tau_{xz}(\mathbf{x},t)\} + f_x(\mathbf{x},t)\ , \\
\rho(\mathbf{x})\partial_t v_y(\mathbf{x},t) &= \{\partial_x \tau_{xy}(\mathbf{x},t) + \partial_y \tau_{yy}(\mathbf{x},t) + \partial_z \tau_{yz}(\mathbf{x},t)\} + f_y(\mathbf{x},t)\ , \\
\rho(\mathbf{x})\partial_t v_z(\mathbf{x},t) &= \{\partial_x \tau_{xz}(\mathbf{x},t) + \partial_y \tau_{yz}(\mathbf{x},t) + \partial_z \tau_{zz}(\mathbf{x},t)\} + f_z(\mathbf{x},t)\ . \qquad (2.15)
\end{aligned}$$

where ρ is the density, $\mathbf{v} = (v_x, v_y, v_z)$ are the components of particle velocity, $\mathbf{x} = [x, y, z]^T$ is the position, t is the time, $\boldsymbol{\tau} = (\tau_{xx}, \tau_{yy}, \tau_{zz}, \tau_{xz}, \tau_{xy})$ are stresses, and $\mathbf{f} = (f_x, f_y, f_z)$ are the external forces. The symbols $\partial_x,\ \partial_y,\ \partial_z$, and ∂_t are shorthand representations of the differential operators $\partial/\partial_x,\ \partial/\partial_y,\ \partial/\partial_z$, and ∂/∂_t.

(ii) The stress-strain relations:

$$\begin{aligned}
\partial_t \tau_{xx}(\mathbf{x},t) &= [\lambda(\mathbf{x}) + 2\mu(\mathbf{x})]\, \partial_x v_x(\mathbf{x},t) + \lambda(\mathbf{x})\, [\partial_y v_y(\mathbf{x},t) + \partial_z v_z(\mathbf{x},t)] + I_{xx}(\mathbf{x},t)\ , \\
\partial_t \tau_{yy}(\mathbf{x},t) &= [\lambda(\mathbf{x}) + 2\mu(\mathbf{x})]\, \partial_y v_y(\mathbf{x},t) + \lambda(\mathbf{x})\, [\partial_x v_x(\mathbf{x},t) + \partial_z v_z(\mathbf{x},t)] + I_{yy}(\mathbf{x},t)\ , \\
\partial_t \tau_{zz}(\mathbf{x},t) &= [\lambda(\mathbf{x}) + 2\mu(\mathbf{x})]\, \partial_z v_z(\mathbf{x},t) + \lambda(\mathbf{x})\, [\partial_x v_x(\mathbf{x},t) + \partial_y v_y(\mathbf{x},t)] + I_{zz}(\mathbf{x},t)\ , \\
\partial_t \tau_{yz}(\mathbf{x},t) &= \mu(\mathbf{x})\, [\partial_z v_y(\mathbf{x},t) + \partial_y v_z(\mathbf{x},t)] + I_{yz}(\mathbf{x},t)\ , \\
\partial_t \tau_{xz}(\mathbf{x},t) &= \mu(\mathbf{x})\, [\partial_z v_x(\mathbf{x},t) + \partial_x v_z(\mathbf{x},t)] + I_{xz}(\mathbf{x},t)\ , \\
\partial_t \tau_{xy}(\mathbf{x},t) &= \mu(\mathbf{x})\, [\partial_y v_x(\mathbf{x},t) + \partial_x v_y(\mathbf{x},t)] + I_{xy}(\mathbf{x},t)\ , \qquad (2.16)
\end{aligned}$$

where λ and μ are the Lamé parameters, and $\mathbf{I} = (I_{xx}, I_{yy}, I_{zz}, I_{yz}, I_{xz}, I_{xy})$ are the external stresses.

Discretization

In order to numerically solve the system of first-order differential equations in (2.15) and (2.16), the first step in the finite-difference technique is to describe the geological model and quantities that characterize the wavefield. That is, the media parameters, the particle velocities, and the stresses. We need to define them both in time and space in order to describe these quantities. We can use the following discretization:

$$\begin{aligned} t &= n\Delta t, \qquad n = 0, 1, 2, \ldots, N, \\ x &= i\Delta x, \qquad i = 0, 1, 2, \ldots, I, \\ y &= j\Delta x, \qquad j = 0, 1, 2, \ldots, J, \\ z &= k\Delta x, \qquad k = 0, 1, 2, \ldots, K, \end{aligned} \tag{2.17}$$

where Δt is the time interval that is the so-called time step, Δx is the spacing interval that is the so-called grid size. The total time length for the data t is defined as $t = N\Delta t$. The total size of the geological model is defined as $X = I\Delta x$, $Y = J\Delta x$, $Z = K\Delta x$. Notice that we have used a cubic grid in this discretization because the spacing intervals in X, Y, and Z axis are the same; however X, Y, and Z can all be different.

We will call this discretization in equation (2.17) reference grid. This terminology will be used to distinguish the gridding in (2.17) with the staggered-grid technique that we will introduce later.

By using the discretization in equation (2.17), we can describe the geological model and quantities that characterize the wavefield in equations (2.1) and (2.2) as

a function of the indices n, i, j, and k. Those quantities can be written as

$$\begin{aligned}
\lambda(x,y,z) &= \lambda\left(i\Delta x, j\Delta y, k\Delta z\right) = \left[\lambda\right]_{i,j,k} \ , \\
\mu(x,y,z) &= \mu\left(i\Delta x, j\Delta y, k\Delta z\right) = \left[\mu\right]_{i,j,k} \ , \\
\rho(x,y,z) &= \rho\left(i\Delta x, j\Delta y, k\Delta z\right) = \left[\rho\right]_{i,j,k} \ ,
\end{aligned} \tag{2.18}$$

for the media parameters in the geological model, and

$$\begin{aligned}
v_x(x,y,z,t) &= v_x\left(i\Delta x, j\Delta y, k\Delta z, n\Delta t\right) = \left[v_x\right]^n_{i,j,k} \ , \\
v_y(x,y,z,t) &= v_y\left(i\Delta x, j\Delta y, k\Delta z, n\Delta t\right) = \left[v_y\right]^n_{i,j,k} \ , \\
v_z(x,y,z,t) &= v_z\left(i\Delta x, j\Delta y, k\Delta z, n\Delta t\right) = \left[v_z\right]^n_{i,j,k} \ , \\
\tau_{xx}(x,y,z,t) &= \tau_{xx}\left(i\Delta x, j\Delta y, k\Delta z, n\Delta t\right) = \left[\tau_{xx}\right]^n_{i,j,k} \ , \\
\tau_{yy}(x,y,z,t) &= \tau_{yy}\left(i\Delta x, j\Delta y, k\Delta z, n\Delta t\right) = \left[\tau_{xy}\right]^n_{i,j,k} \ , \\
\tau_{zz}(x,y,z,t) &= \tau_{zz}\left(i\Delta x, j\Delta y, k\Delta z, n\Delta t\right) = \left[\tau_{zz}\right]^n_{i,j,k} \ , \\
\tau_{yz}(x,y,z,t) &= \tau_{yz}\left(i\Delta x, j\Delta y, k\Delta z, n\Delta t\right) = \left[\tau_{yz}\right]^n_{i,j,k} \ , \\
\tau_{xz}(x,y,z,t) &= \tau_{xz}\left(i\Delta x, j\Delta y, k\Delta z, n\Delta t\right) = \left[\tau_{xz}\right]^n_{i,j,k} \ , \\
\tau_{xy}(x,y,z,t) &= \tau_{xy}\left(i\Delta x, j\Delta y, k\Delta z, n\Delta t\right) = \left[\tau_{xy}\right]^n_{i,j,k} \ ,
\end{aligned} \tag{2.19}$$

for the quantities that describe the wavefield.

Unfortunately, the calculation of the first-order derivatives of these quantities are required to solve the wave equations in (2.15) and (2.16). There are two sets of variables in the wave equations in (2.15) and (2.16); the wavefield variables, which are the particle velocity $\mathbf{v}$ and the stress $\boldsymbol{\tau}$; and the media parameters which are Lamé parameters λ, μ, and density ρ. The differences between the two sets of variables are that the wavefield variables are continuous and that the media variables are not necessarily continuous. We need to find a discretization formulation in which only the derivatives of wavefield variables are needed and the derivatives to media variables are avoided.

The staggered-grid technique

An alternative discretization approach proposed by (Madariaga, 1976) is to use a staggered-grid technique. In this technique, not all quantities in the wave equations are defined at the reference gird; some are defined at half a grid point off the reference grid, say, $x = \left(i \pm \frac{1}{2}\right) \Delta x$ instead of $x = i\Delta x$. Figure 2 illustrates the layout of the wavefield quantities and the media parameters in equations (2.15) and (2.16) on the staggered-grid. In this example, the horizontal component of particle velocity v_x is defined at the reference grid, shear stress, τ_{yz}, is defined at half a grid off the reference grids, the normal stresses τ_{xx}, τ_{yy}, τ_{zz} are defined at half a grid off the reference grid on the X axis. Notice that normal stresses, mass density, and the Lamé parameters are located at the same points.

On the basis of the staggered-grid discretization technique described in Figure 2, the media parameters and wavefield quantities in equations (2.15) and (2.16) can be defined at the discrete space-time domain as follows:

$$\begin{aligned}
\lambda(x,y,z) =& \lambda\left[(i+\frac{1}{2})\Delta x, j\Delta x, k\Delta x\right] = [\lambda]_{i+1/2,j,k} \ , \\
\mu(x,y,z) =& \mu\left[(i+\frac{1}{2})\Delta x, j\Delta x, k\Delta x\right] = [\mu]_{i+1/2,j,k} \ , \\
\rho(x,y,z) =& \rho\left[(i+\frac{1}{2})\Delta x, j\Delta x, k\Delta x\right] = [\rho]_{i+1/2,j,k} \ .
\end{aligned} \tag{2.20}$$

for the media parameters,

$$\begin{aligned}
v_x(x,y,z,t) &= v_x\left[i\Delta x, j\Delta x, k\Delta x, (n+\frac{1}{2})\Delta t\right] = [v_x]^{n+1/2}_{i,j,k} \ , \\
v_y(x,y,z,t) &= v_y\left[(i+\frac{1}{2})\Delta x, (j+\frac{1}{2})\Delta x, k\Delta x, (n+\frac{1}{2})\Delta t\right] = [v_y]^{n+1/2}_{i+1/2,j+1/2,k} \ , \\
v_z(x,y,z,t) &= v_z\left[(i+\frac{1}{2})\Delta x, j\Delta x, (k+\frac{1}{2})\Delta x, (n+\frac{1}{2})\Delta t\right] = [v_z]^{n+1/2}_{i+1/2,j,k+1/2} \ .
\end{aligned} \tag{2.21}$$

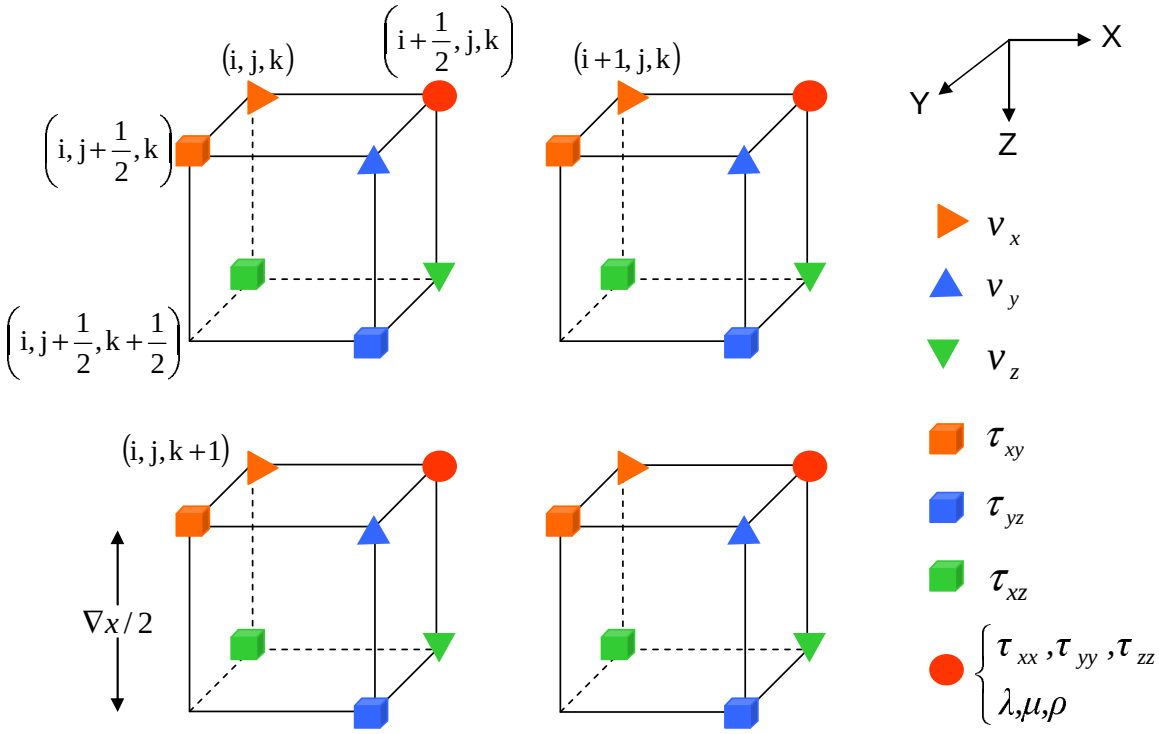

Fig. 2. The staggered-grid formulation for 3D elastic finite-difference modeling. This staggered-grid formulation is adapted from (Ikelle and Amundson, 2005). The indices (i, j, k) represent values at spatial coordinates (x, y, z) and the grid spacing Δx is defined as the length between the centers of two adjacent grids. The wavefield variables and media parameters are defined at a specific grid in a unit cell, and the model space is made up of a series of repeated unit cells that occupy a 3D space. Not all quantities are defined at the reference grid. The horizontal component of particle velocity v_x is defined at the reference grid, shear stress τ_{yz} is defined at half a grid off the reference grids, and the normal stresses τ_{xx}, τ_{yy}, τ_{zz} are defined at half a grid off the reference grid on the X axis. Notice that normal stresses, mass density, and the Lamé parameters are located at the same points.

for the velocities,

$$\begin{aligned}
\tau_{pp}(x,y,z,t) =& \tau_{pp}\left[(i+\frac{1}{2})\Delta x, j\Delta x, k\Delta x, n\Delta t\right] = [\tau_{pp}]^n_{i+1/2,j,k} \ , \\
\tau_{yz}(x,y,z,t) =& \tau_{yz}\left[(i+\frac{1}{2})\Delta x, (j+\frac{1}{2})\Delta x, (k+\frac{1}{2})\Delta x, n\Delta t\right] = [\tau_{yz}]^n_{i+1/2,j+1/2,k+1/2} \ , \\
\tau_{xz}(x,y,z,t) =& \tau_{xz}\left[i\Delta x, j\Delta x, (k+\frac{1}{2})\Delta x, n\Delta t\right] = [\tau_{xz}]^n_{i,j,k+1/2} \ , \\
\tau_{xy}(x,y,z,t) =& \tau_{xy}\left[i\Delta x, (j+\frac{1}{2})\Delta x, k\Delta x, n\Delta t\right] = [\tau_{xy}]^n_{i,j+1/2,k} \ . \qquad (2.22)
\end{aligned}$$

for the stresses with $p = x, y, z$. In the equations above, the superscripts refer to the time index, and the subscripts refer to the spatial indices (see Figure 2).

Note that the choice we made here in Figure 2 is not unique. By choosing one set of quantities for the reference grid, equations (2.15) and (2.16) automatically impose the grid positions of the other quantities as the derivatives must be assigned with the positions in the grids. We provided alternative choices of stagger-grid formulation in Appendix B.

Finite-difference operators

Before we provide the final equations of the staggered-grid technique, let us recall some basic formulae for computing first-order derivatives. The first-order derivatives in the finite-difference technique are based on an approximation of the Taylor-series. The derivatives can be approximated by a second-order operator, a fourth-order operator or even a higher-order operator by (Abramowitz and Stegun, 1964). The higher the order, the longer the difference operator becomes, the more accurate the actual first-order derivatives, and the more expensive the computation will be.

For an arbitrary α, the first-order derivatives of a function $g(x)$ can be approxi-

mated by a three-point formula given by (Abramowitz and Stegun, 1964):

$$\begin{aligned}\partial_x g\left(x+\alpha\Delta x\right) =& \frac{1}{\Delta x}\Bigg[\left(\alpha-\frac{1}{2}\right) g\left(x-\Delta x\right) - 2\alpha g\left(x\right) \\ &+ \left(\alpha+\frac{1}{2}\right) g\left(x+\Delta x\right)\Bigg] + \ldots \end{aligned} \tag{2.23}$$

The evaluated equation (2.23) at $\alpha = 0$ gives us the derivatives at the reference grid:

$$\partial_x g\left(x\right) \approx \frac{1}{\Delta x}\left[-\frac{1}{2} g\left(x-\Delta x\right) + \frac{1}{2} g\left(x+\Delta x\right)\right] , \tag{2.24}$$

Similarly, the evaluated equation (2.23) at $\alpha = 1/2$ gives us:

$$\partial_x g\left(x+\frac{1}{2}\Delta x\right) \approx \frac{1}{\Delta x}\left[-g\left(x\right) + g\left(x+\Delta x\right)\right] . \tag{2.25}$$

Note that we can also obtain the derivatives in the reference grid by shifting equation (2.25) a half grid-point in the negative direction giving us

$$\partial_x g\left(x\right) \approx \frac{1}{\Delta x}\left[-g\left(x-\frac{1}{2}\Delta x\right) + g\left(x+\frac{1}{2}\Delta x\right)\right] . \tag{2.26}$$

Equation (2.26) is the second-order operator for approximating the first order derivatives. Actually, our time derivatives are based on the second-order approximation in equation (2.26).

For spatial derivatives, we will use the fourth-order approximation. Similarly, we can obtain the fourth-order approximation by using a five point formula given by (Abramowitz and Stegun, 1964). For an arbitrary α, the first order derivatives of a function $g(x)$ can be approximated by a five-point formula:

$$\begin{aligned}\partial_x g(x+\alpha\Delta x) =& \frac{1}{\Delta x}\Bigg[\frac{1}{12}(2\alpha^3 - 3\alpha^2 - \alpha + 1) g(x+\Delta x) \\ &- \frac{1}{6}(4\alpha^3 - 3\alpha^2 - 8\alpha + 4) g(x-\Delta x) + \frac{1}{2}(2\alpha^3 - 5\alpha) g(x) \\ &- \frac{1}{6}(4\alpha^3 - 3\alpha^2 - 8\alpha + 4) g(x+\Delta x) \\ &+ \frac{1}{12}(2\alpha^3 - 3\alpha^2 - \alpha + 1) g(x+2\Delta x)\Bigg] + \ldots . \end{aligned} \tag{2.27}$$

The evaluated equation (2.23) at $\alpha = 0$ gives us the derivatives at the reference grid:

$$\partial_x g(x) \approx \frac{1}{\Delta x}\left[\frac{1}{12}g(x-2\Delta x) - \frac{2}{3}g(x-\Delta x) + \frac{2}{3}g(x+\Delta x) - \frac{1}{12}g(x+2\Delta x)\right]. \tag{2.28}$$

Similarly, evaluated equation (2.23) at $\alpha = 1/2$ gives us:

$$\partial_x g\left(x+\frac{1}{2}\Delta x\right) \approx \frac{1}{\Delta x}\left[\frac{1}{24}g(x-\Delta x) - \frac{9}{8}g(x) + \frac{9}{8}g(x+\Delta x) - \frac{1}{24}g(x+2\Delta x)\right]. \tag{2.29}$$

Note that we can also obtain the derivatives in the reference grid by shifting equation (2.29) a half grid-point in the negative direction giving us

$$\partial_x g(x) \approx \frac{1}{\Delta x}\left[\frac{1}{24}g\left(x-\frac{3}{2}\Delta x\right) - \frac{9}{8}g\left(x-\frac{1}{2}\Delta x\right) + \frac{9}{8}g\left(x+\frac{1}{2}\Delta x\right) - \frac{1}{24}g\left(x+\frac{3}{2}\Delta x\right)\right]. \tag{2.30}$$

Equation (2.30) is the fourth-order operator for approximating the first order derivatives. Our spatial derivatives are based on the fourth-order approximation in equation (2.30).

Discrete wave equations

By using the second-order approximation in equation (2.26) for time derivatives and fourth-order approximation in equation (2.30) for spatial derivatives (See section finite-difference operators for detail), the discrete form of wave equations in (2.15)

and (2.16) can be given by as follows:

$$
\begin{aligned}
[v_x]_{i,j,k}^{n+1/2} &= [v_x]_{i,j,k}^{n-1/2} + \left[\Delta t b_x \left(D_x\tau_{xx} + D_y\tau_{xy} + D_z\tau_{xz} + f_x\right)\right]_{i,j,k}^{n} \ , \\
[v_y]_{i+1/2,j+1/2,k}^{n+1/2} &= [v_y]_{i+1/2,j+1/2,k}^{n-1/2} + \left[\Delta t b_y \left(D_x\tau_{xy} + D_y\tau_{yy} + D_z\tau_{yz} + f_y\right)\right]_{i+1/2,j+1/2,k}^{n} \ , \\
[v_z]_{i+1/2,j,k+1/2}^{n+1/2} &= [v_z]_{i+1/2,j,k+1/2}^{n-1/2} + \left[\Delta t b_z \left(D_x\tau_{xz} + D_y\tau_{yz} + D_z\tau_{zz} + f_y\right)\right]_{i+1/2,j,k+1/2}^{n} \ .
\end{aligned}
\tag{2.31}
$$

for the particle velocity and

$$
\begin{aligned}
[\tau_{xx}]_{i+1/2,j,k}^{n+1} &= [\tau_{xx}]_{i+1/2,j,k}^{n} + \Delta t \Bigg[\left(\lambda + 2\mu\right) D_x v_x + \lambda \left(D_y v_y + D_z v_z\right) + I_{xx} \Bigg]_{i+1/2,j,k}^{n+1/2} \ , \\
[\tau_{yy}]_{i+1/2,j,k}^{n+1} &= [\tau_{yy}]_{i+1/2,j,k}^{n} + \Delta t \Bigg[\left(\lambda + 2\mu\right) D_y v_y + \lambda \left(D_x v_x + D_z v_z\right) + I_{yy} \Bigg]_{i+1/2,j,k}^{n+1/2} \ , \\
[\tau_{zz}]_{i+1/2,j,k}^{n+1} &= [\tau_{zz}]_{i+1/2,j,k}^{n} + \Delta t \Bigg[\left(\lambda + 2\mu\right) D_z v_z + \lambda \left(D_x v_x + D_y v_y\right) + I_{zz} \Bigg]_{i+1/2,j,k}^{n+1/2} \ , \\
[\tau_{yz}]_{i+1/2,j+1/2,k+1/2}^{n+1} &= [\tau_{yz}]_{i+1/2,j+1/2,k+1/2}^{n} + \Delta t \left[\mu_{yz} \left(D_z v_y + D_y v_z\right) + I_{yz}\right]_{i+1/2,j+1/2,k+1/2}^{n+1/2} \ , \\
[\tau_{xz}]_{i,j,k+1/2}^{n+1} &= [\tau_{xz}]_{i,j,k+1/2}^{n} + \Delta t \left[\mu_{xz} \left(D_z v_x + D_x v_z\right) + I_{xz}\right]_{i,j,k+1/2}^{n+1/2} \ , \\
[\tau_{xy}]_{i,j+1/2,k}^{n+1} &= [\tau_{xy}]_{i,j+1/2,k}^{n} + \Delta t \left[\mu_{xy} \left(D_y v_x + D_x v_y\right) + I_{xy}\right]_{i,j+1/2,k}^{n+1/2} \ .
\end{aligned}
\tag{2.32}
$$

for the stresses, with

$$
\begin{aligned}
b_x &= \frac{1}{2}\left[b_{i,j,k} + b_{i-1,j,k}\right] \ , \\
b_y &= \frac{1}{2}\left[b_{i,j,k} + b_{i,j-1,k}\right] \ , \\
b_z &= \frac{1}{2}\left[b_{i,j,k} + b_{i,j,k-1}\right] \ .
\end{aligned}
\tag{2.33}
$$

$$
\begin{aligned}
\mu_{yz} &= \left[\frac{1}{4}\left(\frac{1}{\mu_{i,j,k}} + \frac{1}{\mu_{i,j-1,k}} + \frac{1}{\mu_{i,j,k-1}} + \frac{1}{\mu_{i,j-1,k-1}}\right)\right]^{-1} \ , \\
\mu_{xz} &= \left[\frac{1}{4}\left(\frac{1}{\mu_{i,j,k}} + \frac{1}{\mu_{i-1,j,k}} + \frac{1}{\mu_{i,j,k-1}} + \frac{1}{\mu_{i-1,j,k-1}}\right)\right]^{-1} \ , \\
\mu_{xy} &= \left[\frac{1}{4}\left(\frac{1}{\mu_{i,j,k}} + \frac{1}{\mu_{i-1,j,k}} + \frac{1}{\mu_{i,j-1,k}} + \frac{1}{\mu_{i-1,j-1,k}}\right)\right]^{-1} \ .
\end{aligned}
\tag{2.34}
$$

In the equations above, b_x, b_y, and b_z are the effective media parameters for the reciprocal of density, $[b_{i,j,k} = 1/\rho_{i,j,k}]$, and μ_{yz}, μ_{xz} and μ_{xy} are the effective medium parameters for the rigidity. The use of effective media parameters the staggered-grid formulation follows from the work of (Ikelle and Amundson, 2005) who applied this technique to fourth-order spatial operators in the staggered-grid technique. The effective media parameters provide a more accurate representation of the actual parameters near the media interface by approximately satisfying the traction continuity condition across the interface. (Graves, 1996) used the numerical experiments for the fourth-order staggered-grid system to show the use of effective media. Furthermore, media averaging is necessary to ensure numerical stability when an interface with large media contrast intersects the free surface.

The operators D_x, D_y, and D_z denote the first-order spatial derivative for x, y, and z, respectively. These first-order derivative operators are generally evaluated by either a second-order difference (section finite-difference operators),

$$D_x g_{i,k} \approx \frac{1}{\Delta x}\left(g_{i+1/2,k} - g_{i-1/2,k}\right) \ , \tag{2.35}$$

or a fourth-order difference,

$$D_x g_{i,k} \approx \frac{1}{\Delta x}\left[\frac{9}{8}\left(g_{i+1/2,k} - g_{i-1/2,k}\right) - \frac{1}{24}\left(g_{i+3/2,k} - g_{i-3/2,k}\right)\right] \ . \tag{2.36}$$

Note that one can use sixth-order finite-difference operator (which requires six grid points) or even order higher than sixth. Such approach obviously will be more accurate than the fourth-order finite difference considered here, however such approach require decreasing the grid spacing, and hence significantly increase the computing requirements for finite-difference modeling. Our experience suggests that fourth-order finite difference is accurate enough for our practical purpose as we will illustrate later by comparing our finite difference results to analytical result.

In summary, we use the second-order approximation for time derivatives and

fourth-order approximation for space derivatives. These choices imply that a minimum of five grid points per wavelength is required when selecting the media parameters and grid spacing Δx in accordance with (Levander, 1988).

To conclude this section, I would like to draw attention on two important characteristics of the staggered grid that we have adopted here. The first one is that through numerical implementation of equations (2.31) and (2.32) we avoid taking derivatives of medium parameters which are discontinuous in space. The second is that operator in the staggered grid technique in equations (2.31) and (2.32) are all centered naturally at the same point in space and time. Thus the resulting finite-difference system of equations is staggered both in space and in time. The velocity field at time $(n+1/2)\Delta t$ is updated explicitly from equations (2.31) by using the velocity field at time $(n-1/2)\Delta t$ and the stress field at time $n\Delta t$. The stress field at time $(n+1)\Delta t$ is updated explicitly by equations (2.32) by using stress field at $n\Delta t$ and the previously updated velocity field at time $(n+1/2)\Delta t$. The components of particle velocity are updated independently from the stresses in the staggered-grid technique, making the scheme efficient and concise.

CODE VERIFICATION

We have implemented the staggered-grid finite-difference technique in the previous section. The goal in this section is to verify the staggered-grid finite-difference code. One way to verify the finite-difference code is to compare the modeled data generated by the staggered-grid finite-difference program with the analytical solution in a homogeneous medium. Another way is to check snapshots of wave propagation by using basic physics principles.

Analytical solution

For the special case of a homogeneous acoustic medium, the wavefield (pressure or displacement) has an analytical solution, which can be obtained by convolution between Green's function and source wavelet. The Green's function in a 3D homogeneous acoustic mediumis given by (Ikelle and Amundson, 2005)

$$g^{(3D)}(R,\tau) = \frac{1}{4\pi R}\delta(\tau - R/V)\ . \tag{2.37}$$

where R is the distance between source $\mathbf{x}$ and receiver $\mathbf{x}'$, $R = |\mathbf{x} - \mathbf{x}'|$, V is the velocity of the medium. The 3D Green's function is a weighted delta function.

Assuming a 3D homogeneous acoustic medium with P-wave velocity $V = 2000$ m/s and density $\rho = 1.9$ g/ cm^3, the pressure data was modeled for one single receiver with source and receiver distance $R = 250$ m by a 3D staggered-grid finite-difference technique.

The 3D Green's function in equation (2.37) is shown on the top left in Figure 3. Predicted data calculated by the convolution between the source wavelet (the Ricker wavelet with 20 Hz central frequency) and the 3D Green's function in equation (2.37) is shown at the top right in Figure 3. The modeled pressure data is shown at the bottom left in Figure 3. The comparison between the modeled data generated by staggered-grid finite-difference technique and predicted data is shown at the bottom left in Figure 3. Comparing the modeled data (the blue line) with the predicted data (the red line), we can see that 3D finite-difference modeling results match the analytical solution as theoretically expected.

Snapshots of wave propagation

Snapshots are recording the wavefield at fixed positions at any given time. The study of snapshots helps us to better understand wave propagation in complex structures, as we can see how waves respond to the structures as time goes on. In this section, we

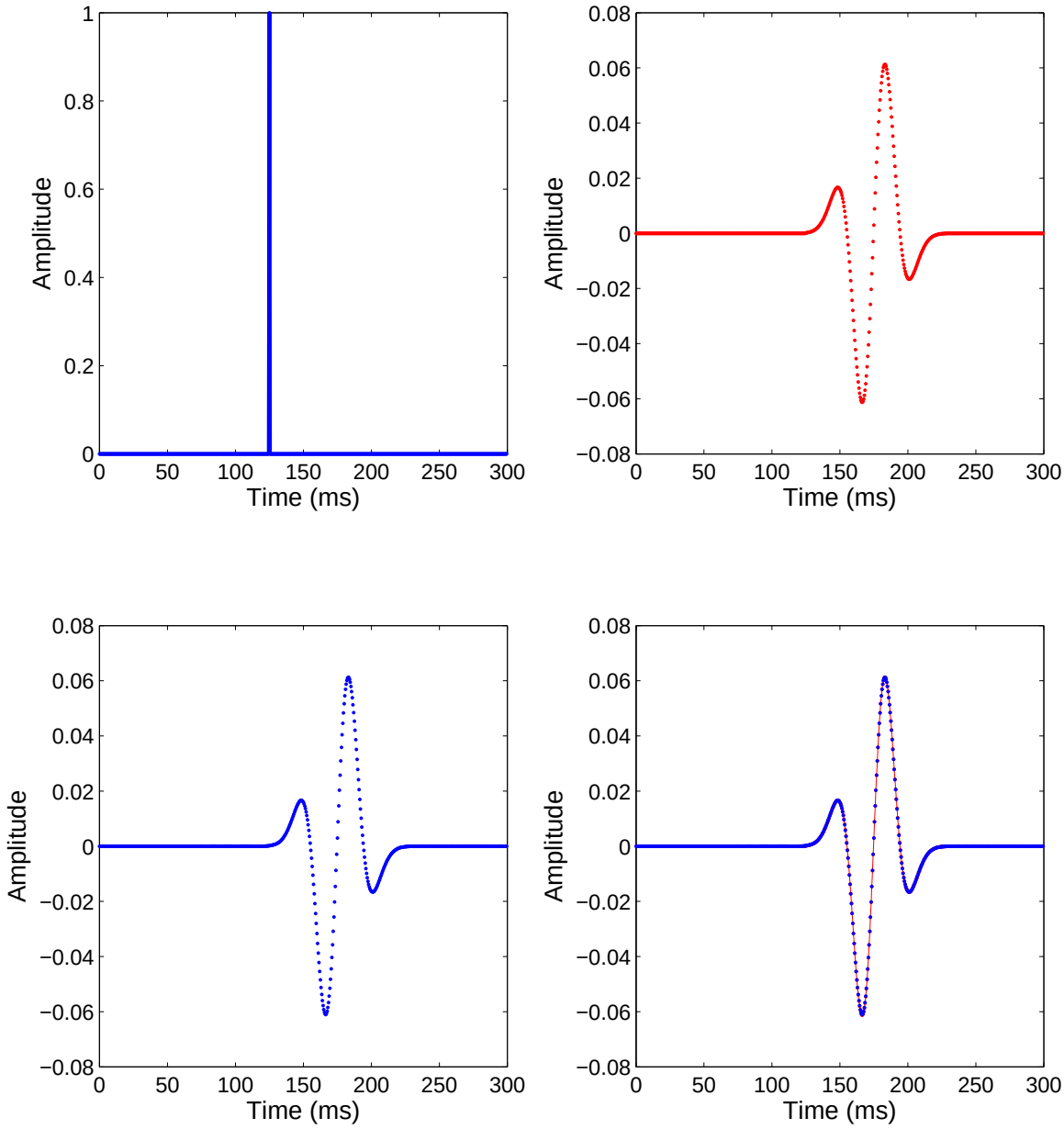

Fig. 3. Comparison between the modeled data and the analytical solution in a 3D homogeneous medium. Properties of the medium are V_p = 2000 m/s and ρ = 1.9 g/cm^3. (top left) the 3D Green's function, (top right) predicted data calculated by the convolution between the source wavelet and the 3D Green's function, (bottom left) the modeled pressure data at a single receiver located 250 m away from the source, (bottom right) comparison between the predicted data and the modeled data. The red line indicates the predicted data, the blue line indicates the modeled data.

will use basic physics principles to check the accuracy of wave-propagation snapshots in a model made of two homogeneous elastic isotropic media.

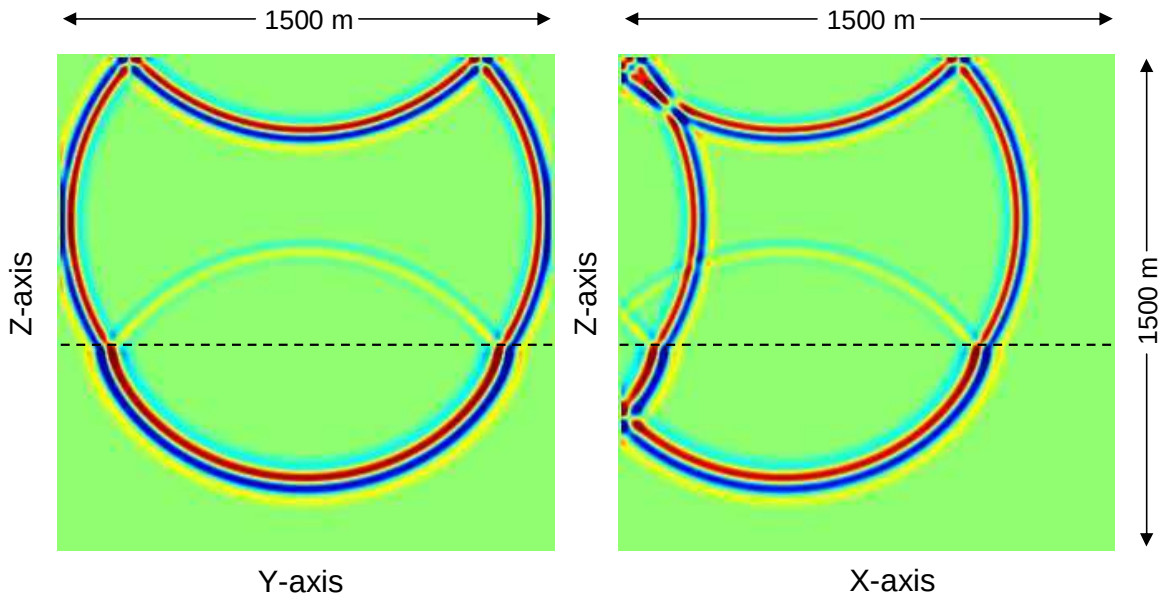

Fig. 4. Snapshots of wave propagation in a model consisting of two homogeneous elastic isotropic media. Properties of the top medium are $V_p = 2000$ m/s, $V_s = 1100$ m/s, and $\rho = 1.9$ g/cm^3. Those of the bottom medium are $V_p = 2500$ m/s, $V_s = 1300$ m/s and $\rho = 2.2$ g/cm^3, the interface is located at 900 m depth. Snapshots were taken at 400 ms. Waves were generated by an explosive source which is located at (500 m, 750 m, 500 m). The physical quantity displayed here is the volumetric deformation. Two planes passing the source position displayed here are: (left) the Y-Z plane at x=500 m, and the (right) X-Z plane at y=750. Notice that the data shown here were generated without using the absorbing boundary condition as we see the wrap-around waves reflected from the boundaries of the geological model.

Snapshots of wave propagation in this model are shown in Figure 4. When the wave reaches the interface between the two media, part of its energy returns to the top medium from which it came, that is reflection. The remaining energy enters the bottom layer, that is transmission. The reflections and transmissions follow Snell's law and Fermat's principle. We can see all the seismic events as theoretically expected from Figure 4. The wrap-around waves are the undesired reflections from the boundary of the model, and we will discuss how to eliminate the wrap-around events.

BOUNDARY CONDITION

In the real world, the earth is an inhomogeneous semi-infinite medium, and seismic waves can propagate to an infinite distance horizontally and vertically, except for air-solid interface in land seismic and air-water interface in marine seismic (Air-solid and air-water interface is at the free-surface boundary). However, for the numerical modeling the computational space is limited, and we need to truncate the infinite geological models to finite computational domains. The edges of these truncated models produce undesirable boundary reflections on the computed synthetic data in Figure 4. These wrap-around events eventually override the actual seismic signals in the data. An absorbing boundary condition is needed in order to eliminate the undesired reflections from the edges of the truncated model.

Free-surface boundary condition

The air-solid interface in land and the air-water interface in marine are considered as the free-surface boundary in staggered-grid finite-difference modeling. Free-surface boundary condition must be carefully considered in finite-difference technique because of numerical stability and computational accuracy. (Ikelle and Amundson, 2005) described a method for implementing a planar free-surface boundary condition in the staggered-grid finite-difference technique. This method assumes the zero-stress condition at the free surface and explicitly implemented by fourth-order spatial difference operator. Let the free surface be at a depth of $z = 0$. Then, the free-surface boundary condition is zero-stress condition at the free surface, which can be expressed as:

$$\tau_{zz}|_{k=0} = \tau_{yz}|_{k=0} = \tau_{xz}|_{k=0} = 0 \ , \tag{2.38}$$

The free-surface boundary condition given in (2.38) is that the normal stress, τ_{zz}, and the shear stress, τ_{xz} and τ_{yz}, are null at $z = 0$. The horizontal spatial derivative poses no problem for staggered-grid implementation in equations (2.32), however, for

the vertical spatial derivative using the fourth-order difference operator, we have to add two grid points above $z = 0$. Setting the free-surface boundary at a depth of $z = 0$, the values of the stress field above the free surface can be obtained by using an imaging method suggested by (Levander, 1988) and (Graves, 1996). The stress field above the free surface can be expressed as:

$$\begin{aligned}
&\tau_{zz}|_{k=0} = 0, && \tau_{zz}|_{k=-1} = -\tau_{zz}|_{k=-1}, \\
&\tau_{yz}|_{k=-\frac{1}{2}} = -\tau_{yz}|_{k=\frac{1}{2}}, && \tau_{yz}|_{z=-\frac{3}{2}} = -\tau_{yz}|_{k=\frac{3}{2}}\ , \\
&\tau_{xz}|_{k=-\frac{1}{2}} = -\tau_{xz}|_{k=\frac{1}{2}}, && \tau_{xz}|_{z=-\frac{3}{2}} = -\tau_{xz}|_{k=\frac{3}{2}}\ .
\end{aligned} \tag{2.39}$$

Note that the stress components τ_{xx}, τ_{yy} and τ_{xy} do not need special care for the free-surface boundary condition because the spatial derivatives of these quantities are respective with x, and y axis only. Particle velocity components v_x, v_y, and v_z above the free-surface boundary can be calculated by equation (2.31).

Absorbing boundary condition

The earth is an inhomogeneous semi-infinite medium. There is no boundary limit except on the top for an air-solid interface in land and air-water interface in marine, therefore seismic waves can propagate to infinite distance horizontally and downward vertically in the real world. However, the computational domain is limited, we have to truncate the infinite geological model to a finite computational region where we are interested. The edges of these truncated models produce undesirable boundary reflections on the modeled data (Figure 4), and these undesired events eventually override the actual seismic signals in the data. An absorbing boundary is needed in order to eliminate the undesired boundary reflections.

Another advantage for absorbing boundary condition is that we can also apply the absorbing boundary condition replacing the free-surface boundary condition in finite-difference modeling. By using absorbing boundary we can avoid the free-

surface multiples at the air-water interface in simulating marine data acquisition. Data generated by using the absorbing boundary condition is often used to check the multiple-attenuation technique, design surveys, and other studies when free-surface multiples should be eliminated.

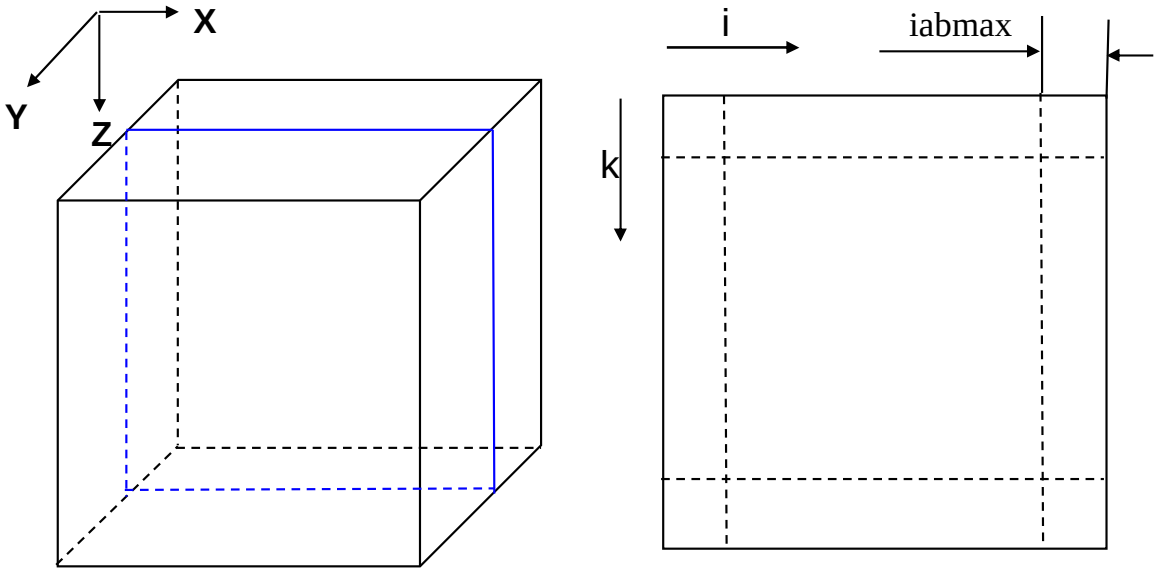

Fig. 5. Grid configuration for absorbing boundary condition (Cerjan et al., 1985). (left) 3D absorbing boundary configuration, (right) one of the X-Z plane in 3D model. *iabmax* is the absorbing width in grid points.

One solution to the undesired boundary reflections is that we can select the model large enough so that waves reach the boundary only after we finished the recording. Unfortunately, this solution is not applicable yet because it requires a increase of the present model size by a factor of 8 or even larger (present computer cant afford it).

The current approach to absorbing boundary is to attenuate the waves before they reach the boundary. A number of technique performing this attenuation have been proposed in the last forty years. One of such techniques is to use an approximation to extrapolate the interior solution one grid outward to fill in the boundary introduced by (Clayton and Engquist, 1977). This method is not very effective for waves with a large incidence angle. Another technique is to introduce additional match (as depicted in Figure 5) in the geological model, then we try to attenuate

waves through that match. This method was proposed by (Cerjan et al., 1985), and often knows as sponge boundary condition. The technique for implementing the sponge boundary condition include first computing the following function $G(i)$, then multiply it by particle velocity and stress field within the match. The function $G(i)$ by which the wavefield variables are multiplied is (Ikelle and Amundson, 2005)

$$G(i) = \exp\left\{ -\left[\frac{\alpha}{iabmax}\,(iabmax - i)^2\right]\right\} \qquad for\, 1 \le i \le iabmax\ , \tag{2.40}$$

where $iabmax$ is the strip width in grid points and α is a constant determined by trial and error for the optical absorbing boundary conditions.

The challenge of using this sponge boundary condition is to select the value of $iabmax$ and α which allow us to attenuate the waves through this match. Through the trial we have the optimal $iabmax$ and α, obviously these quantities will vary with model size and medium parameters. We found out these quantities wont vary a lot through a series of tests with different geological parameters.

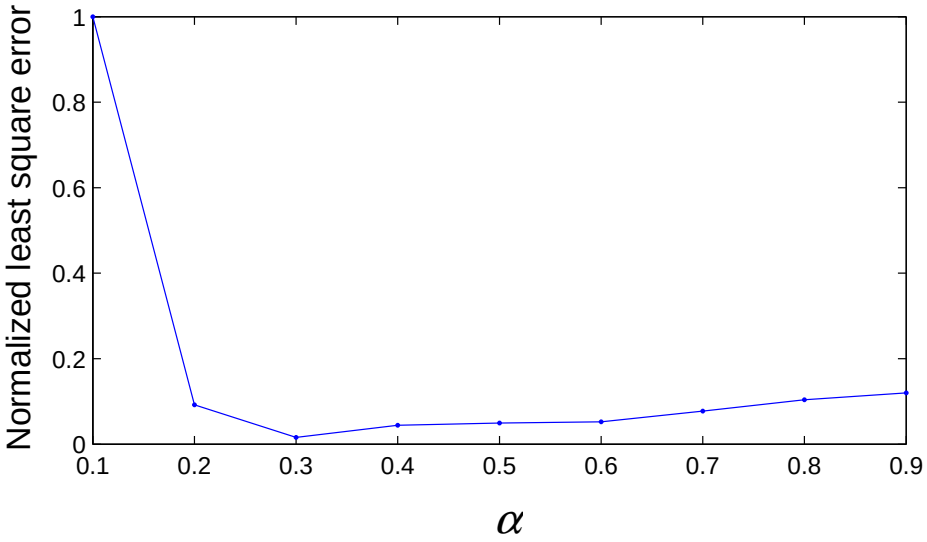

Fig. 6. The effectiveness of absorbing boundary condition as a function of α. α is a constant in equation (2.40). The best absorbing boundary is achieved when the error is minimum, where $\alpha = 0.3$ in this case. Note that a 30 grid-point absorbing boundary width is used in the test.

Let us validate these conclusion with some numerical results. Figure 6 shows

the effectiveness of absorbing boundary condition as a function of α. We measure the effectiveness of absorbing boundary condition here by computing the least square error between the data with perfect boundary condition and the one computed using the sponge absorbing boundary with formula $G(i)$. The way we define the data with perfect absorbing boundary condition is that we extend the geological model large enough so that the recording finished before the waves reach the boundaries.

Let d_{exa} be the data with prefect absorbing boundary and d_{abs} be the data computed by using the absorbing boundary condition defined in equation (2.40). We define the error as follows:

$$eror = \sum_{x \in M} \sum_{y \in M} \sum_{z \in M} \sum_{t} |d_{exa}(x, y, z, t) - d_{abs}(x, y, z, t)|^2 \ . \tag{2.41}$$

where M is the geological model and t is time.

In Figure 6, α value ranges from 0.1 to 0.9 with $iabmax = 30$ grid points. As we can see in this figure, the optical value of α is 0.3. This result is not entirely surprising because similar value has been obtained for 2D finite-difference modeling. Moreover, we conclude that with observations through multiple experiments this value vary little with different model parameters and with $iabmax$, especially when $iabmax$ is at least 30 grid points. All the numerical examples in this study used $\alpha = 0.3$ and $iabmax$ is a 30 grid-point absorbing width.

The wave propagation snapshots with an absorbing boundary condition in a model made of two homogeneous elastic isotropic media is shown in Figure 7. We have applied the absorbing boundary in all the edges in this model. As we can see, waves were eliminated when they reach the boundaries in Figure 7. Compared with Figure 4 the wrap-around events in Figure 7 are well eliminated.

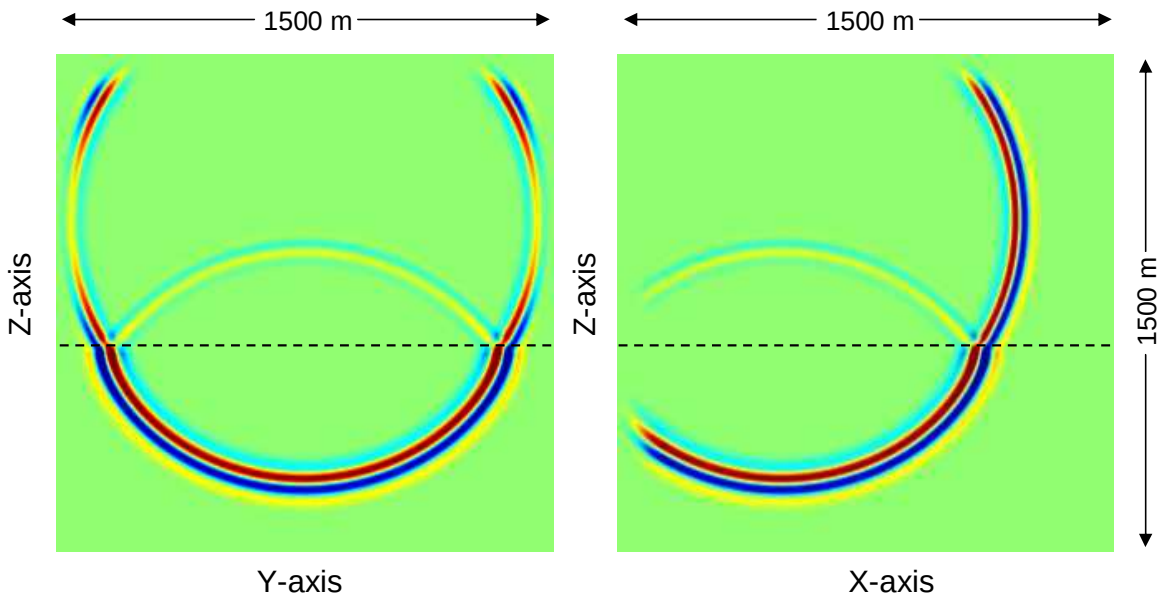

Fig. 7. Snapshots of wave propagation in a model consisting of two homogeneous elastic isotropic media with absorbing boundary. Snapshots were taken at 400 ms. Properties of the top medium are $V_p = 2000$ m/s, $V_s = 1100$ m/s and $\rho = 1.9$ g/cm^3, those of the bottom medium are $V_p = 2500$ m/s, $V_s = 1300$ m/s and $\rho = 2.2$ g/cm^3, the interface is located at 900 m depth. Waves were generated by an explosive source which is located at (500 m, 750 m, 500 m). The physical quantity displayed here is the volumetric deformation. Two planes passing the source position displayed here are: (left) the Y-Z plane at x=500 m, (right) the X-Z plane at y=750. Notice that the wrap-around waves in the data are well eliminated.

PRACTICAL LIMITATION

Wave equations (2.15) and (2.16) were approximated by a second-order time derivative operator and a fourth-order spatial derivative operator in the staggered-grid finite-difference technique. These finite-difference operators are the truncation of the Taylor series, error associated with these truncation can lead to stability and grid-dispersion problem during operating the finite-difference modeling. In this section, I want to elaborate the instability and grid dispersion by providing conditions for avoiding them.

Instability

In the staggered-grid finite-difference technique, the wavefield quantities are computed recursively, time step by time step. For example, computing the particle velocity components at time step $(n + 1/2)$ and the stress components at time step $(n + 1)$ require the previous time step $(n - 1/2)$ of the components of particle velocity and the previous time step n of the stress components. This recursive computation (time step by time step) can be a source of numerical instability. Errors introduced by the approximation of differential wave equations can propagate and be magnified during the recursive updates in the finite-difference technique, therefore causing significant instabilities during the computation and artifacts in the synthetic data.

Stability condition is only analyzed for the homogeneous medium. (Moczo et al., 2000) derived the stability condition for 3D homogeneous medium based on the fourth-order approximation. (Moczo et al., 2000) assumed that the errors of velocity and stress (at time $t = N\Delta t$ and $x = I\Delta x$, $y = J\Delta x$, and $z = K\Delta x$) have the harmonic form

$$E = \exp[i(-\omega N\Delta t + k_x I\Delta x + k_y J\Delta x + k_z K\Delta x)] \ , \tag{2.42}$$

where ω is an angular frequency, k_x, k_y, and k_z are the wavenumber with respect to

x, y, and z respectively. For instance the errors of components of particle velocity are:

$$\begin{bmatrix} e(v_x) \\ e(v_y) \\ e(v_z) \end{bmatrix} = \begin{bmatrix} A \\ B \\ C \end{bmatrix} \exp[i(-\omega N\Delta t + k_x I\Delta x + k_y J\Delta x + k_z K\Delta x)] \ , \tag{2.43}$$

Substituting equation (2.43) into equation (2.31) leads to the equations (Moczo et al., 2000)

$$\begin{bmatrix} A \\ B \\ C \end{bmatrix} \left(\frac{\Delta x \sin(\omega \Delta t/2)}{\Delta t} \right)^2 = \begin{bmatrix} (\alpha a)^2 + \beta^2 \sum & \alpha^2 ab & \alpha^2 ac \\ \alpha^2 ab & (\alpha b)^2 + \beta^2 \sum & \alpha^2 bc \\ \alpha^2 ac & \alpha^2 bc & (\alpha c)^2 + \beta^2 \sum \end{bmatrix} \begin{bmatrix} A \\ B \\ C \end{bmatrix} \ , \tag{2.44}$$

where α and β are the P-wave and S-wave velocity respectively, and

$$\begin{aligned} a &= \frac{9}{8}\sin(3\Delta x k_x/2) + \frac{1}{24}\sin(2\Delta x k_x/2) \ , \\ b &= \frac{9}{8}\sin(3\Delta x k_y/2) + \frac{1}{24}\sin(2\Delta x k_y/2) \ , \\ c &= \frac{9}{8}\sin(3\Delta x k_z/2) + \frac{1}{24}\sin(2\Delta x k_z/2) \ , \end{aligned} \tag{2.45}$$

and

$$\sum = a^2 + b^2 + c^2; \tag{2.46}$$

by solving equation (2.45), we can obtain (Moczo et al., 2000)

$$\sin(\omega \Delta t/2) = \pm \frac{\Delta t}{\Delta x} \alpha \sum^{1/2} \ , \tag{2.47}$$

$$\sin(\omega \Delta t/2) = \pm \frac{\Delta t}{\Delta x} \beta \sum^{1/2} \ , \tag{2.48}$$

Thus, we obtained two independent equations: equation (2.47) for the P wave and equation (2.47) for the S wave. From equation (2.47), we have $\Delta t \leq \Delta x \sum^{-1/2} /\alpha$, if we let the $\sum$ take its maximum value, the stability condition for the P wave should

be (Moczo et al., 2000)

$$\Delta t \leq \frac{6\Delta x}{7\sqrt{3}\alpha} \, , \tag{2.49}$$

and similarly, the stability condition for S wave should be (Moczo et al., 2000)

$$\Delta t \leq \frac{6\Delta x}{7\sqrt{3}\beta} \, , \tag{2.50}$$

If both types of waves are generated and propagate in a medium, condition in equation (2.49) should be used as the stability condition since $\alpha > \beta$.

Instability in heterogeneous medium is unlikely to occur if the temporal and spatial sampling interval satisfy the stability condition given by (Moczo et al., 2000)

$$\Delta t \leq \frac{6\Delta x}{7\sqrt{3}V_{max}} \, , \tag{2.51}$$

where V_{max} is the maximum wave velocity traveling within the 3-D model.

Grid dispersion

Another type of error that occurs in the finite-difference modeling method is the so-called grid dispersion. This error is also the result of truncation when we approximate spatial derivatives. The condition for avoiding grid dispersion is related to the number of grid points sampled per wavelength. A good rule is that a minimum sampling of five grid points per wavelength is required for the fourth-order finite-difference approximation (Levander, 1988). The grid dispersion condition for fourth-order approximation is

$$f_{max} < v_{min}/5\Delta x \, , \tag{2.52}$$

where v_{min} is the minimum wave velocity traveling within the 3D model, f_{max} is the maximum source frequency, Δx is the spatial sampling interval.

SUMMARY

We have developed a 3D staggered-grid finite-difference modeling code, and verified the finite-differen code by comparing the modeled data with an analytical solution in a homogeneous medium. We also applied absorbing boundary condition for the staggered-grid finite-difference technique in this chapter. Figure 8 shows a flowchart for 3D staggered-grid finite-difference modeling code. A Fortran code for a 3D staggered-grid finite-difference modeling for isotropic elastic media is provided in Appendix A.

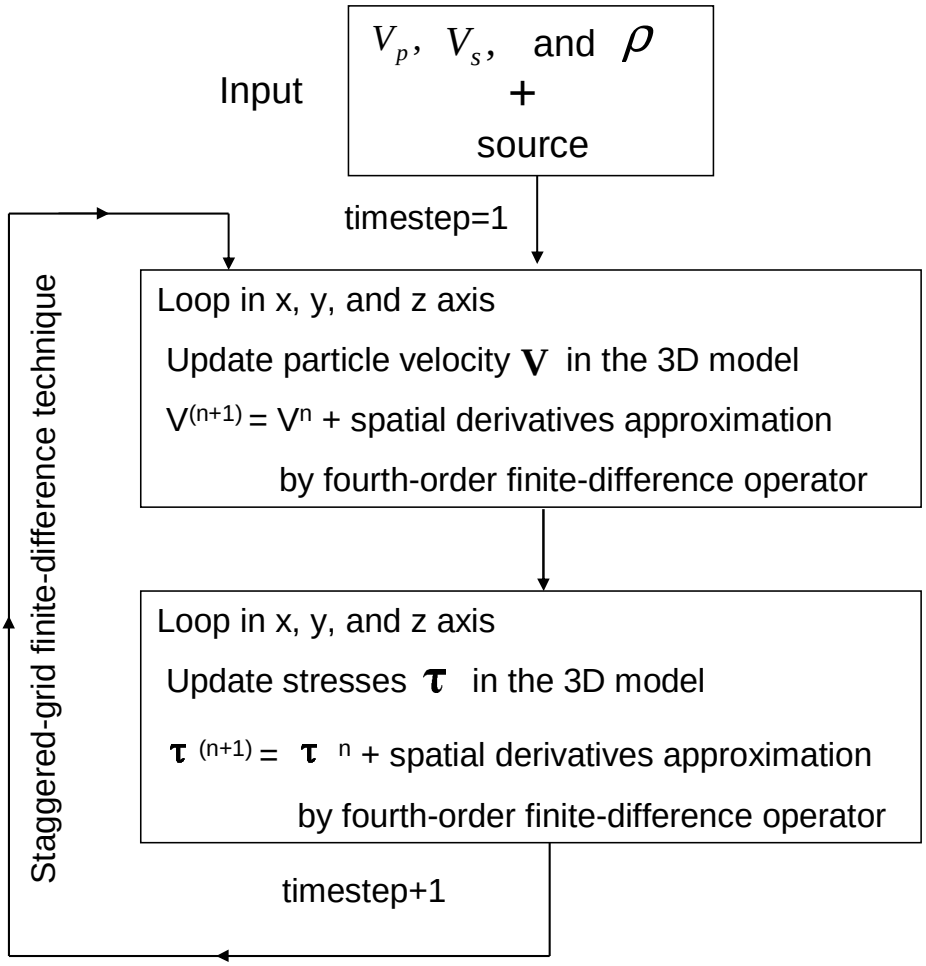

Fig. 8. A flowchart for 3D staggered-grid finite-difference modeling code implementation.

CHAPTER III

ADDITIONAL NUMERICAL EXAMPLES

In the previous chapter, I have developed and verified a 3D finite-difference modeling program. In this chapter I will provide additional numerical examples and use the basic physics principle to verify the 3D finite-difference modeling results. Here I will examine the wave-propagation snapshots generated by using the finite-difference modeling program in simple models. For this purpose, I will use three different geological models: a homogeneous model, a heterogeneous model consisting of two homogeneous layers, and a heterogeneous model with a faulted bedrock. We will use travel time to analyze seismic events displayed in the snapshots.

Notice that the results through this chapter are displayed in the three orthogonal planes: X-Y plane, Y-Z plane and X-Z plane which intersect at the source position. We have not displayed the other planes because of limited space to avoid redundancy.

A HOMOGENEOUS MODEL TEST

From the basic physics principles, an explosive source generates only P-waves, while a vertical force generates both P-waves and S-waves in a homogeneous isotropic medium. The travel time is invariant with the direction of wave propagation in a homogeneous isotropic medium. An explosion or a vertical force can be used as a seismic source in data acquisition. An explosion can be used in both marine and land seismic, while a vertical force can be used only in land seismic. In this section I will use a homogeneous elastic isotropic model to verify that the finite-difference modeling program can model both marine and land seismic data acquisition by using an explosion and a vertical force as the seismic sources.

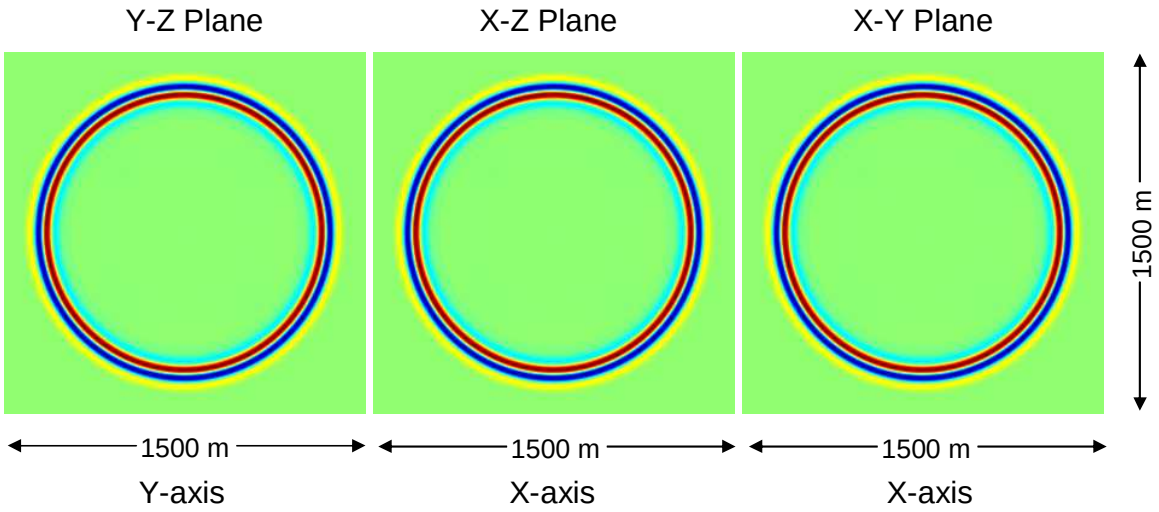

Fig. 9. Snapshots of wave propagation for measurements of volumetric deformation using an explosive source in a homogeneous solid elastic and isotropic medium. Properties of the medium are $V_p = 2500$ m/s, $V_s = 1300$ m/s and $\rho = 2.2$ g/cm^3. The waves were generated by an explosive source ($I_{xx} = I_{yy} = I_{zz}$, $I_{yz} = I_{xz} = I_{xy} = 0$, see Appendix A for detail) located in the center of the model. Snapshots were taken at 275 ms. Physical quantity displayed here is volumetric deformation. Three orthogonal planes which intersect at the source location are displayed here: (left) Y-Z plane, (middle) X-Z plane, (right) X-Y plane. The data were plotted using the same color scale.

Explosive source

In a homogeneous medium, the data generated by an explosive source contain only P-waves, even when the medium is elastic. These properties are valid only for isotropic media. One of the first verification of the finite-difference code is done by analyzing the snapshots of wave propagation through a homogeneous medium. Figures 9 and 10 show the data for the case of a homogeneous and isotropic medium, there is only one type of waves propagating in the medium. Since the source is explosive, the only type of waves generated is the P-waves. Notice that the volumetric deformation is recorded, the amplitude of volumetric deformation is invariant with direction, which shows a uniform spherical wavefront as seen Figure 9.

In seismic data acquisition, it is more and more common that all the three components of particle velocity are recorded even in marine seismic today. Unlike the invariant amplitude of volumetric deformation in Figure 9, the amplitude of the

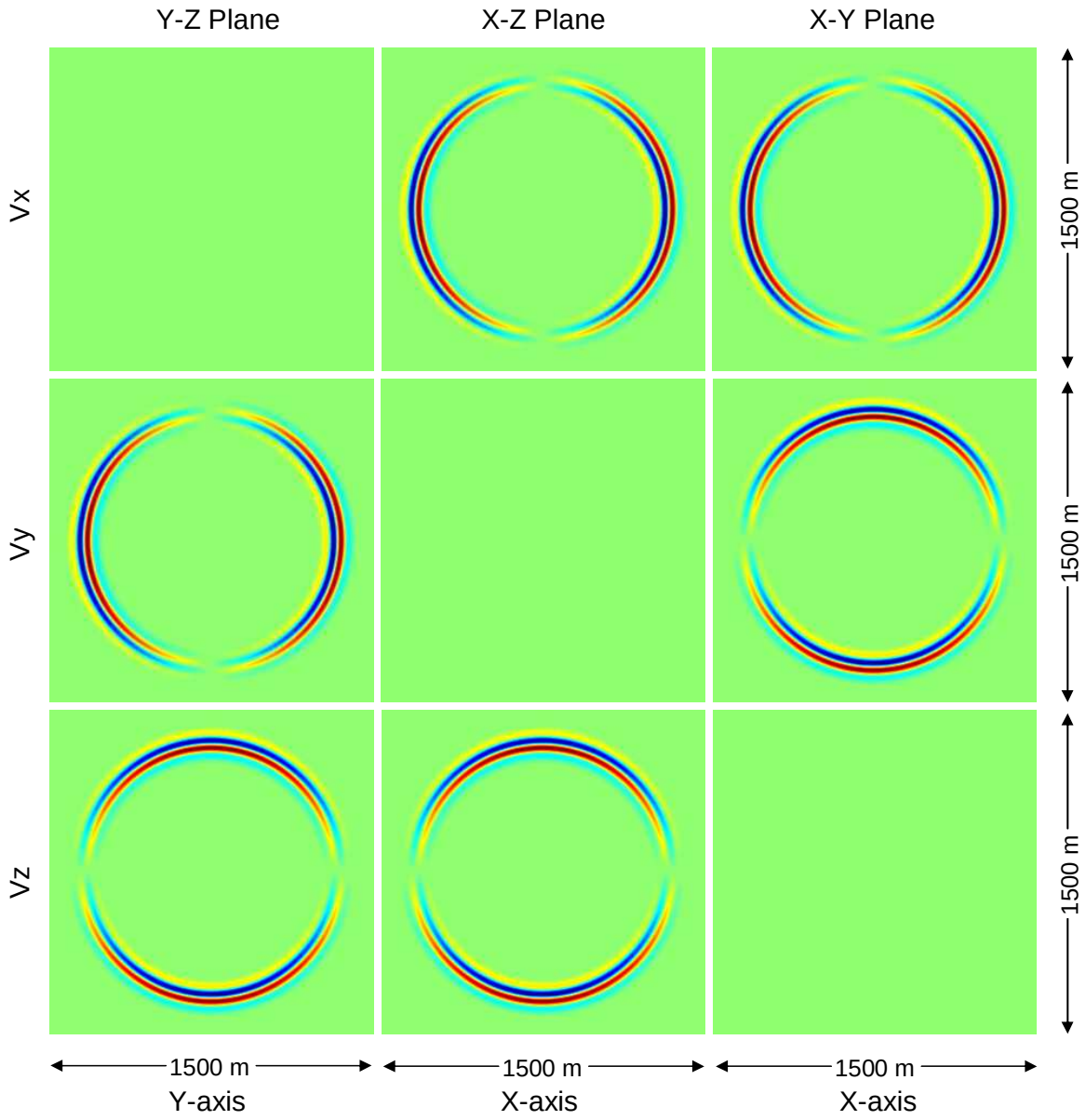

Fig. 10. Snapshots of wave propagation for measurements of particle velocity using an explosive source in a homogeneous solid elastic and isotropic medium. Properties of the medium are $V_p = 2500$ m/s, $V_s = 1300$ m/s and $\rho = 2.2$ g/cm^3. The waves were generated by an explosion located in the center of the model. Snapshots were taken at 275 ms. Physical quantities displayed here are: (top row) v_x, (middle row) v_y, (bottom row) v_z. Three orthogonal planes which intersect at the source location are displayed here: (left) Y-Z plane, (middle) X-Z plane, (right) X-Y plane. The data were plotted using the same color scale.

components of particle velocity here varies with direction as shown in Figure 10.

The particle velocity has the following relation with the pressure data (Ikelle and Amundson, 2005):

$$\frac{\partial v(x,y,z)_k}{\partial t} = -\frac{1}{\rho}\frac{\partial P(x,y,z)}{\partial x_k} \qquad k = 1,2,3\ . \tag{3.1}$$

where $v(x,y,z)_k$ is the kth component of particle velocity and $P(x,y,z)$ is the pressure. In any plane which passes through the source, the pressure is independent on the coordinate perpendicular to the plane. For example, in the case of the horizontal plane X-Y, the pressure is independent on the Z coordinate. This is why, in equation (3.1) for $k = 3$, the space derivative in the right-hand side is null, and consequently, the vertical component of the velocity will be zero in any point of this plane. This observation is generally true for all the components of the particle velocity measured on the corresponding perpendicular plane.

An explosive source generates a spherical wavefront. Consequently, the magnitudes of all quantities related to the wave propagation will have spherical representations at a given time. For example, $|\mathbf{v}|$ has a spherical symmetry, so it is constant. However, as one can see in Figure 10, the amplitude of these quantities is angle-dependent. For example, $v_x = |\mathbf{v}|\cos\theta$ is maximum in the x direction (where $\cos\theta = 1$) and 0 in the y direction (where $\cos\theta = 0$).

Vertical force

The usage of this finite-difference code is not limited to acoustic media only. It is also valid for elastic medium, therefore it supports both P-waves and S-waves. In order to validate this point, a homogeneous medium is considered and a vertical force is used to generate seismic waves.

If we record divergence of particle velocity, we could verify that only P-waves are observed as shown in Figure 11. This is consistent with the fact that divergence

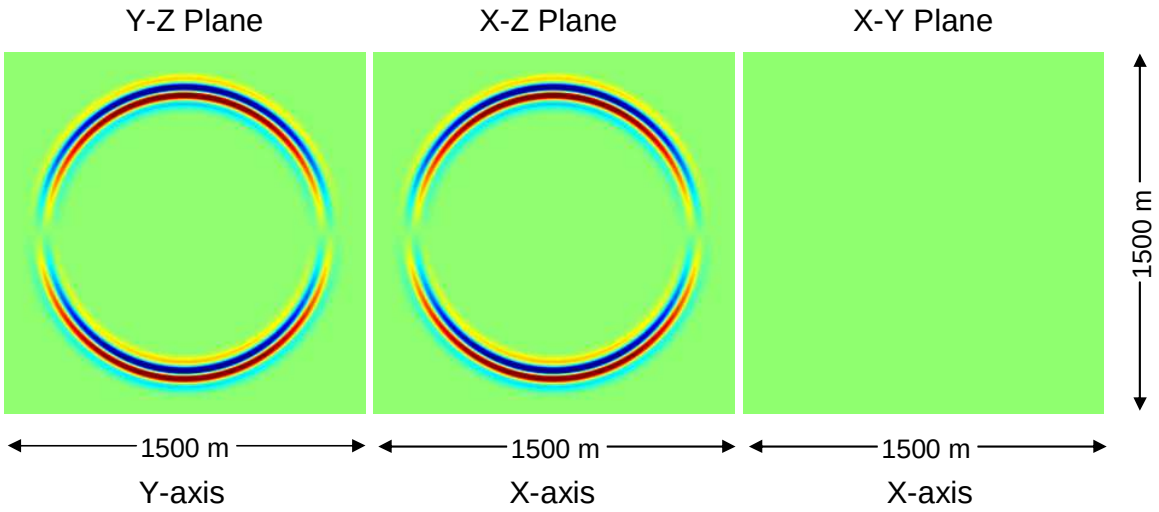

Fig. 11. Snapshots of wave propagation for measurements of divergence of particle velocity using a vertical force in a homogeneous solid elastic and isotropic medium. Properties of the medium are $V_p = 2500$ m/s, $V_s = 1300$ m/s and $\rho = 2.2$ g/cm^3. The waves were generated by a vertical force located in the center of the model. Snapshots were taken at 275 ms. Physical quantities displayed here is divergence of particle velocity. Three orthogonal planes which intersect at the source location are displayed here: (left) Y-Z plane, (middle) X-Z plane, (right) X-Y plane. The data were plotted using the same color scale.

describes the volumetric deformation in isotropic media.

As shown in Figure 12 two types of waves propagating with different velocities were generated. To identify each of the wave we consider the fact that in real world $V_p > V_s$. Therefore the outer circles are the P-waves and the inner circles are S-waves in Figure 12. The particle motion in the S-waves is perpendicular to the direction of propagation which is shown in Figure 12 bottom row. This also allows us to identify that the inner circles are S-waves.

As shown in Figure 12, only the vertical component of particle velocity of S-wave can be seen in the X-Y plane, which is consistent with the wave equations described earlier in chapter II.

The particle motion of S-wave generated by a vertical force is parallel to the z-axis in the X-Y plane at source location, therefore there is no horizontal motion is observed in that plane, which can be confirmed in Figure 12. The horizontal components of

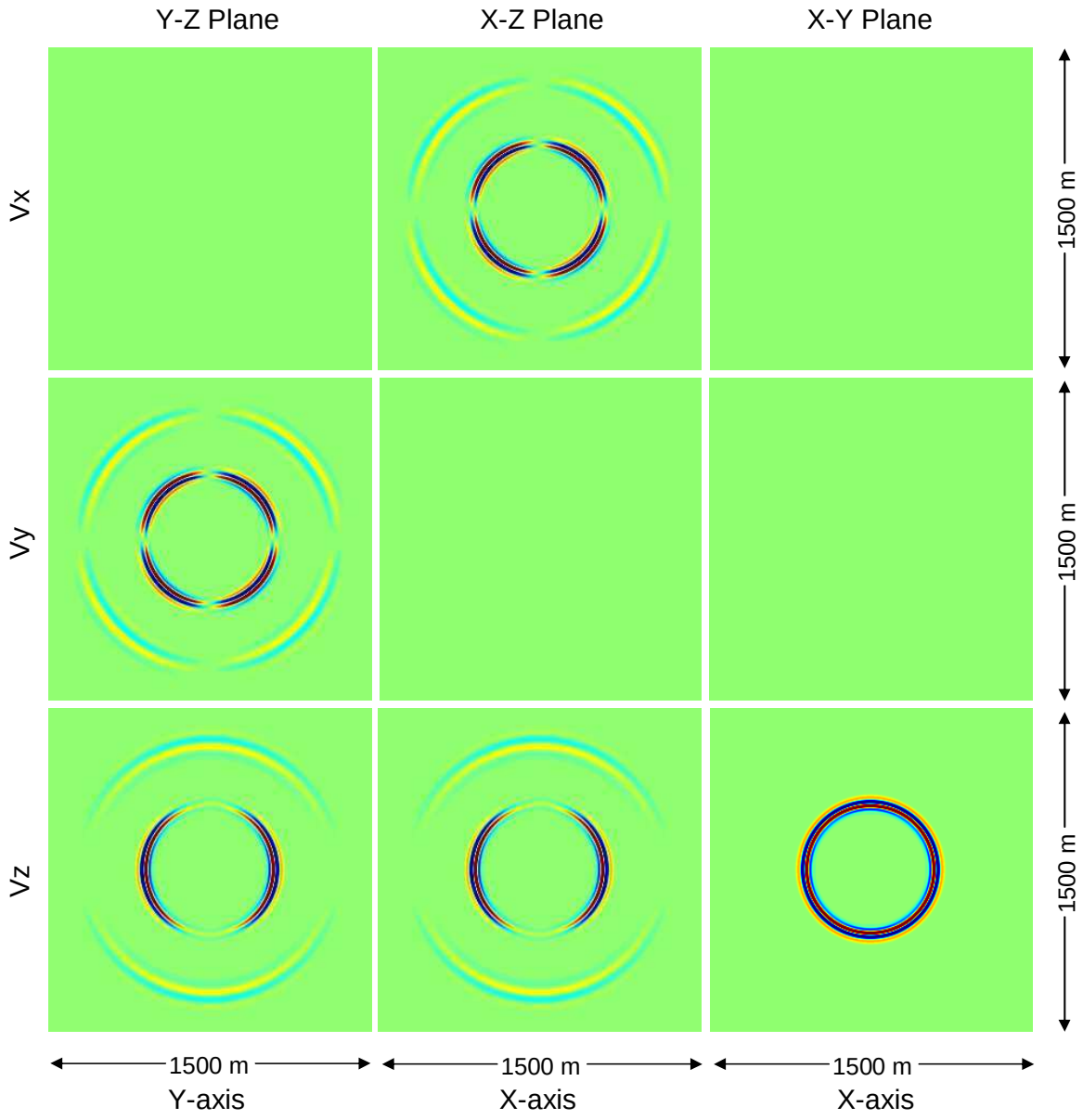

Fig. 12. Snapshots of wave propagation for measurements of particle velocity using a vertical force in a homogeneous solid elastic and isotropic medium. Properties of the medium are $V_p = 2500$ m/s, $V_s = 1300$ m/s and $\rho = 2.2$ g/cm^3. The waves were generated by a vertical force located in the center of the model. Snapshots were taken at 275 ms. Physical quantities displayed here are: (top row) v_x, (middle row) v_y, (bottom row) v_z. Three orthogonal planes which intersect at the source location are displayed here: (left) Y-Z plane, (middle) X-Z plane, (right) X-Y plane. The data were plotted using the same color scale.

particle velocity exhibit zero amplitude in X-Y plane as shown in Figure 12.

As stated in the previous section, for P-waves each of the three components of particle velocity is zero on its perpendicular plane. This is also observed in Figure 12 which shows v_x in Y-Z plane and v_y in X-Z plane are zero. In Y-Z plane and X-Z plane, the horizontal component of particle velocity of P-waves at normal incidence is zero because the particle motion of P-waves is parallel to z-axis at normal incidence. The horizontal component of particle velocity of S-waves is zero at horizontal direction in these two planes are because that the particle motion of S-waves is parallel to z-axis.

Note that the data generated by an explosive source which recorded the vertical component of particle velocity shown in Figure 10 bottom row, could be obtained by using a vertical force and recording volumetric deformation as shown in Figure 11. This observation is the direct verification of the reciprocity principle (Ikelle and Amundson, 2005).

A REFLECTION TEST

In the previous section, it has been verified that the finite-difference modeling program can properly model wave propagation in a homogeneous isotropic elastic medium. However, the earth is not homogeneous, but made of rocks with different physical properties. Reflections occur when the waves reach the interface between different type of rocks. In this section I will verify that the finite-difference modeling program can model reflections, transmissions and converted-waves. The model I used for this study is a heterogeneous model consisting of two homogeneous and isotropic media separated by a horizontal interface.

Explosive source

Considering a model with two homogeneous and isotropic acoustic media separated by a horizontal interface. A P-wave generated by an explosive source propagate through

the top medium as shown in Figure 13. When the P-wave reaches the horizontal interface between the two layers, it is partitioned into reflected wave (The wave is reflected to the top layer as P-wave: reflection r_{pp}.) and transmitted wave (The wave enters the bottom layer as P-wave: transmission t_{pp}) as illustrated in Figure 13.

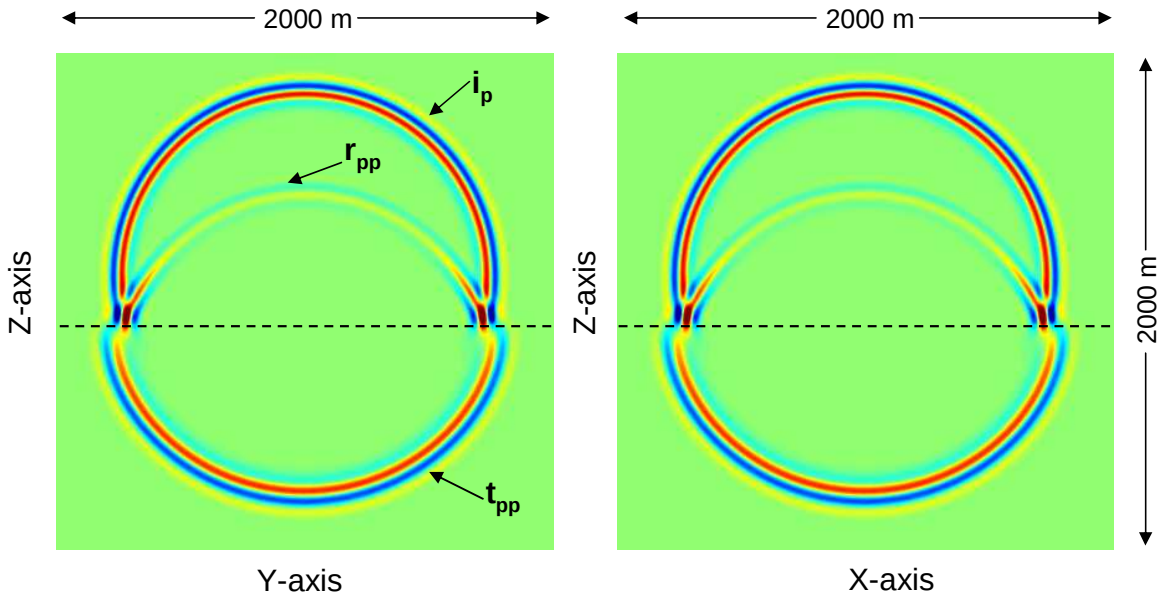

Fig. 13. Snapshots of wave propagation for measurements of pressure using an explosive source in a heterogeneous model. The heterogeneous model consists of two homogeneous and isotropic acoustic media separated by a horizontal interface. Properties of the top medium are $V_p = 2000$ m/s and $\rho = 1.9$ g/cm^3, those of the bottom medium are $V_p = 2500$ m/s and $\rho = 2.2$ g/cm^3. The size of the model is 2000 m $\times$ 2000 m $\times$ 2000 m, the interface is located at 1100 m depth, and source is located at (1000 m, 1000 m, 900 m). The waves were generated by an explosion. Snapshots were taken at 425 ms. The physical quantity displayed here is the pressure. Two vertical planes which pass the source location are displayed: (left) Y-Z plane, (right) X-Z plane. Symbols: i_p indicates incident P-wave, r_{pp} indicates reflected P-wave with incident P-wave, t_{pp} indicates transmitted P-wave with incident P-wave. The data were plotted using the same color scale.

However in elastic media, when a P-wave reaches the horizontal interface between the two layers, it is partitioned into two reflected waves r_{pp} and r_{ps} (The P-wave is converted to S-wave when reflected at the interface.) and two transmitted waves t_{pp} and t_{ps} (The P-wave is converted to S-wave when entering the bottom layer) as illustrated in Figure 14. Compared with Figure 13, Figure 14 has two more events r_{ps} and t_{ps} as expected. The amplitude for both converted waves (r_{ps} and t_{ps}) is zero

at normal incidence as we can see in Figure 14.

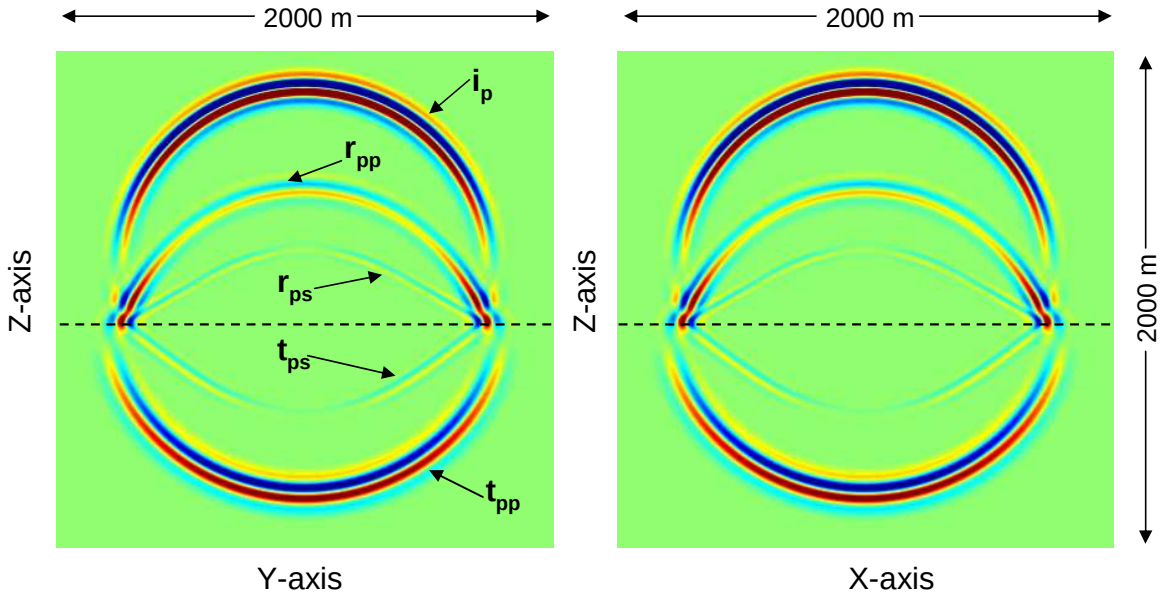

Fig. 14. Snapshots of wave propagation for measurements of v_z using an explosive source in a heterogeneous model. The heterogeneous model consists of two homogeneous and isotropic solid media separated by a horizontal interface. Properties of the top medium are $V_p = 2000$ m/s, $V_s = 1100$ m/s and $\rho = 1.9$ g/cm^3, those of the bottom medium are $V_p = 2500$ m/s, $V_s = 1300$ m/s and $\rho = 2.2$ g/cm^3. The size of the model is 2000 m $\times$ 2000 m $\times$ 2000 m, the interface is located at 1100 m depth, and source is located at (1000 m, 1000 m, 900 m). The waves were generated by an explosion. Snapshots were taken at 425 ms. The physical quantity displayed here is v_z. Two vertical planes which pass the source location are displayed: (left) Y-Z plane, (right) X-Z plane. Symbols: i_p indicates incident P-wave, r_{pp} indicates reflected P-wave with incident P-wave, r_{ps} indicates reflected S-wave with incident P-wave, t_{pp} indicates transmitted P-wave with incident P-wave, t_{ps} indicates transmitted S-wave with incident P-wave. The data were plotted using the same color scale.

We have verified the reflections, transmissions and converted-waves using the travel time and they all follow the Snell's law and Fermat's principle. As we can see the wave propagation in both models are horizontally symmetric in both Figure 13 and Figure 14, which is consistent with the geological model with a horizontal interface.

Vertical force

Let us consider a vertical force as a seismic source to generate waves in the model described earlier. It was shown that the vertical force generates both P-waves and S-waves in elastic media, therefore the waves propagating through the model include reflections, transmissions and converted-waves for both P and S waves.

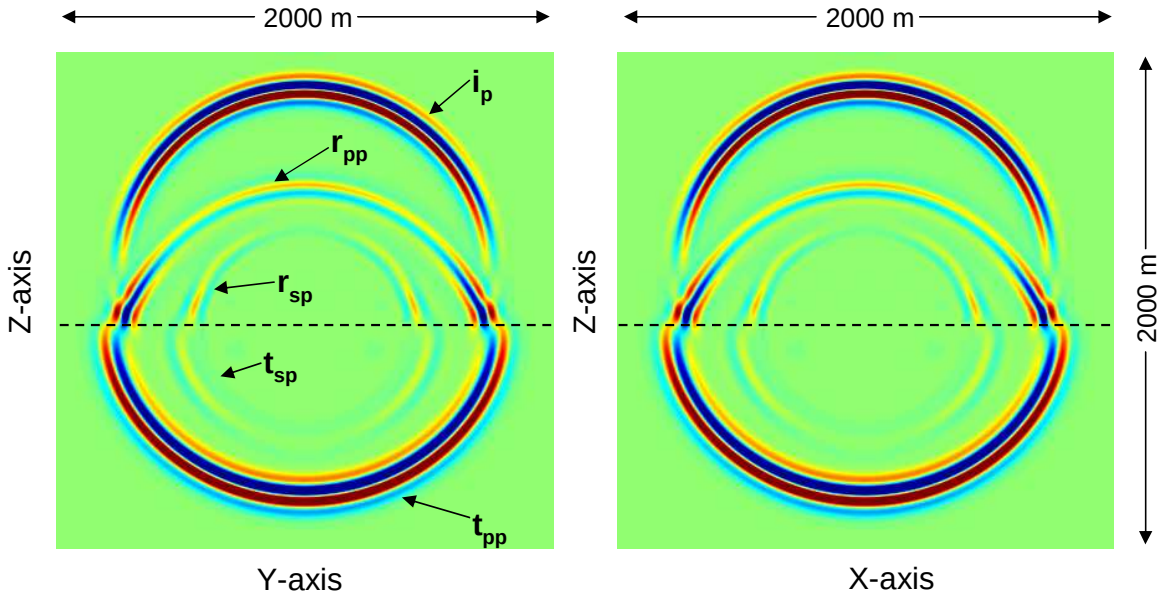

Fig. 15. Snapshots of wave propagation for measurements of volumetric deformation using a vertical force in a heterogeneous model. The heterogeneous model consists of two homogeneous and isotropic elastic media separated by a horizontal interface. Properties of the top medium are $V_p = 2000$ m/s, $V_s = 1100$ m/s and $\rho = 1.9$ g/cm^3, those of the bottom medium are $V_p = 2500$ m/s, $V_s = 1300$ m/s and $\rho = 2.2$ g/cm^3. The size of the model is 2000 m $\times$ 2000 m $\times$ 2000 m, the interface is located at 1100 m depth, and source is located at (1000 m, 1000 m, 900 m). The waves were generated by a vertical force. Snapshots were taken at 425 ms. The physical quantity displayed here is the volumetric deformation. The planes plotted here are: (left) Y-Z plane, (right) X-Z plane. Symbols: i_p indicates incident P-wave, r_{pp} indicates reflected P-wave with incident P-wave, r_{sp} indicates reflected P-wave with incident S-wave, t_{pp} indicates transmitted P-wave with incident P-wave, t_{sp} indicates transmitted P-wave with incident S-wave. The data were plotted using the same color scale.

From the previous section, when a P-wave reaches the horizontal interface between the two layers, it is partitioned into two reflected waves (r_{pp} and r_{ps}) and two transmitted waves (t_{pp} and t_{ps}). Similarly, when an S-wave reaches the horizontal

interface, it is also partitioned into two reflected waves (r_{ss} and r_{sp}) and two transmitted waves (t_{ss} and t_{sp}). This is because that an S-wave can be reflected back to the top layer and enters the bottom layer as an S-wave, an S-wave can also be converted to P-wave when reflected or transmitted.

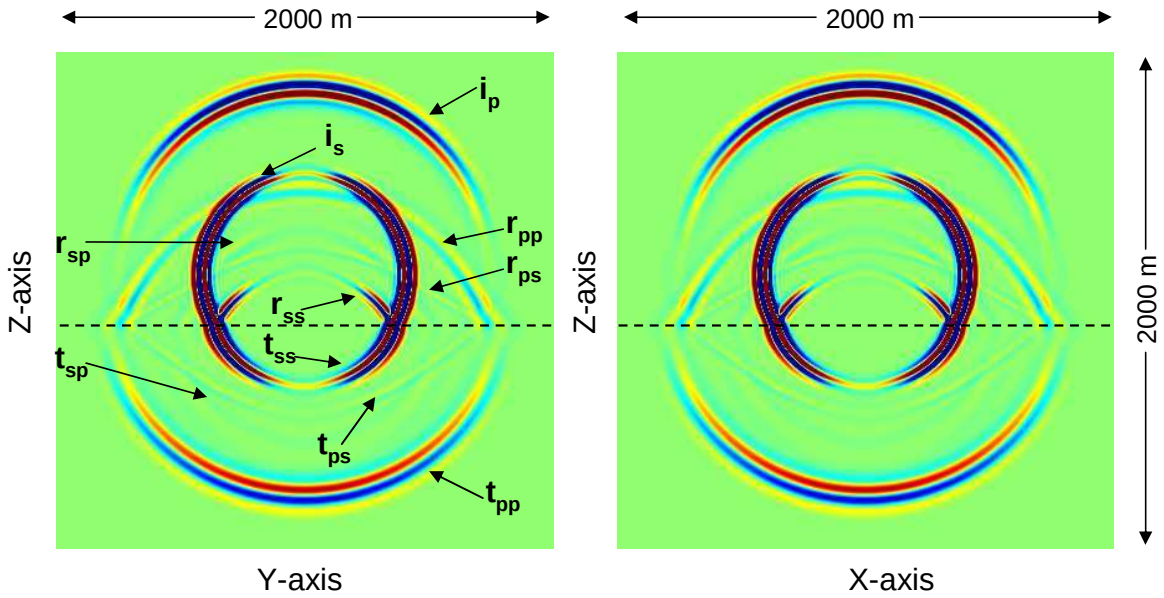

Fig. 16. Snapshots of wave propagation for measurements of v_z using a vertical force in a heterogeneous model. The heterogeneous model consists of two homogeneous and isotropic elastic media separated by a horizontal interface. Properties of the top medium are $V_p = 2000$ m/s, $V_s = 1100$ m/s and $\rho = 1.9$ g/cm^3, those of the bottom medium are $V_p = 2500$ m/s, $V_s = 1300$ m/s and $\rho = 2.2$ g/cm^3. The size of the model is 2000 m $\times$ 2000 m $\times$ 2000 m, the interface is located at 1100 m depth, and source is located at (1000 m, 1000 m, 900 m). The waves were generated by a vertical force. Snapshots were taken at 425 ms. The physical quantity displayed here is the vertical component of particle velocity v_z. The planes plotted here are: (left) Y-Z plane, (right) X-Z plane. Symbols: i_p indicates incident P-wave, r_{pp} indicates reflected P-wave with incident P-wave, r_{ps} indicates reflected S-wave with incident P-wave, t_{pp} indicates transmitted P-wave with incident P-wave, t_{ps} indicates transmitted S-wave with incident P-wave, r_{ss} indicates reflected S-wave with incident S-wave, r_{sp} indicates reflected P-wave with incident S-wave, t_{ss} indicates transmitted S-wave with incident S-wave, t_{ss} indicates transmitted S-wave with incident S-wave. The data were plotted using the same color scale.

The volumetric deformation describes compression and expansion in an isotropic medium, hence it is related to P-wave propagation only. Therefore if the volumetric deformation is recorded as in this case, the data contain information only for i_p, r_{pp},

r_{sp}, t_{pp}, and t_{sp}, which can be seen in Figure 15. Compared with Figure 13, Figure 15 has two more seismic events r_{sp} and t_{sp}, this is because the waves generated by a vertical force contain S-waves in addition to P-waves.

Particle velocity carries both P-waves and S-waves related information which is shown in Figure 16. Comparing the seismic events in Figure 16 with those in Figure 14, we can see S-wave events i_s, r_{ss}, r_{sp}, t_{ss}, and t_{sp} in addition to the P-wave events shown in Figure 14. The amplitude of the converted waves is zero at normal incidence, which is also seen in Figure 16.

We have also verified all the seismic events in Figure 15 and Figure 16 using the travel time. It was confirmed that both reflections and transmissions follow the Snell's law and Fermat's principle. As we can see the wave propagation are horizontally symmetric in both Figure 13 and Figure 14, which is consistent with the geological model with a horizontal interface.

A DIFFRACTION TEST

In the previous section, I have shown that our finite-difference modeling program can properly model wave propagation when encountering a horizontal interface. However, the interfaces between the rock is not always horizontal. The earth also has faults, folds, pinchouts, unconformities, and so on. Therefore reflections and transmissions are insufficient to describe the wave propagation because the energy can be diffracted. In this section I will show that our finite-difference program can also properly model the diffractions.

For this study, a model with a faulted bedrock will be used. This model consists of a homogeneous background medium with a homogeneous rectangular shape fault bedrock along the Y-axis. The physical properties of the model are invariant respect to Y-coordiante.

Figure 17 shows snapshots of wave propagation in this model. The plane dis-

played in Figure 17 is only the X-Z plane because the model is invariant with Y-axis. Before the waves reach the top corner of the faulted bedrock, the propagation is the same as in the previous section as can be seen in Figure 17. When P-waves reach the top corner of the faulted bedrock, we see how the diffracted P-waves (d_p) and S-waves (d_s) radiate from the corner is very clear. The top corner of the faulted bedrock is like a second source, and both diffracted P-waves and diffracted S-waves wavefronts are circular as expected.

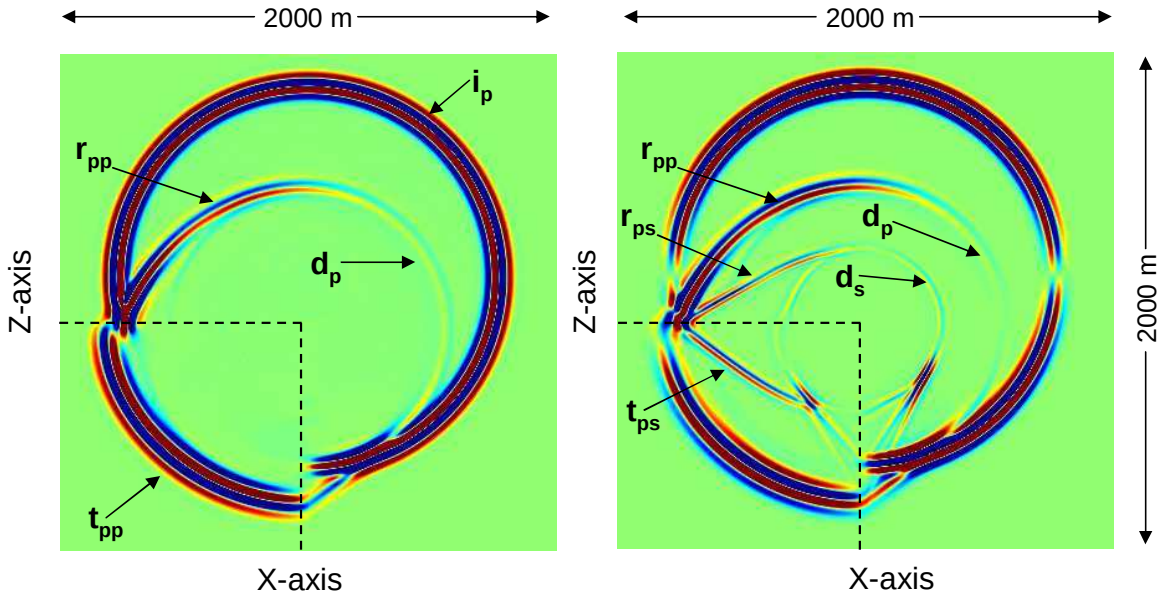

Fig. 17. Snapshots of diffractions from a model with faulted bedrock. The model consists of a homogeneous background medium with V_p = 2000 m/s, V_s = 1100 m/s and ρ = 1.9 g/cm^3. The fault bedrock is a rectangular shape homogeneous medium along the Y-axis with V_p = 2500 m/s, V_s = 1300 m/s and ρ = 2.2 g/cm^3. The size of the model is 2000 m × 2000 m × 2000 m. An explosive source is located at (1000 m, 1000 m, 900 m). Snapshots were taken at 425 ms. The physical quantities displayed here are: (left) volumetric deformation, (right) v_z. Symbols: i_p indicates incident P-wave, r_{pp} indicates reflected P-wave with incident P-wave, r_{ps} indicates reflected S-wave with incident P-wave, t_{pp} indicates transmitted P-wave with incident P-wave, t_{ps} indicates transmitted S-wave with incident P-wave, d_p indicates the P-wave diffraction, d_s indicates the incident S-wave diffraction. The data were plotted using the same color scale.

SUMMARY

In this chapter we have provided additional numerical examples showing that our finite-difference modeling program can model reflections, transmissions, diffractions and converted waves properly. We have also shown the ability of our finite-difference program to model both land and marine data acquisition.

CHAPTER IV

SOME EXAMPLES OF FINITE-DIFFERENCE APPLICATIONS

We have developed and verified a 3D finite-difference modeling tool in chapter II and III. In this chapter I will show some of the practical applications of the finite-difference modeling tool. In particular, two applications will be shown in this chapter. First the application of the finite-difference modeling in improving the illumination of a complex salt model will be shown. Then modeling shear-waves splitting and triplication in anisotropic medium using the 3D finite-difference technique will be followed.

COMPLEX SALT MODEL

The most challenging problem that exploration and production industry meets today in Gulf of Mexico is the salt. Salt body can be a good structural trap for hydrocarbon, therefore, salt and subsalt imaging is very important for locating the reservoir. Unfortunately, good imaging of the salt and subsalt structure is very difficult. This is because, first, salt has a very high seismic velocity compared with the surrounding sediments, which significantly increases the reflected energy and decreases the energy that passes through the salt body. The poor illumination of conventional seismic survey makes is very difficult to image the subsalt reflector. Second, the salt body usually has a very irregular shape, which greatly enhances the diffractions. The signal below the salt body is usually very weak due to the strong diffracted energy. In this section the synthetic data of a complex salt model generated by 3D finite-difference program will be shown and the subsalt reflection will be analyzed.

Figure 18 shows a complex salt model that mimics a marine environment in the Gulf of Mexico. The model is adapted from SEG salt model, the model covers a region of 5 km $\times$ 5 km $\times$ 2.5 km, with a 300 m water depth. The geology described

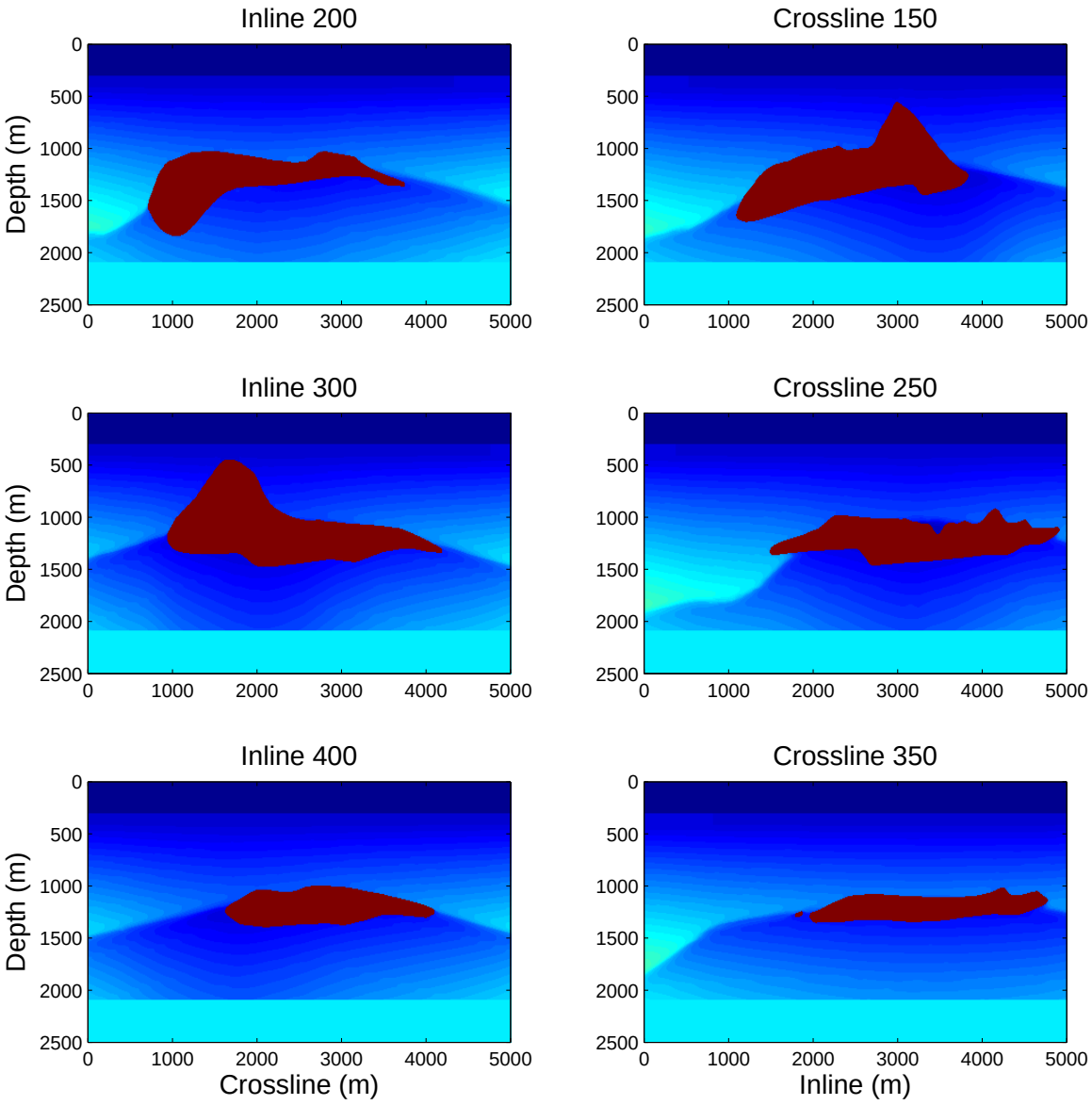

Fig. 18. A complex salt model of the Gulf of Mexico. This model is adapted form SEG salt model. The model covers a region of 5 km $\times$ 5 km $\times$ 2.5 km, water depth is 300 m. (left) P-wave velocity in inline direction, (right) P-wave velocity in crossline direction. The red color is the salt body.

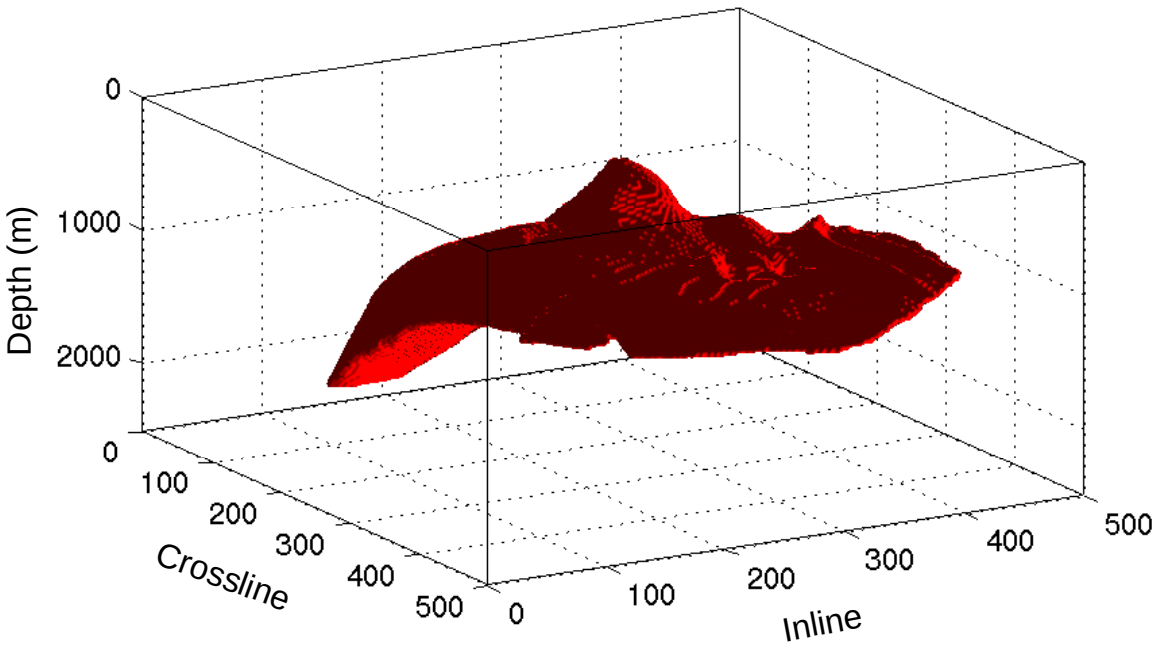

Fig. 19. A 3D view of salt body shown in Figure 18. The red color is the salt body.

in this model is a typical shallow marine environment, sediment velocity gradually increases with depth, and a very complicated salt body (shown in Figure 19) grows into sediment. A flat reflector was added below the salt body to check if we can see the subsalt reflection in the synthetic data.

The synthetic data of the salt model were generated using the 3D acoustic finite-difference modeling program. The data were created by applying absorbing boundary condition instead of free-surface boundary, therefore no free-surface multiples exist in the data. A 10 m $\times$ 10 m $\times$ 10 m cubic grid was used in the finite-difference program, resulting the model that has 560 $\times$ 560 $\times$ 310 grid points. An explosive source (with 10 hz central frequency and 20 hz maximum frequency) was used to generate the waves, and the data was recorded for 3 s with 4 ms sampling interval.

Figure 20 shows an example of shot gathers, the receivers are located along inline 300 shown in Figure 18 with a 10 m receiver interval. Explosive source is located in the center of the line. The data are quite complicated with direct wave, water bottom reflection, top salt reflection, bottom salt reflection, strong diffractions from the salt

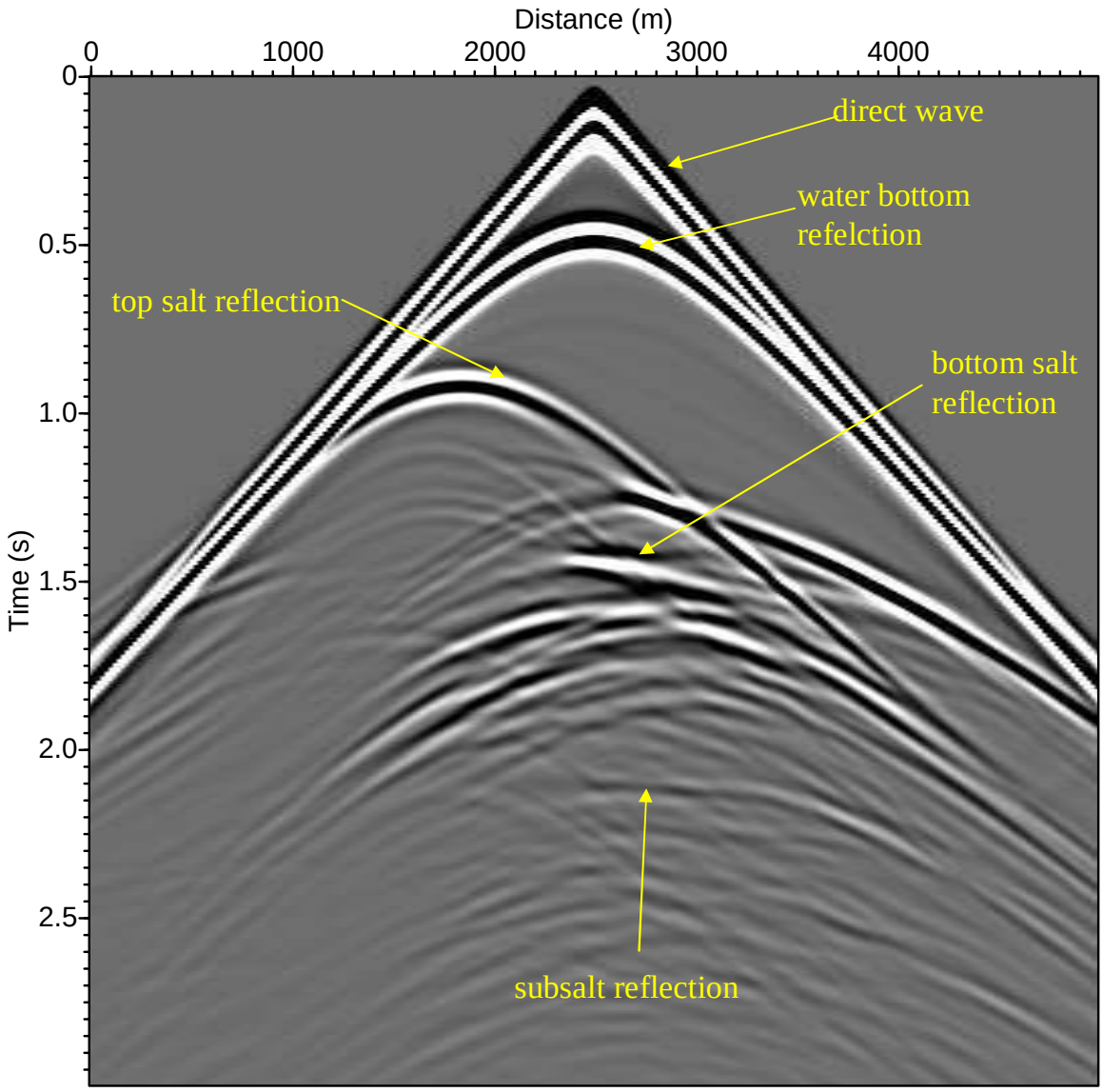

Fig. 20. An example of shot gathers. The receivers are located along inline 300 shown in Figure 18. The receiver interval is 10 m. The shot is located in the middle of the line. Direct wave, water bottom reflection, top salt reflection, bottom salt reflection, diffractions are seen in the data.

body. The subsalt reflection is very weak and arrive around 2.1 s. It is hard to see in the shot gather data, therefore we have identified the subsalt reflection using the arrival time in the zero-offset data, seen in Figure 21.

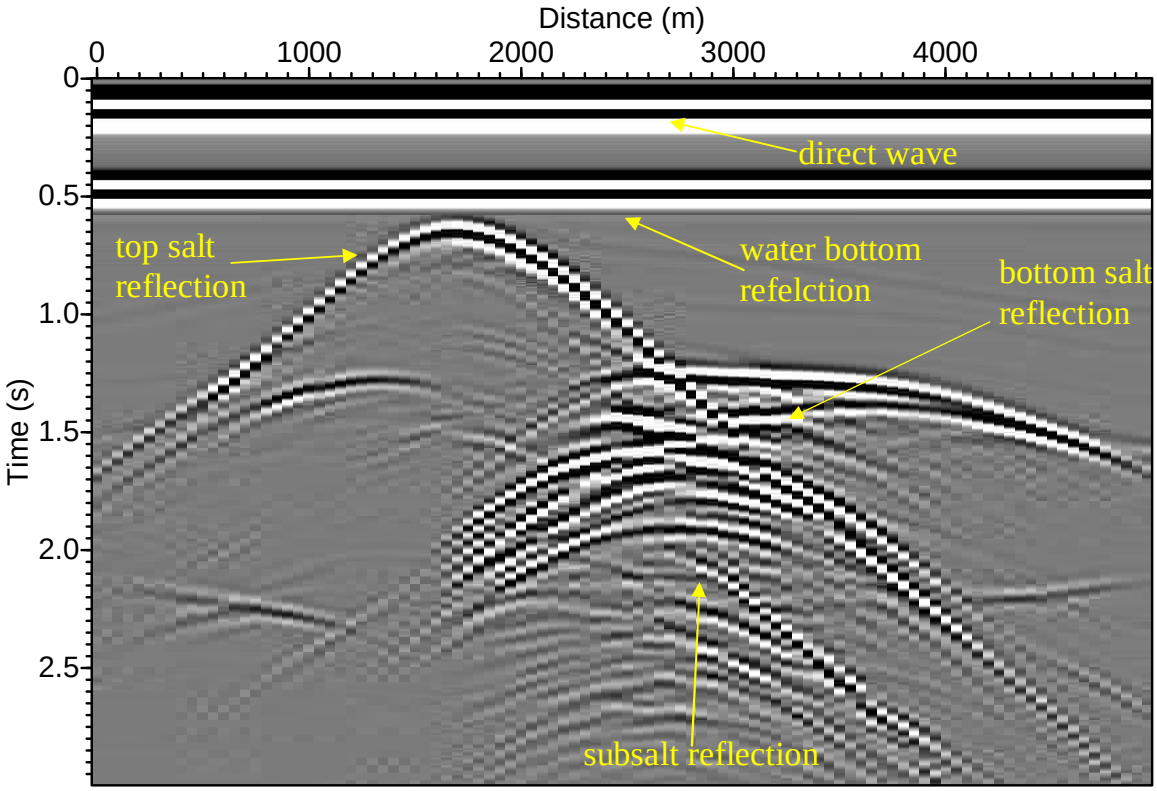

Fig. 21. Zero offset data inline 300 shown in Figure 18. 100 shots total with 50 m shot interval. Direct wave, water bottom reflection, top salt reflection, bottom salt reflection, diffractions, and subsalt reflection are clearly seen in the data.

Figure 21 shows an example of zero-offset data inline 300 as shown in Figure 18. 100 shot gathers with 50 m shot interval along the line were generated. We can see clearly water bottom reflections, top salt reflections, bottom salt reflections, subsalt reflections in Figure 21 as zero-offset data follow the geological structures. Diffractions are very strong because of the salt body; the subsalt reflections are still weak even after boosting the amplitude when plotting the data.

Figure 22 shows another example of zero-offset data crossline 250 (see Figure 18). 100 shot gathers with 50 m shot interval along the line were generated. We

can clearly see water bottom reflections, top salt reflections, bottom salt reflections, and subsalt reflections in Figure 22. The out-of-plane salt reflection is also present in the data generated by the 3D finite-difference modeling program. We have also generated the zero-offset data in the same crossline by using the 2D finite-difference modeling program shown in Figure 23, the out-of-plane salt reflection is not present in the 2D data. Modeling of the out-of-plane events is one of the advantages of the 3D finite-difference modeling program.

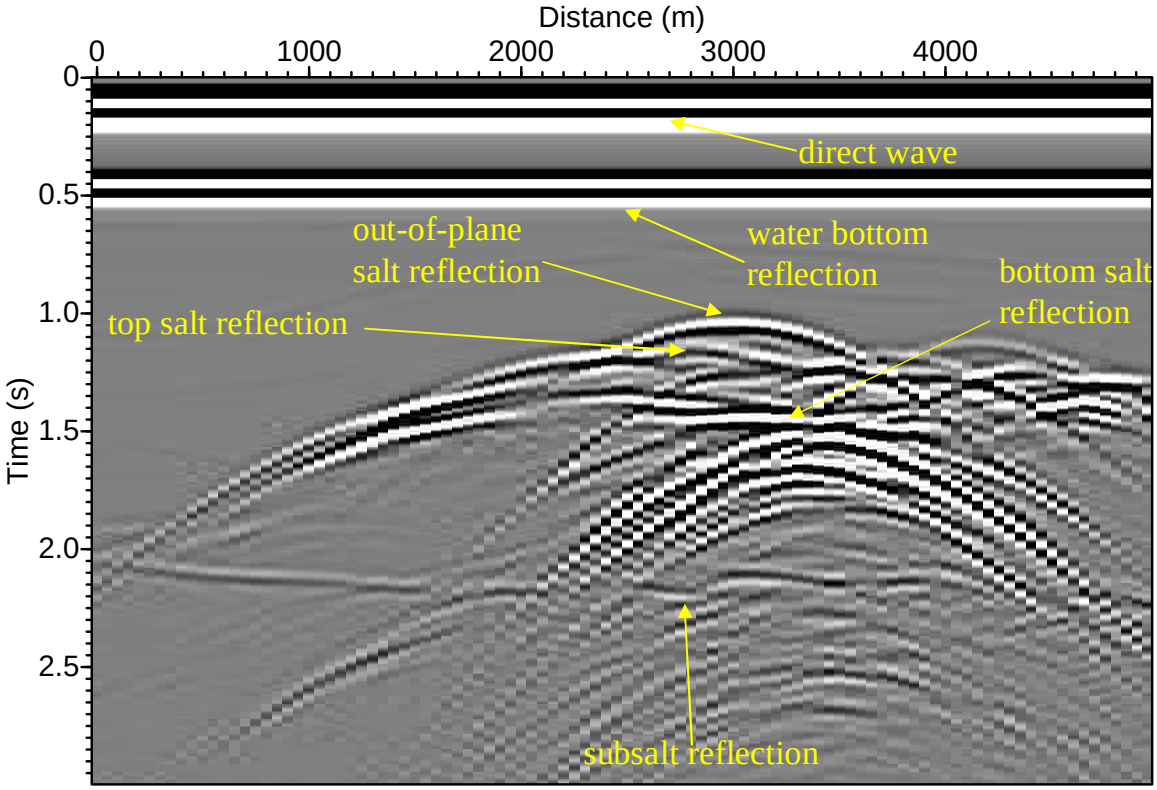

Fig. 22. Zero offset data crossline 250 shown in Figure 18. 100 shots total with 50 m shot interval. Direct wave, water bottom reflection, top salt reflection, bottom salt reflection, diffractions, and subsalt reflection are clearly seen in the data. Out-of-plane salt reflection is also present in the data.

Comparing Figure 21 with Figure 22, we can see that the subsalt reflections are very weak and hard to see when the salt body is thick. This is because that very little energy can penetrate the salt body and reach the subsalt reflector when the salt body is thick, therefore very poor signal to noise ratio below the salt body. This is

the main reason that makes subsalt imaging is so challenging.

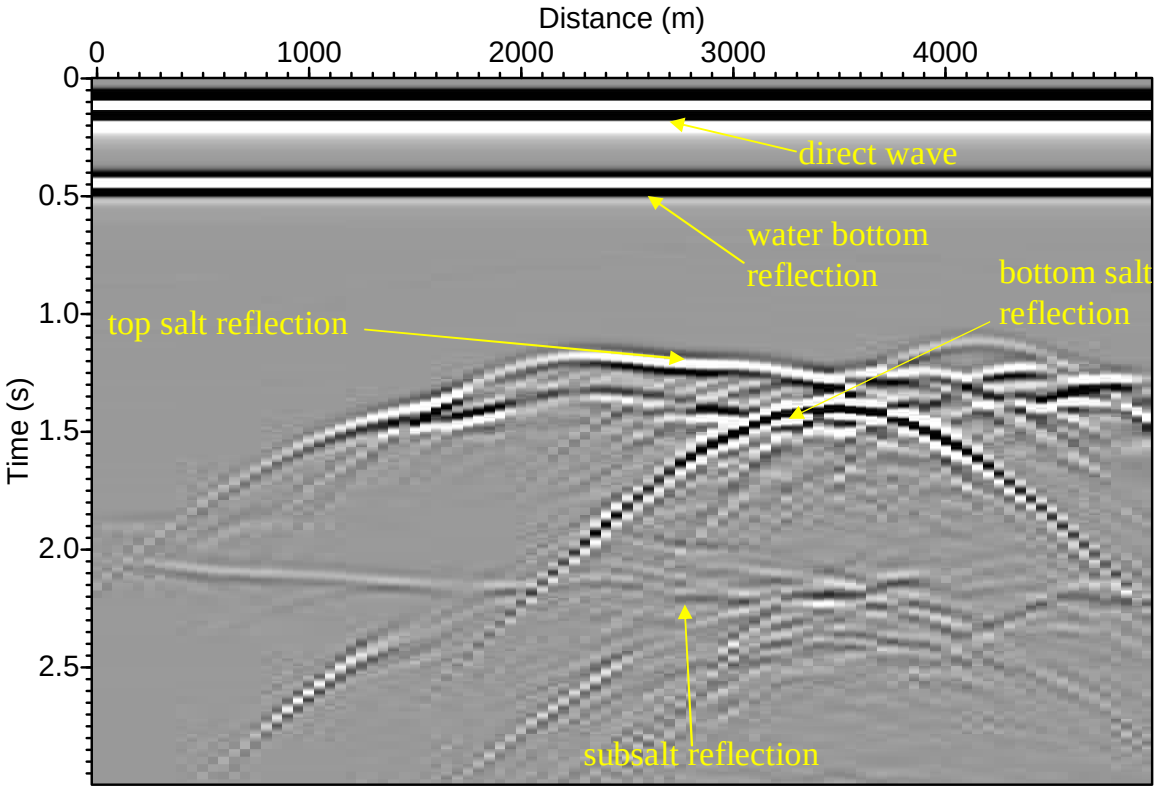

Fig. 23. Zero offset data crossline 250 shown in Figure 18 generated by 2D finite-difference modeling. 100 shots total with 50 m shot interval. Water bottom reflection, top salt reflection, bottom salt reflection, diffractions, and subsalt reflection are clearly seen in the data. Note that the direct waves have been removed from the data.

Finally, it is important to point out that the reason why the 3D finite-difference method is not yet a classical modeling tool for seismic survey design is that it is quite numerically intensive. For example, the salt model discussed above has a grid size of $560 \times 560 \times 310$, data is recorded for 3 s, which is equivalent to 3,000 time steps in 3D finite-different program. It took about 6 hours to generate one shot gather when the code is running parallel on 8 cpus in a specially designed V880-Sun-Microsystems computer. For zero-offset data with 100 shots total shown in Figures 21 and 22, the computing time is 600 hours for each zero-offset data. Generating the full gathers of the salt model requires 60,000 hours computing time using the computers we currently have in the CASP group.

ANISOTROPIC MODEL

Certain wave propagation phenomena can only be seen by using 3D modeling tool, especially a 3D finite-difference modeling tool. Such phenomenon include shear-wave splitting and triplication which are important for fracture characterization. In this section I will apply the finite-difference tool on an anisotropic medium, showing that we can successfully model anisotropy, shear-wave splitting and triplication.

In this section I will study the simplest anisotropic symmetry system called transversely isotropy (TI). In the TI medium the property of the medium only depends on the angle between that direction and the symmetry axis (The properties are independent of the direction in the plane perpendicular to the symmetry axis). Due to the symmetry axis in the TI medium, only 5 stiffness constants are independent. The symmetry direction is usually associated with gravity or regional stress. If gravity is the dominant factor, the symmetry axis will be vertical, and we have a VTI model. If regional stress is dominant factor, the symmetry axis can be horizontal, in this case we have a HTI model.

The terminology of quasicompressional (qP-wave) and quasishear (qS-wave) waves will be used in discussing the P and S waves in VTI and HTI medium. (Winterstein, 1989) provided the following regarding for qP, qSV, and qSH waves terminology in anisotropic medium. In isotropic media, wave polarization is either parallel or perpendicular to direction of travel. In anisotropic media, they are so only for the special direction of travel. Hence, in general, wave propagations are neither strictly parallel or perpendicular to the propagation direction. The waves are denoted qP, qSV, and qSH, as appropriate, where q indicates quasi-. Quasi means similar but not exactly.

VTI medium

VTI is the transversely isotropy with a vertical symmetry axis. Rock formation with VTI symmetry can be described by a five independent stiffness constants. The

stiffness tensor of the VTI medium is

$$[C] = \begin{bmatrix} C_{11} & C_{11}-2C_{66} & C_{13} & 0 & 0 & 0 \\ C_{11}-2C_{66} & C_{22} & C_{13} & 0 & 0 & 0 \\ C_{13} & C_{13} & C_{33} & 0 & 0 & 0 \\ 0 & 0 & 0 & C_{44} & 0 & 0 \\ 0 & 0 & 0 & 0 & C_{44} & 0 \\ 0 & 0 & 0 & 0 & 0 & C_{66} \end{bmatrix}. \tag{4.1}$$

with the energy constraint that (Ikelle and Amundson, 2005)

$$\begin{aligned} & C_{11} \geq C_{66} \geq 0 \\ & C_{33} \geq 0 \\ & C_{44} \geq 0 \\ & {C_{13}}^2 \leq C_{33}(C_{11}-C_{66}). \end{aligned} \tag{4.2}$$

The energy constraint in equation (4.2) ensures that P-waves are always faster than S-waves in a given direction (Ikelle and Amundson, 2005).

Let us look at the wave propagation in a homogeneous VTI model with the stiffness tensor

$$\frac{1}{\rho}[C](km^2/s^2) = \begin{bmatrix} 5.29 & 1.91 & 2.62 & 0 & 0 & 0 \\ 1.91 & 5.29 & 2.62 & 0 & 0 & 0 \\ 2.62 & 2.62 & 4.20 & 0 & 0 & 0 \\ 0 & 0 & 0 & 1.21 & 0 & 0 \\ 0 & 0 & 0 & 0 & 1.21 & 0 \\ 0 & 0 & 0 & 0 & 0 & 1.69 \end{bmatrix}. \tag{4.3}$$

with $\rho = 2.5$ g/cm^3. We have propagate the seismic waves through this VTI model, the resulting wavefronts are shown in Figures 24 and 25.

Figure 24 shows the snapshots of wave propagation corresponding to the qP-

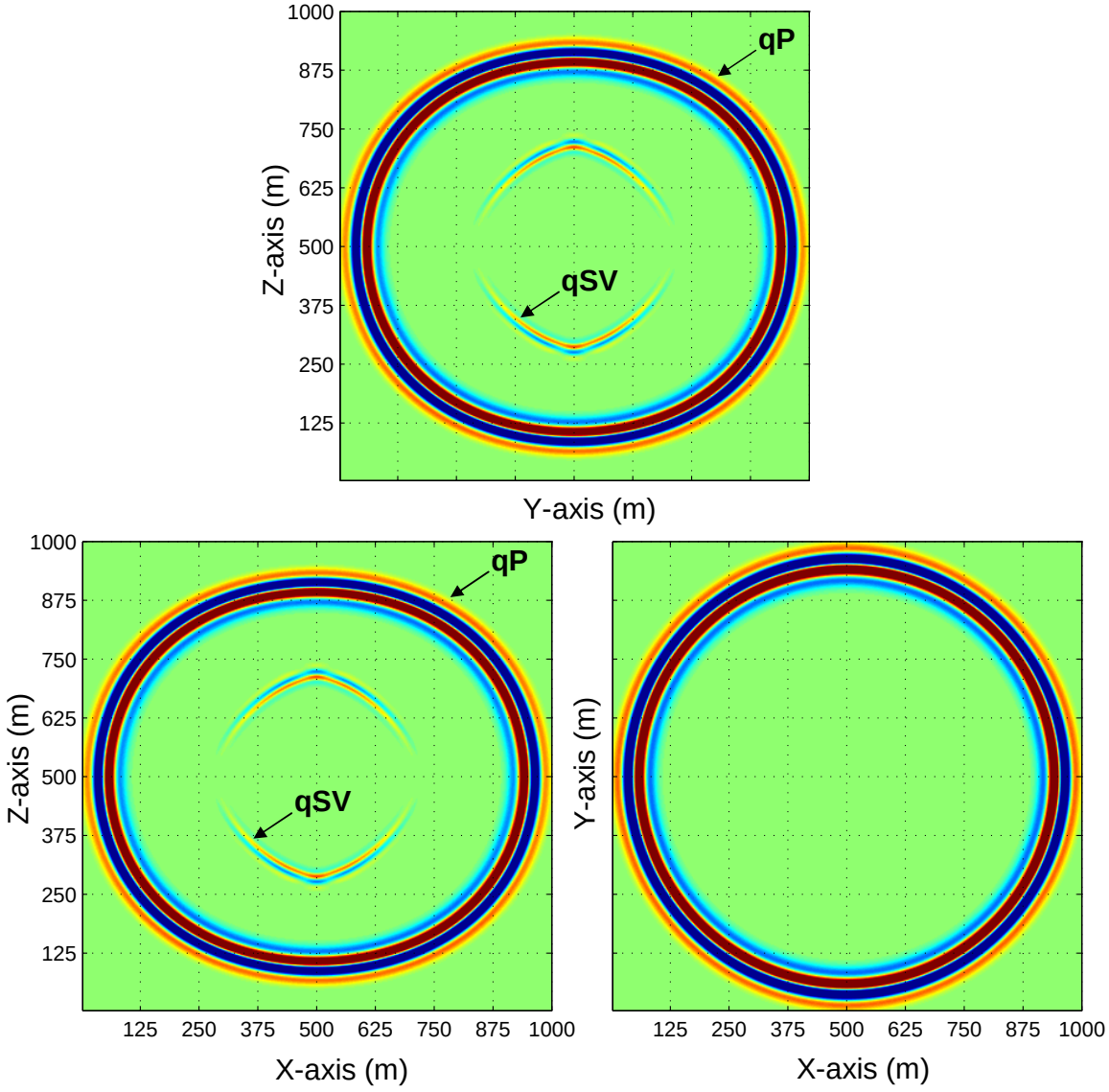

Fig. 24. Snapshots of wave propagation for measurements of volumetric deformation using an explosive source in a VTI medium. Properties of the medium are defined in equation (4.3). The source used to generate waves is an explosive source. Snapshots were taken at 225 ms. The physical quantities displayed here is volumetric deformation. Three orthogonal planes which intersect at the source location are displayed here: Y-Z plane, X-Z plane, and X-Y plane. Notice the arrival times are variant with the direction of propagation in the X-Z plane and Y-Z plane. In the X-Y plane the arrival times are invariant with direction.

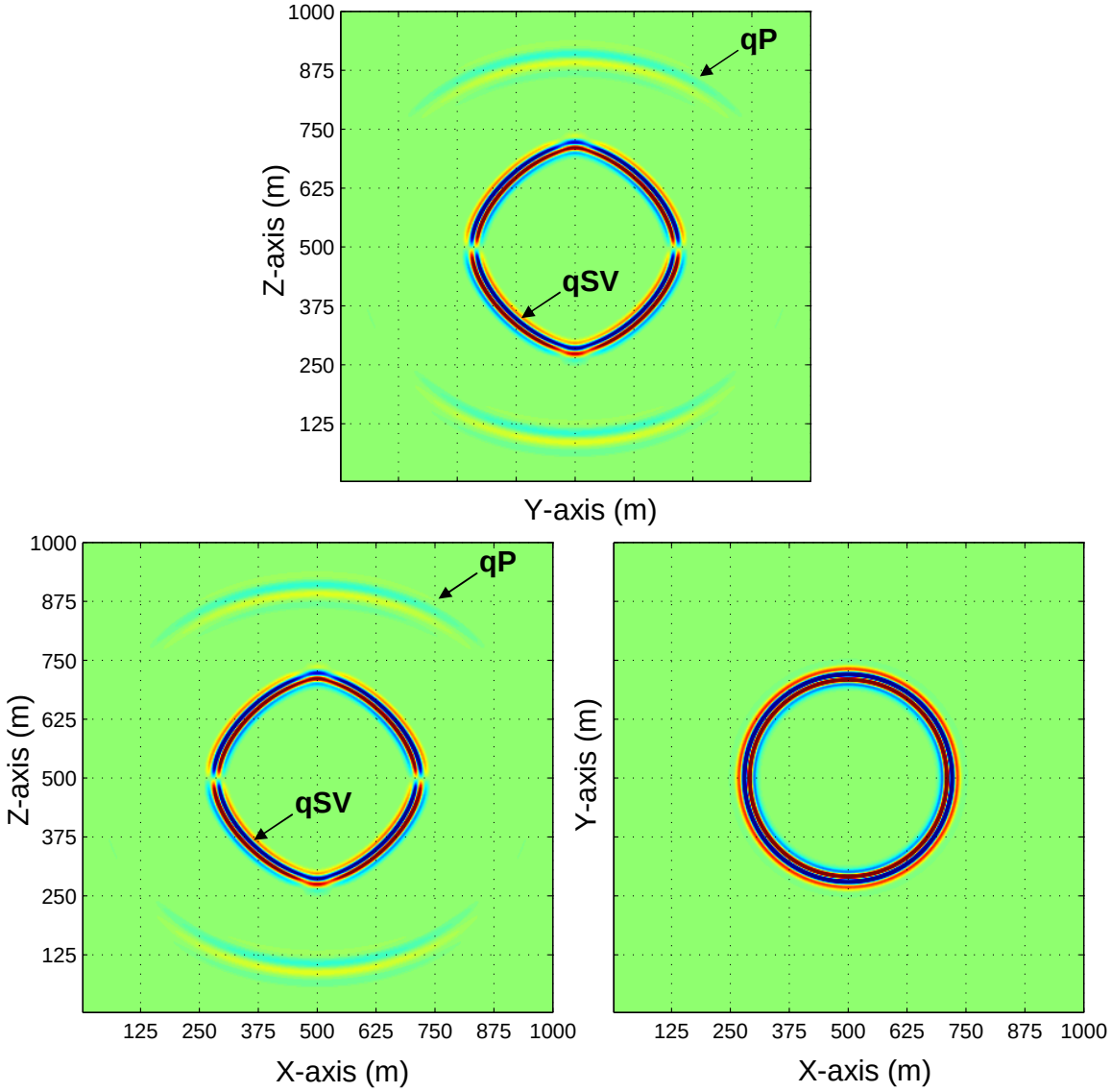

Fig. 25. Snapshots of wave propagation for measurements of v_z using an S-wave source in a VTI medium. Properties of the medium are defined in equation (4.3). The source used to generate waves is a predominantly S-wave source (see Appendix A for detail). Snapshots were taken at 225 ms. The physical quantities displayed here is v_z. Three orthogonal planes which intersect at the source location are displayed here: Y-Z plane, X-Z plane, and X-Y plane. Notice the arrival times are variant with the direction of propagation in the X-Z plane and Y-Z plane. In the X-Y plane the arrival times are invariant with direction.

waves in the VTI model. In Figure 24, we can see qP-waves travel faster in the horizontal direction in the vertical direction than in the X-Z plane and Y-Z plane. The medium behaves anisotropically as expected. These observations also confirm that the waves propagate faster where the resistance to deformation is weakest. Figure 24 shows that qP wavefronts in the X-Y plane are invariant with direction, this also conforms the characteristic of VTI model.

Figure 25 shows the snapshots of wave propagation corresponding to the qS-waves in the VTI model, where we can see that the horizontal and vertical speed are the same in Figure 25. This is because that qS-waves are basically polarized in the X-Y plane parallel to the direction of wave propagation, the medium property is invariant in X-Y plane in a VTI model. However, for an intermediate angle between 0 and 90^o, the speed of qS-waves decreases because the medium is anisotropic in that direction of propagation. The travel time for qS waves is invariant with direction of propagation in the X-Y plane, this is because the VTI medium is azimuthally isotropic.

HTI medium

HTI is the transversely isotropy with a horizontal symmetry axis. Rock formation with HTI symmetry can be described by a five independent stiffness constants. The stiffness tensor of the HTI medium is

$$[C] = \begin{bmatrix} C_{11} & C_{13} & C_{13} & 0 & 0 & 0 \\ C_{13} & C_{33} & C_{33} - 2C_{44} & 0 & 0 & 0 \\ C_{13} & C_{33} - 2C_{44} & C_{33} & 0 & 0 & 0 \\ 0 & 0 & 0 & C_{44} & 0 & 0 \\ 0 & 0 & 0 & 0 & C_{66} & 0 \\ 0 & 0 & 0 & 0 & 0 & C_{66} \end{bmatrix}. \tag{4.4}$$

Let us look at the wave propagation in a homogeneous HTI model with the

stiffness tensor

$$\frac{1}{\rho}[C](km^2/s^2) = \begin{bmatrix} 5.29 & 2.62 & 2.62 & 0 & 0 & 0 \\ 2.62 & 4.20 & 1.78 & 0 & 0 & 0 \\ 2.62 & 1.78 & 4.20 & 0 & 0 & 0 \\ 0 & 0 & 0 & 1.21 & 0 & 0 \\ 0 & 0 & 0 & 0 & 1.69 & 0 \\ 0 & 0 & 0 & 0 & 0 & 1.69 \end{bmatrix}. \tag{4.5}$$

with $\rho = 2.5$ g/cm^3. We have propagate the seismic waves through this HTI model, the resulting wavefronts are shown in Figures 26 and 27.

Figure 26 shows the snapshots of wave propagation corresponding to the qP-waves in the HTI model. In Figure 26 we can see that qP-waves travel faster in the x direction in X-Z plane and X-Y plane where particle motion is aligned with the medium's maximal stiffness direction. qP wavefronts are invariant with direction in the Y-Z plane, qP velocity is slower on this plane, which is the opposite of VTI behavior. It is because the maximal stiffness direction of VTI is different to that of HTI.

Figure 25 shows the snapshots of wave propagation in the HTI model with a shear source. Besides the travel time anisotropy of qP and qS waves we have seen in Figure 25, in Figure 27 we see a new phenomenon that qS-wave has splitted into two components qSV and qSH (a phenomenon known as shear-wave splitting). This phenomenon is also observed in field data where the shear-wave splits when it passes through the fractures.

(Ikelle and Amundson, 2005) provided an explanation of the shear-wave splitting phenomenon. An S-wave of arbitrary polarization entering into an anisotropic region can split into two S-waves, and the particle motion can be polarized in both medium's stiff (fast) direction and the compliant direction. The split waves with differently polarized motion arrive at their destination at different time. Splitting occurs

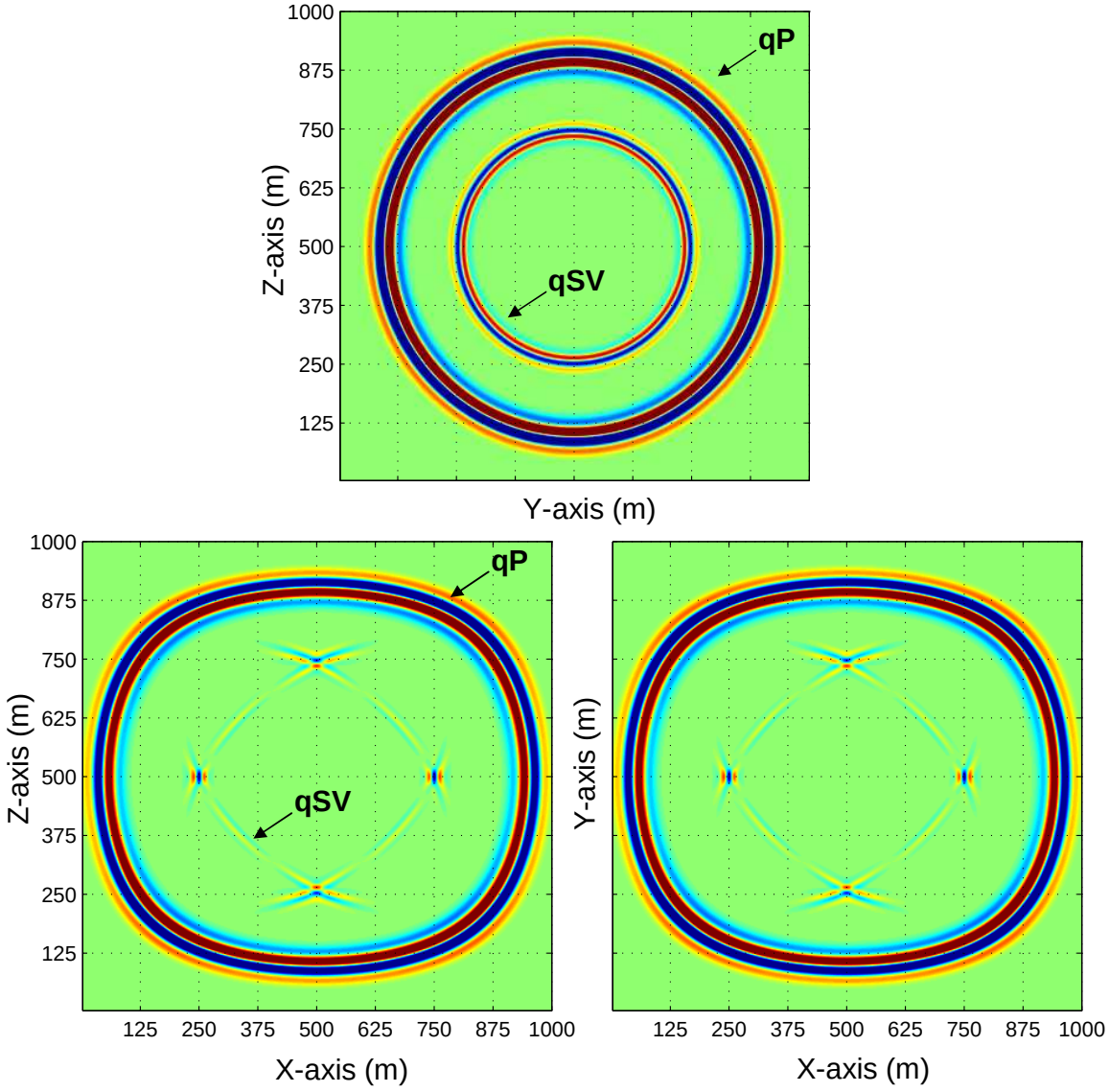

Fig. 26. Snapshots of wave propagation for measurements of volumetric deformation using an explosive source in a HTI medium. Properties of the medium are defined in equation (4.5). The source used to generate waves is an explosive source. Snapshots were taken at 225 ms. The physical quantities displayed here is volumetric deformation. Three orthogonal planes which intersect at the source location are displayed here: Y-Z plane, X-Z plane, and X-Y plane. Notice the arrival times are variant with the direction of propagation in the X-Z plane and X-Y plane. In the Y-Z plane the arrival times are invariant with direction.

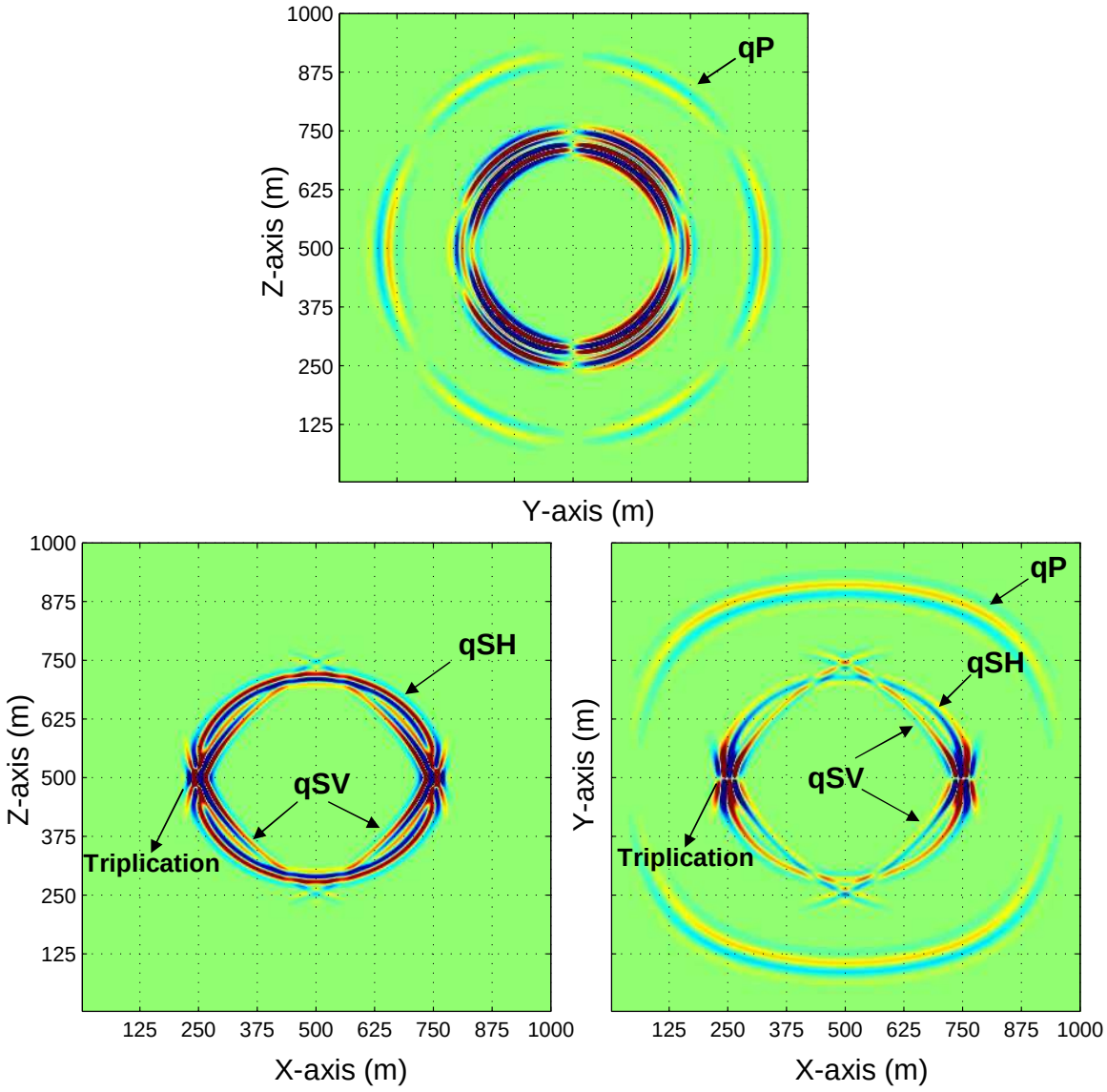

Fig. 27. Snapshots of wave propagation for measurements of v_y using an S-wave source in a HTI medium. Properties of the medium are defined in equation (4.5). The source used to generate waves is a predominantly S-wave source. Snapshots were taken at 225 ms. The physical quantities displayed here is v_y. Three orthogonal planes which intersect at the source location are displayed here: Y-Z plane, X-Z plane, and X-Y plane. Notice the arrival times are variant with the direction of propagation in the X-Z plane and X-Y plane. In the Y-Z plane the arrival times are invariant with direction. qS-wave has splitted into two components qSV and qSH (a phenomenon known as shear-wave splitting). The phenomenon of triplication (energy traveling in the same direction with more than one velocity) is also shown in the data.

when shear-waves travel horizontally through a VTI medium or vertically through a fractured HTI medium. Shear-wave splitting is more evident in data corresponding to HTI media than those to VTI media because most seismic acquisition are designed that the waves propagates predominantly vertically.

Shear-wave splitting is very useful for detecting the orientation and density of fractures, the time delay between the fast and slow S-waves is proportional to the intensity of fractures, shear-wave splitting can also be used to detect orientation of anisotropy in the rocks.

Another phenomenon we see in Figure 25 is the triplication, a phenomenon in which the wave energy travels in the same direction with more than one velocity. Triplication has been observed in the actual data acquisition. Triplication will cause a problem when the data are migrated, because of more than one velocity in the same direction.

SUMMARY

In this chapter I have shown applications of finite-difference modeling on a complex salt model of Gulf of Mexico and on an anisotropic medium. I have shown that the finite-difference program can be a tool for illumination and survey design. We have successfully modeled travel-time anisotropy, shear-wave splitting and triplication in anisotropic medium using the 3D finite-difference program. We also point out that 3D finite-difference modeling is an expensive tool, which is the reason that it is still not widely used in exploration and production industry.

CHAPTER V

SCATTERING DIAGRAMS IN SEISMIC IMAGING: MORE INSIGHTS INTO THE CONSTRUCTION OF VIRTUAL EVENTS AND INTERNAL MULTIPLES

OVERVIEW

The key processes in marine seismic imaging include (i) removing from seismic data all seismic events (free-surface multiples and ghosts) which contain at least one reflection at the sea surface in their wave-propagation path, and leaving those with no reflection at the free surface (internal multiples and primaries), (ii) removing events with at least two reflections in the subsurface (internal multiples), and leaving events with only one reflection in the subsurface (primaries), and then (iii) locating the scattering points and reflectors inside the subsurface which are the sources of primaries and internal multiple events. All these processes are here explained, derived, and optimized via scattering diagrams (diagrammatica) in a way similar to the way the quantum field theory is often explained via Feynman diagrams. Our discussion of the removal of events with free-surface reflections from the data will be brief, as the diagrammatica of these events are now well understood.

The main focus of this paper is the diagrammatica of internal multiples and primaries. Although these events do not contain any reflection at the sea surface, it is important to reconstruct them with scattering points near the sea surface, where seismic data are recorded. So our diagrammatica of primaries and internal multiples include events which are not directly recorded in seismic data but which can be constructed from seismic data. These events have allowed us to construct scattering diagrams of primaries and internal multiples with scattering points near the sea surface. Furthermore, these new diagrammatica of internal multiples and primaries can be used to remove internal multiples from the data.

PUTTING SCATTERING DIAGRAMS TO WORK

Examples of the wave-propagation paths which constitute towed-streamer data are depicted in Figure 28. These events can be grouped into three categories: primaries, free-surface-reflection events (ghosts and free-surface multiples), and internal multiples. Primaries are seismic events which reflect or diffract only once in the subsurface, but not at the free surface, before being recorded. Free-surface-reflection events (ghosts and free-surface multiples) are events with at least one reflection at the sea surface in their wave-propagation path. When the first and/or last reflection in the wave-propagation path of a free-surface-reflection event is at the sea surface, the events are characterized as ghosts. All the other free-surface-reflection events are characterized as free-surface multiples. Internal multiples are seismic events with no reflection at the free surface but with reflections between two interfaces other than the free surface. Two types of events in seismic data that do not readily fall into the three categories that we have defined are head waves and direct waves. We treat head waves here as internal multiples and direct waves as primaries.

The key processes involved in marine seismic imaging (which are at the heart of modern oil and gas exploration and production) include (i) removing free-surface-reflection events from the data and leaving primaries and internal multiples, (ii) removing internal multiples from the data and leaving primaries, and then (iii) locating the scattering points and reflectors in the subsurface, which are the sources of primaries and internal multiples in particular. Our objective in this paper and in the subsequent ones is to show that all these processes can be explained, derived, and "optimized" using scattering diagrams (diagrammatica) in a way similar to the way the quantum field theory is often explained using Feynman diagrams. Our description of the optimization of seismic processes will become clearer in the next paragraph. Note that diagrammatica here mean a collection of scattering diagrams used to describe seismic events. We obviously expect this collection to grow significantly in the

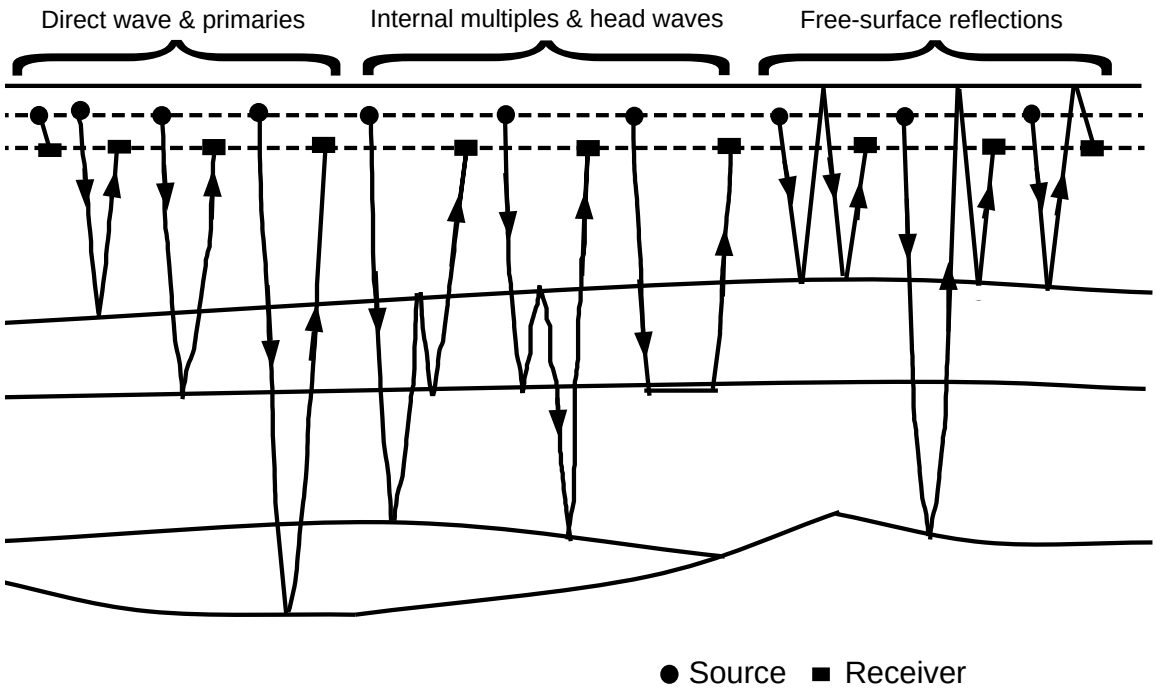

Fig. 28. Examples of the scattering diagrams for direct wave, primaries, free-surface reflections, and internal multiples.

coming years in a way that will enable us to describe the entire field of petroleum seismology through scattering diagrams.

Before we describe the convention used in drawing our scattering diagrams, let us recall that solutions of wave equations (the building blocks of seismology) involve waves traveling in positive as well as negative time, the so-called "retarded" and "advanced" waves. Retarded waves progressively move with increasing time, as visualized in the classical movies of wave propagation (e.g., (Ikelle and Amundson, 2005)). They are consistent with the way current seismic data acquisitions are carried out; they arrive at receiver locations at some time after they have left the source location. Advanced waves travel backward in time; that is, they arrive at the hydrophones or geophones before they have left the source point. These waves are really an affront to our common sense and our understanding of how the world operates—our ever-aging bodies being an obvious testimony. So despite the fact that advanced waves are valid solutions to the wave equations, they are generally ignored in most seismology

studies, at least in part, because of their counterintuitive nature. One of the key features of our diagrammatica here is that these advanced waves are included in our constructions of the scattering diagrams of seismic events.

In our scattering diagrams, such as the ones in Figure 29, the process of wave propagation begins on the left and ends on the right. The solid line represents waves traveling forward in time (forward wave propagation), and the dotted line represents waves traveling backward in time (backward wave propagation). In forward wave propagation, the process begins on the left and ends on the right, whereas in backward wave propagation, it is the opposite. The arrows are added in these scattering diagrams to clearly indicate the direction of wave propagation. The point at which the two lines meet is known as the scattering point. Scattering points can occur at the intersection of two solid lines, of two dotted lines, or of a solid line and a dotted line. The time is not explicitly shown in the scattering diagrams of this paper in order to avoid an unnecessary complication associated with a third axis. Notice that all events recorded in seismic data (i.e., direct waves, primaries, ghosts, and multiples) have a forward propagation. Therefore, in our diagrammatica, these events will be marked entirely by solid lines and will go from left to right. We will call them "real events." Their noncausal versions, which correspond to backward propagation, will be marked by dotted lines and will go from right to left. We will call them "anticausal events." Events which combine solid and dotted lines in their constructs will appear only in intermediate, unobservable stages of a process for constructing a real event. We will call these events "virtual events," as suggested by (Ikelle, 2004), (Ikelle and Gangi, 2005).

As we can see in Figure 29, it is always possible to construct free-surface-reflection events by combining wave-propagation paths of events contained in the same seismic data because the wave-propagation paths of free-surface-reflection events contain at least one reflection point at the sea surface. That is not the case for internal multiples

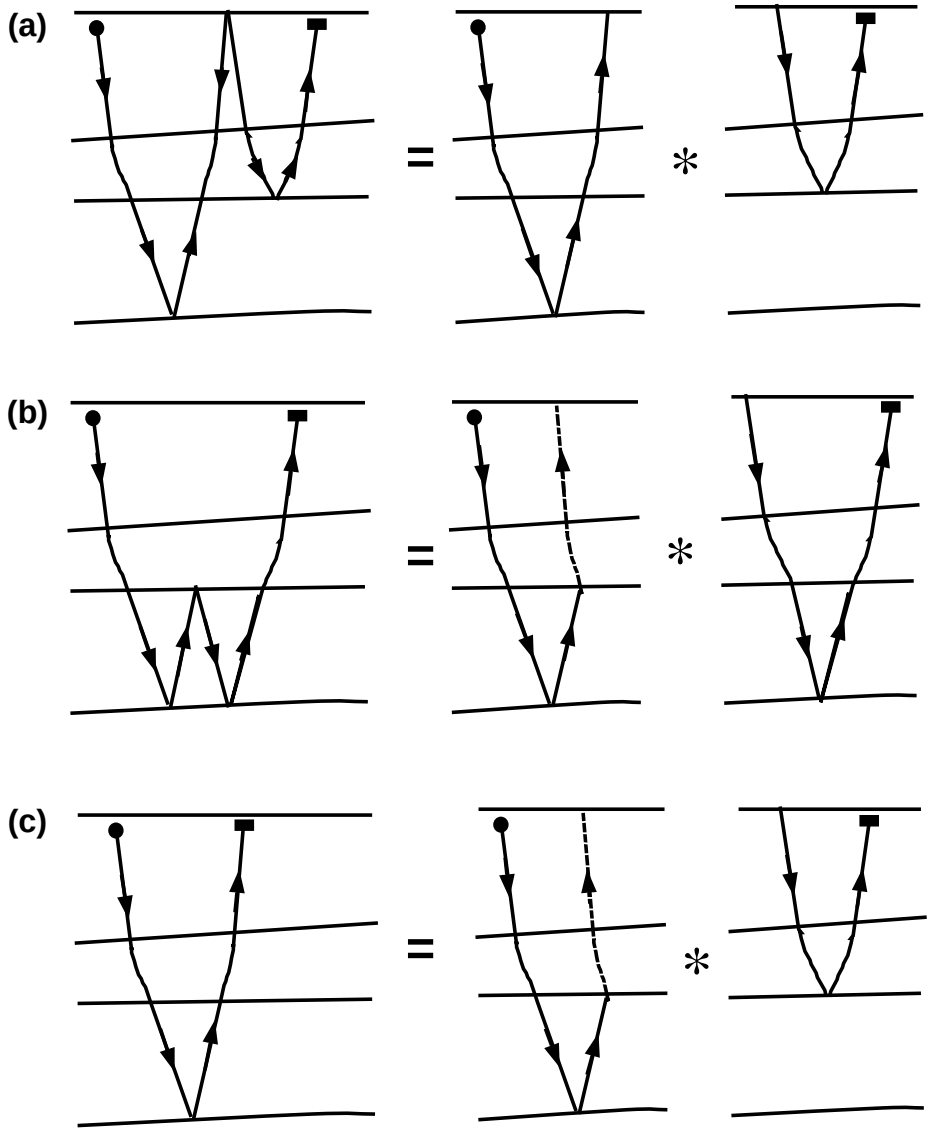

Fig. 29. Examples of constructions of primaries, free-surface multiples, and internal multiples using scattering diagrams. In these scattering diagrams, like the ones in the remaining figures in this paper, the process of wave propagation begins on the left and ends on the right. The solid line represents waves traveling forward in time, and the dotted line represents waves traveling backward in time. (a) A combination of two primaries is used to predict a first-order multiple. Notice that it is always possible to construct free-surface-reflection events by combining the wave-propagation paths of two real events contained in the same seismic data because the wave-propagation paths of free-surface-reflection events contain at least one reflection point at the sea surface. (b) A combination of a primary with a virtual event can produce an internal multiple. (c) This combination can also produce primaries. Notice that the virtual event allows us to compensate for the fact that internal multiples and primaries do not contain free-surface reflection points.

and primaries. For example, to compensate for the fact that internal multiples do not contain free-surface-reflection points in their wave-propagation paths, the technology commonly used today in the oil and gas industry for constructing internal multiples, developed by (Berkhout and Verschuur, 2005), requires that the internal-multiple-generating reflectors be known, say, through interpretation of data. For the same reason, current migration methods used for locating the scattering points and reflectors in the subsurface from the field of primaries also require knowledge of a smooth-background-velocity model. This smooth-velocity model is used to extrapolate data acquired near the sea surface to the scattering points inside the subsurface, where there is no receiver.

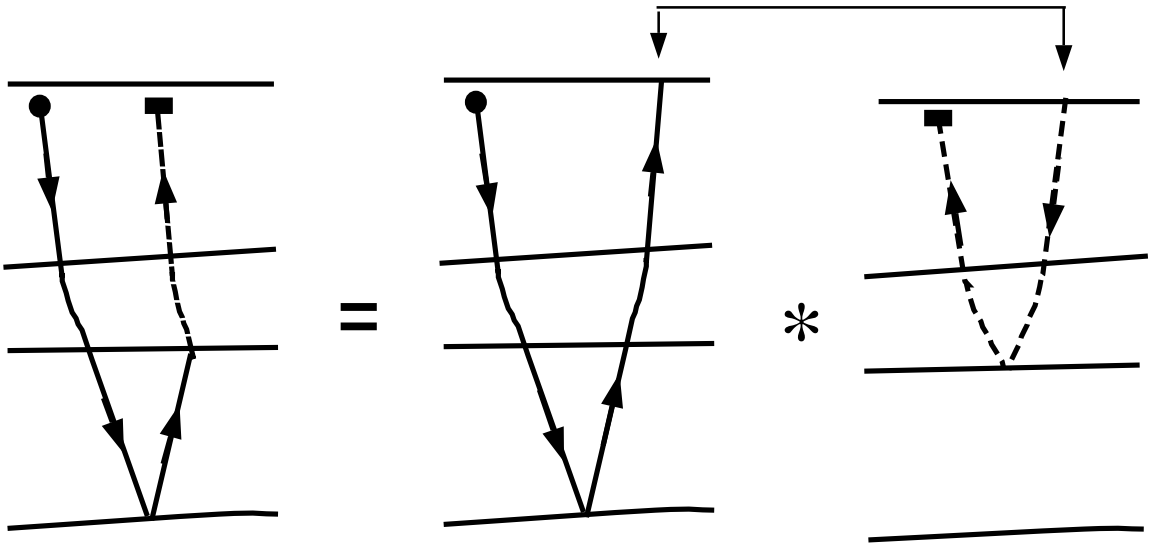

Fig. 30. An illustration of the construction of virtual seismic data as a combination of two primaries in which one of the primaries has been time-inverted.

So in addition to removing multiples from the data and leaving only primaries, modern seismic imaging methods also require the estimation of a smooth-velocity model of the subsurface before applying migration algorithms to seismic data. By using the concept of virtual events introduced by (Ikelle, 2004), (Ikelle and Gangi, 2005), we here show that internal multiples and primaries can be constructed with the scattering point at the sea surface, just like free-surface multiples, as depicted

in Figures 29 and 30. Furthermore, this concept can be used to remove internal multiples from the data. In a paper in preparation, it is also used to develop methods for locating the scattering points and reflectors in the subsurface in which velocity estimation and migration are combined. In other words, this concept of virtual events can be used not only to improve our understanding of the construction of internal multiples and primaries but also to develop more-optimal imaging solutions. Again, note that virtual events are not directly recorded in seismic data, but they can be constructed from seismic data by time-inverting one of the two fields used in their constructions (see Figure 30).

Let us remark that one can establish an analogy between virtual events and the concept of virtual particles in quantum field theory. Just like virtual events, virtual particles are theoretical particles that cannot be detected directly but are nonetheless a fundamental part of quantum field theory [see (Ikelle and Gangi, 2005) and (Ikelle and Gangi, 2007) for more details]. These authors also discussed the connection between virtual events and the notion of negative refraction in optics. This notion is generally attributed to (Veselago, 1968), who first hypothesized that the material with a negative refractive index could exist so that light entering a material with a negative refractive index from a material with a positive refractive index will bend in the opposite direction of the usual observation. The similarities between the last two legs of the virtual events and the path of negative refraction are described in these papers.

Our discussion of these various constructs of seismic events will center on the convolution-type and crosscorrelation-type representation theorems, as derived, for example, in (Bojarski, 1983), (de Hoop, 1995), and (Gangi, 1970). Other studies, especially those related to multiple attenuation and up/down wavefield separation, have used the convolution-type representation theorem as the starting point of the development of their solutions. They include (Kennett, 1979), (Fokkema and van den Berg,

1990) and (Fokkema and van den Berg, 1993), (Ziolkowski et al., 1999), (Amundsen, 2001), (Amundsen et al., 2001), and (Ikelle et al., 2003). We have included Fokkema and van den Berg (1990, 1993) in the list, although their starting point is actually the convolution-type reciprocity theorems from which the convolution-type representation theorem can be deduced. One of the novelties here is our use of both the crosscorrelation-type and convolution-type representation theorems in our constructs of the scattering diagrams of seismic events.

This paper differs from (Ikelle, 2006), and Ikelle and Gangi (2005 and 2007). In Ikelle (2006), the results are purely intuitive, not rooted in any physical theorem. In Ikelle and Gangi (2005 and 2007), we show that the intuitive solution described in Ikelle (2006) can actually be described from the representation theorem. We also extends this discussion to Snell's law and sometimes to a material-science point of view. Although this paper takes advantage of our previous formulation of the representation theorem, it focuses on the construction of the scattering diagrams (diagrammatica) of seismic events by combining forward and backward wave propagation. We illustrate the applicability of these constructs with numerical examples generated by finite-difference modeling. We also use analytic derivations for an 1D model to explain these constructs. None of these items is described in our previous publications.

Let us also note that (van Manen et al., 2005) have also recently used the crosscorrelation-type representation theorem for improving the computation time of finite-difference modeling. (Derode et al., 2003), (Roux and Fink, 2003), (Wapenaar, 2004), and (Snieder et al., 2004) have explicitly or implicitly used the correlation-type reciprocity theorems to retrieve Green's function of inhomogeneous media from wavefield recordings. We also show in this paper that the intuitive results of internal multiple attenuation obtained by Ikelle (2004, 2005) can actually be derived from the crosscorrelation-type representation theory. Although not yet established, the works of (Rickett and Claerbout, 1999) and of (Schuster et al., 2004) on daylight imaging,

and that (Berkhout and Verschuur, 2005) and (Verschuur and Berkhout, 2005) on internal multiple attenuation, can also be related to the crosscorrelation-type representation theorem because, at the very least, they invoke time reversal and the crosscorrelation of wavefields.

WHY THE CURRENT CONSTRUCT OF FREE-SURFACE MULTIPLES DOES NOT READILY EXTEND TO THE CONSTRUCTION OF INTERNAL MULTIPLES AND PRIMARIES

The objective of seismic multiple attenuation (also known as the demultiple procedure) is to transform the data recorded over the actual medium (which consists of a solid half-space overlain by a water layer with an air-water interface—see Figure 31a) to hypothetical data corresponding to the same model without the free surface (air-water interface). That is, the water layer is now infinite, as illustrated in Figure 31b. This transformation includes the prediction of free-surface multiples from the actual data and the removal of predicted free-surface multiples from the actual data. Our goal in this section is to describe this transformation of the data, in particular the aspect related to the construction of free-surface multiples, and to point out why this construct does not readily extend to that of internal multiples. We will start this section by defining some of the notation conventions that we used in this paper.

Position is specified by the coordinates $\{x, y, z\} = \{x_1, x_2, x_3\}$ with respect to a fixed Cartesian reference frame with origin O, and three mutually perpendicular base vectors $\{\mathbf{i}_1, \mathbf{i}_2, \mathbf{i}_3\}$; $\mathbf{i}_3$ points vertically downward. The length of each of these three vectors is 1. The subscript notation for vectors and the Einstein summation convention are adopted. Lowercase Latin subscripts are employed for this purpose (e.g., v_k); they are to be assigned the values 1, 2, and 3 unless specified otherwise. The lowercase Latin subscript r and s are reserved for indicating receiver and source locations, respectively. The Fourier transform of a physical quantity, say, $g(\mathbf{x}, t)$, with

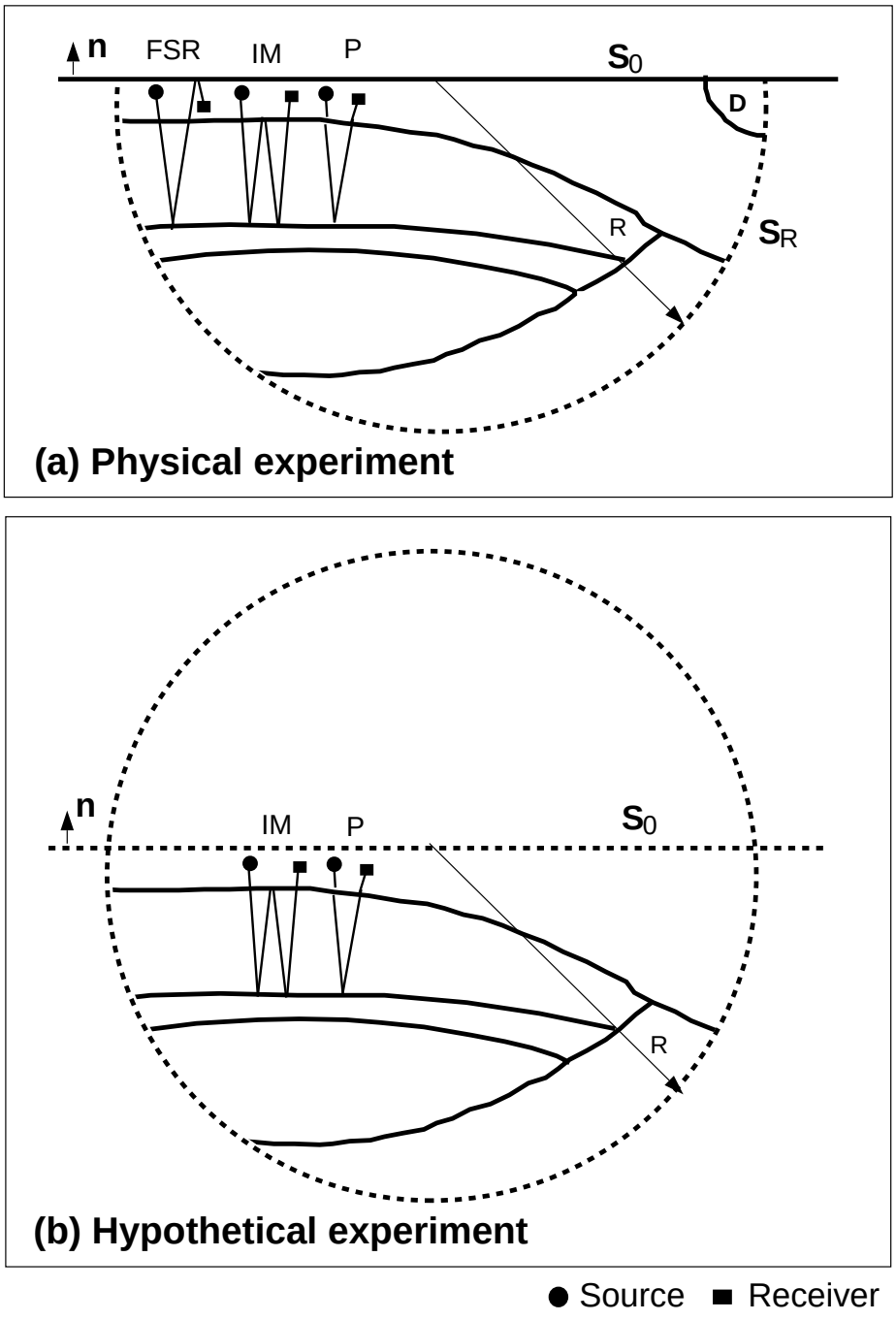

Fig. 31. Geometry of the physical and hypothetical wave-scattering experiments. The surface $S = S_0 + S_R$ with an outward-pointing normal vector $\boldsymbol{n}$ encloses a volume D. (a) In the physical experiment, S_0 is a free surface with vanishing pressure. (b) In the hypothetical experiment, S_0 is a nonphysical boundary. No free-surface reflections are generated. (FSR = free-surface reflections, IM = internal multiple, and P = primary).

respect to time is given by

$$g(\mathbf{x},\omega) = \int_0^{+\infty} g(\mathbf{x},t)\exp\left[-i\omega t\right] dt\,, \tag{5.1}$$

and the inverse Fourier transform is given by

$$g(\mathbf{x},t) = \int_{-\infty}^{+\infty} g(\mathbf{x},\omega)\exp\left[i\omega t\right] d\omega\,. \tag{5.2}$$

Let $P_0(\mathbf{x}_r,\omega;\mathbf{x}_s)$ denote the Fourier transform over time of the recorded pressure field corresponding to the actual medium (Figure 31a) for a receiver at $\mathbf{x}_r$ and a point source at $\mathbf{x}_s$, and let $P_P(\mathbf{x}_r,\omega;\mathbf{x}_s)$ denote the hypothetical pressure field corresponding to a medium with an infinite water layer (Figure 31b). These fields can be related, via the representation theorem [e.g., (de Hoop, 1966), (de Hoop, 1995), (Gangi, 1970), (Aki and Richards, 1980), and (Ikelle and Amundson, 2005)], as follows:

$$\begin{aligned} P_0(\mathbf{x}_r,\omega;\mathbf{x}_s) =& P_P(\mathbf{x}_r,\omega;\mathbf{x}_s) + \frac{1}{s(\omega)}\oint_S dS(\mathbf{x}) n_k(\mathbf{x})\sigma(\mathbf{x})\Bigg[P_P(\mathbf{x},\omega;\mathbf{x}_r)\frac{\partial P_0(\mathbf{x},\omega;\mathbf{x}_s)}{\partial x_k} \\ & - P_0(\mathbf{x},\omega;\mathbf{x}_s)\frac{\partial P_P(\mathbf{x},\omega;\mathbf{x}_r)}{\partial x_k}\Bigg]\,, \end{aligned} \tag{5.3}$$

where $s(\omega)$ is the time-Fourier transform of the source signature at point $\mathbf{x}_s$ and $\sigma(\mathbf{x})$ is the specific volume. We assume that the actual medium is enclosed by the surface $S = S_0 + S_R$, with an outward-pointing normal vector $\boldsymbol{n}$, as depicted in Figure 31, where S_0 is the air-water surface and S_R represents a hemisphere of radius R. The surface integral over S is generally known as the Kirchhoff surface integral. If we let radius R go to infinity, surface $S_{R\to\infty}$ gives a zero contribution to the Kirchhoff surface integral in (5.3) via the Sommerfeld's radiation boundary condition (Sommerfeld, 1954); see Appendix C for a numerical verification of this condition). Both P_0 and P_P must satisfy the Sommerfeld's radiation boundary condition at infinity in order that the Kirchhoff surface integral over $S_{R\to\infty}$ be zero. Furthermore, using the fact that the pressure field P_0 vanishes at the free surface (i.e., at the sea surface), equation

(5.3) reduces to

$$P_0(\mathbf{x}_r,\omega;\mathbf{x}_s) = P_P(\mathbf{x}_r,\omega;\mathbf{x}_s) + \frac{\sigma_0}{s(\omega)}\int_{S_0} dS(\mathbf{x})\, n_k(\mathbf{x}) \left[P_P(\mathbf{x},\omega;\mathbf{x}_r)\frac{\partial P_0(\mathbf{x},\omega;\mathbf{x}_s)}{\partial x_k}\right] \quad (5.4)$$

where σ_0 is the specific volume of the water. Using the facts that (i) on S_0, the outward-pointing normal vector $\boldsymbol{n}$ is along the negative z-axis, (ii) the vertical component of the particle velocity is related to the normal gradient of the pressure field via the force-equilibrium equation; i.e.,

$$i\omega v_3(\mathbf{x},\omega;\mathbf{x}_s) = \sigma_0 \frac{\partial P_0(\mathbf{x},\omega;\mathbf{x}_s)}{\partial x_3} \ , \quad (5.5)$$

and (iii) the reciprocity theorem shows $P_P(\mathbf{x},\omega;\mathbf{x}_r) = P_P(\mathbf{x}_r,\omega;\mathbf{x})$, then equation (5.4) can be rewritten as follows:

$$P_0(\mathbf{x}_r,\omega;\mathbf{x}_s) = P_P(\mathbf{x}_r,\omega;\mathbf{x}_s) + a(\omega)\int_{S_0} dS(\mathbf{x}) P_P(\mathbf{x}_r,\omega;\mathbf{x}) v_3(\mathbf{x},\omega;\mathbf{x}_s) \ , \quad (5.6)$$

with

$$a(\omega) = -\frac{i\omega}{s(\omega)} \ . \quad (5.7)$$

Equation (5.6) is the integral relationship between the data without free-surface multiples $P_P(\mathbf{x}_r,\omega,\mathbf{x}_s)$ and the recorded data $P_0(\mathbf{x}_r,\omega,\mathbf{x}_s)$. The first term on the right-hand side contains only primaries and internal multiples, and the second term contains free-surface-reflection events. Figure 32 illustrates with scattering diagrams how the second term on the right-hand side of (5.6) predicts free-surface multiples. Basically, the multidimensional convolution of the three events of v_3 (α_i) with the two events of P_P, through equation (5.6) allows us to predict free-surface events γ_{ij} ($\gamma_{ij} = \alpha_i * \beta_j$). This multidimensional convolution is entirely based on real events, and it produces only real events.

As the notion of time-retarded and time-advanced fields is central to this paper, let us show more explicitly the direction of time described in Figure 32 by considering

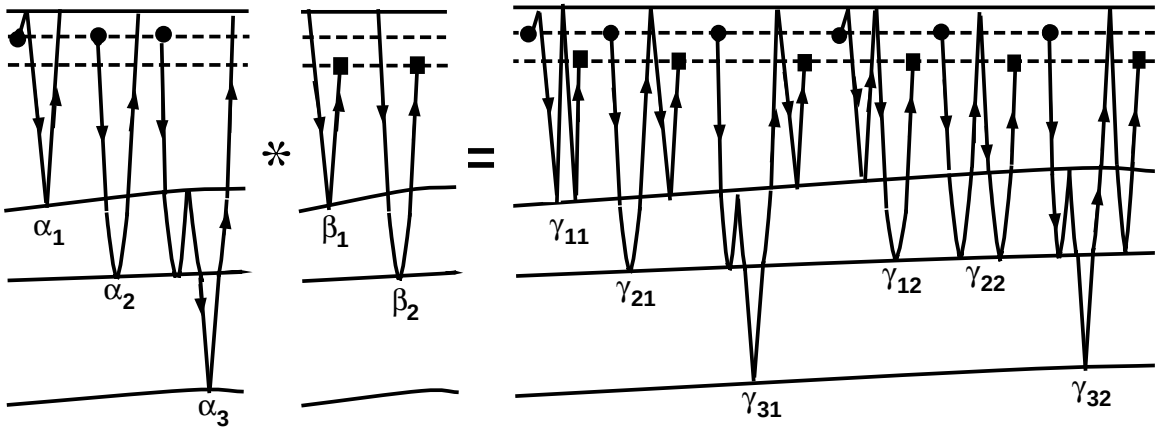

Fig. 32. Examples of the construction of free-surface reflections. Examples of the construction of free-surface reflections as a combination of events of the pressure data which contain only primaries (β_i) and the events of the vertical component of particle velocity (α_j). The symbol * denotes the multidimensional convolution operation in the second term of equation (5.6), which allows us to combine P_P and v_3. The results of the multidimensional convolutions of P_P and v_3 are denoted γ_{ij} such that $\gamma_{ij} = \alpha_i * \beta_j$. The same nomenclature is used in Figures 33, 34, 35, 36, 37, and 47(a).

the scattering diagrams in Figure 32 for a 1D medium and limiting ourselves to zero-offset data. To keep things simple, we ignore the effects of ghosts and geometrical spreading and assume that the source signature is a spike of amplitude unity. The vertical component of the particle velocity, v_3, can be written as follows:

$$v_3 = \alpha_1 Z_1 + \alpha_2 Z_2 + \alpha_3 Z_3 \ . \tag{5.8}$$

The pressure, P_P, can be written as follows:

$$P_P = \beta_1 Z_1 + \beta_2 Z_2 \ , \tag{5.9}$$

where

$$Z_k = \exp\left\{-i\omega\tau_k^{(z)}\right\} \tag{5.10}$$

and k take the values 1, 2, and 3. If τ_1, τ_2, and τ_3 denote the one-way traveltimes in the first layer, second layer, and third layer, respectively, then $\tau_1^{(z)} = 2\tau_1$, $\tau_2^{(z)} = 2\tau_1 + 2\tau_2$, and $\tau_3^{(z)} = 2\tau_1 + 4\tau_2 + 2\tau_3$. Note that Z_k is the temporal Fourier transform of

$\delta\left[t-\tau_k^{(z)}\right]$. The convolution of v_3 and P_P, which we have denoted γ_{kl}, is given by

$$\gamma_{kl}(\omega)=\alpha_k\beta_l\exp\left\{-i\omega\left[\tau_k^{(z)}+\tau_l^{(z)}\right]\right\}\ , \tag{5.11}$$

and its complex conjugate is

$$\gamma_{kl}^*(\omega)=\alpha_k\beta_l\exp\left\{i\omega\left[\tau_k^{(z)}+\tau_l^{(z)}\right]\right\}\ . \tag{5.12}$$

In equation (5.11) and (5.12), k takes the values 1, 2, and 3, whereas l takes the values 1 and 2. In the time domain, these fields are

$$\gamma_{kl}(t)=\alpha_k\beta_l\delta\left[t-\tau_k^{(z)}-\tau_l^{(z)}\right]=\alpha_k\beta_l\delta\left[t-t_{kl}^{(0)}\right]\ , \tag{5.13}$$

$$\gamma'_{kl}(t)=\alpha_k\beta_l\delta\left[t+\tau_k^{(z)}+\tau_l^{(z)}\right]=\alpha_k\beta_l\delta\left[t+t_{kl}^{(0)}\right]\ , \tag{5.14}$$

where

$$t_{kl}^{(0)}=\tau_k^{(z)}+\tau_l^{(z)}\geq 0\ . \tag{5.15}$$

$\gamma_{kl}(t)$ and $\gamma'_{kl}(t)$ are the temporal Fourier transforms of $\gamma_{kl}(\omega)$ and $\gamma_{kl}^*(\omega)$, respectively. From (5.13), it follows that $\gamma_{kl}(t)$ is a time-retarded field, whereas $\gamma'_{kl}(t)$ is a time-advanced field. Therefore the multidimensional convolution of v_3 with P_P, described by $\gamma_{kl}(t)$, creates only forward-propagating events, which is consistent with the scattering diagrams in Figure 32. Moreover, the traveltime $t_{kl}^{(0)}$ of each event γ_{kl} contains a two-way traveltime in the first layer (i.e., $2\tau_1$) or a multiple of $2\tau_1$. The traveltime of events which travel trough the second layer (i.e., γ_{12}, γ_{21}, γ_{22}, γ_{31}, and γ_{32}) contains a two-way traveltime in the second layer (i.e., $2\tau_2$) or a multiple of $2\tau_2$. The traveltime of events which travel through the third layer (i.e., γ_{31} and γ_{32}) contains a two-way traveltime in the third layer (i.e., $2\tau_3$). The importance of these remarks will become clear in the next section when the diagrammatica of the convolution-type rep-

resentatation theorem are contrasted with those of the correlation-type representation theorem.

Let us return to the problem of solving for P_P [see equqtion (5.6)]. First, note that the source point of the pressure field P_P and the receiver points of the particle velocity v_3 are located at the sea surface inside the Kirchhoff surface integral instead of at the actual locations of the seismic experiment. Therefore we must extrapolate the particle velocity from the actual receiver point, (x, y, z_r), to the point at the free surface, $(x, y, z_r = 0)$, and extrapolate the pressure field inside the integral from the source point at the free surface, $(x, y, z_s = 0)$, to the actual source point, (x, y, z_s), before solving the integral equation in (5.6). See (Ikelle et al., 2003) and (Ikelle and Amundson, 2005) for more details. Because the sources and receivers in towed-streamer experiments are very near the sea surface, these extrapolations amount simply to a modification of $a(\omega)$.

Our objective is to reconstruct P_P by solving equation (5.6). Let us start by rewriting (5.6) in this form:

$$\int_{S_0} dS(\mathbf{x}) \left\{ I(\mathbf{x}, \omega; \mathbf{x}_s) + B_{\text{kir}}(\mathbf{x}, \omega; \mathbf{x}_s) \right\} P_P(\mathbf{x}_r, \omega; \mathbf{x}) = P_0(\mathbf{x}_r, \omega; \mathbf{x}_s) \ , \qquad (5.16)$$

where

$$B_{\text{kir}}(\mathbf{x}, \omega; \mathbf{x}_s) = a(\omega) v_3(\mathbf{x}, \omega; \mathbf{x}_s) \qquad (5.17)$$

and

$$I(\mathbf{x}, \omega; \mathbf{x}_s) = \delta(\mathbf{x} - \mathbf{x}_s) \ . \qquad (5.18)$$

In compact notation, (5.16) becomes

$$P_P = \left[\mathcal{I} + \mathcal{B}_{\text{kir}} \right]^{-1} P_0 \ . \qquad (5.19)$$

Function $B_{\text{kir}}(\mathbf{x}_s, \mathbf{x}, \omega)$ is the kernel of operator $\mathcal{B}_{\text{kir}}$, and $I(\mathbf{x}_s, \mathbf{x}, \omega)$ is the kernel

of operator $\mathcal{I}$. Because the reflection coefficients are small in the subsurface, we generally need only to remove the first two or three orders of multiples from the data to achieve the objective of properly revealing primaries and internal multiples which may have been obscured by free-surface multiples. Actual practice has shown that the Taylor series expansion of (5.19) is far more numerically stable than (5.19) itself. The Taylor series expansion of (5.19), also known as the inverse Kirchhoff scattering series, can be written as

$$P_P = \left[\mathcal{I} - \mathcal{B}_{\text{kir}} + \mathcal{B}_{\text{kir}}^2 - \mathcal{B}_{\text{kir}}^3 + ...\right] P_0 \ . \tag{5.20}$$

The first term of this series is the actual data, the second term removes events that reflect once at the sea surface, the third removes events that reflect twice at the sea surface, and so on [see Ikelle and Amundsen (2005) for more details].

One of the key components of the derivation for constructing data without free-surface-reflection events is the notion of a model of the subsurface with an infinite water layer (Figure 31b). The data corresponding to this model do not contain free-surface-reflection events. Unfortunately, this notion does not readily extend to the construction of data without internal multiples. In other words, it is not yet possible to propose a model (other than a homogeneous medium) which does not produce internal multiples.

VIRTUAL EVENTS REVEALED BY THE CORRELATION-TYPE REPRESENTATION

Virtual events

As the idea of creating a model of the subsurface that we can associate with data without internal multiples does not seem realistic, we opted for a different approach in the construction of internal multiples. Our starting point in this new approach is the representation theorem, which utilizes both the time-advanced and time-retarded

fields instead of the time-retarded fields only, as we describe in (1). (de Hoop, 1966), (de Hoop, 1995), (Gangi, 1970), and (Bojarski, 1983) show that the representation theorem can also be written as follows:

$$s^*(\omega)P_0(\mathbf{x}_r,\omega;\mathbf{x}_s)+s(\omega)P_P^*(\mathbf{x}_r,\omega;\mathbf{x}_s)=\oint_S dS(\mathbf{x})n_k(\mathbf{x})\sigma(\mathbf{x})\Bigg[P_P^*(\mathbf{x},\omega;\mathbf{x}_r)\frac{\partial P_0(\mathbf{x},\omega;\mathbf{x}_s)}{\partial x_k} + P_0(\mathbf{x},\omega;\mathbf{x}_s)\frac{\partial P_P^*(\mathbf{x},\omega;\mathbf{x}_r)}{\partial x_k}\Bigg]\ , \qquad (5.21)$$

where the asterisk * denotes a complex conjugate. We assume that the medium is lossless. The actual data P_0 and the data without free-surface-reflection events P_P are, by definition, time-retarded fields because they are recordings of waves traveling in positive time in accordance with classical wave-propagation experiments. However, the complex conjugate of, say, P_P (i.e., P_P^*) is a time-advanced field because it describes recordings of waves traveling in negative time. (Note that whereas the time-advanced field, P_P^*, has no counterpart in nature, it is a valid solution to the wave equation.) Again, $s(\omega)$ is the Fourier transform of the source signature, and $s^*(\omega)$ is its complex conjugate. We can also notice, contrary to equation (5.3), in which the Kirchhoff scattering integral represents a time convolution between P_P and P_0 (i.e., the product of their Fourier transform), the Kirchhoff scattering integral in (5.21) represents a time crosscorrelation between P_P and P_0.

Before discussing (5.21) further, let us clarify our objective. In analyzing the representation theorem (5.21), our goal is not to recover the data without free-surface-reflection events [which is best achieved by using (5.3) anyway], but rather to extract some internal aspects of this equation, which can be used in the construction of internal multiples and primaries with scattering points at the free surface. Although equations (5.3) and (5.21) are equivalent, their scattering diagrams are quite different, as we will see later.

Let us now return to the analysis of equation (5.21). To further analyze this

equation, especially its Kirchhoff surface integral, let us rewrite (5.21) as follows:

$$s^*(\omega)P_0(\mathbf{x}_r,\omega;\mathbf{x}_s) \quad + \quad s(\omega)P_P^*(\mathbf{x}_r,\omega;\mathbf{x}_s) = -\sigma_0 \int_{S_0} dS(\mathbf{x}) \left[P_P^*(\mathbf{x},\omega;\mathbf{x}_r) \frac{\partial P_0(\mathbf{x},\omega;\mathbf{x}_s)}{\partial x_3} \right]$$

$$+ \quad 2\int_{S_R} dS(\mathbf{x}) n_k(\mathbf{x})\sigma(\mathbf{x}) \left[P_P^*(\mathbf{x},\omega;\mathbf{x}_r) \frac{\partial P_0(\mathbf{x},\omega;\mathbf{x}_s)}{\partial x_k} \right] \quad , \qquad (5.22)$$

or

$$\frac{1}{a^*(\omega)} P_0(\mathbf{x}_r,\omega;\mathbf{x}_s) \quad - \quad \frac{1}{a(\omega)} P_P^*(\mathbf{x}_r,\omega;\mathbf{x}_s) = -\int_{S_0} dS(\mathbf{x}) \left[P_P^*(\mathbf{x},\omega;\mathbf{x}_r) v_3(\mathbf{x},\omega;\mathbf{x}_s) \right]$$

$$+ \quad 2\int_{S_R} dS(\mathbf{x}) n_k(\mathbf{x})\sigma(\mathbf{x}) \left[P_P^*(\mathbf{x},\omega;\mathbf{x}_r) v_k(\mathbf{x},\omega;\mathbf{x}_s) \right] \quad , \qquad (5.23)$$

with

$$i\omega v_k(\mathbf{x},\omega;\mathbf{x}_s) = \sigma(\mathbf{x}) \frac{\partial P_0(\mathbf{x},\omega;\mathbf{x}_s)}{\partial x_k} \ . \qquad (5.24)$$

$a(\omega)$, invoked in (5.23), is defined in (5.7). Note that when passing from (5.21) to (5.22), we use the fact that the pressure field associated with the actual medium vanishes at the free surface and that on S_0, the outward-pointing normal vector, $\boldsymbol{n}$, is along the negative z-axis. Note also that the derivations we made earlier for passing from (5.3) to (5.4) are not applicable when passing from (5.21) to (5.22) because the contribution of the Kirchhoff surface integral over $S_{R\to\infty}$ in (5.21) no longer goes to zero if we let radius R go to infinity [see Appendix C for numerical illustrations]. In other words, P_P^* does not satisfy the Sommerfeld's radiation boundary condition at infinity. However, we have simplified the expression inside the integral over S_R because as $R \to \infty$, P_P and P_0 contain only downgoing waves (see Appendix C for more details).

Let us now examine the scattering events created during the computation of the Kirchhoff scattering integrals over S_0 and S_R for equation (5.23). We start with the integral over S_0. Figure 33 shows that the crosscorrelation of the direct wave contained

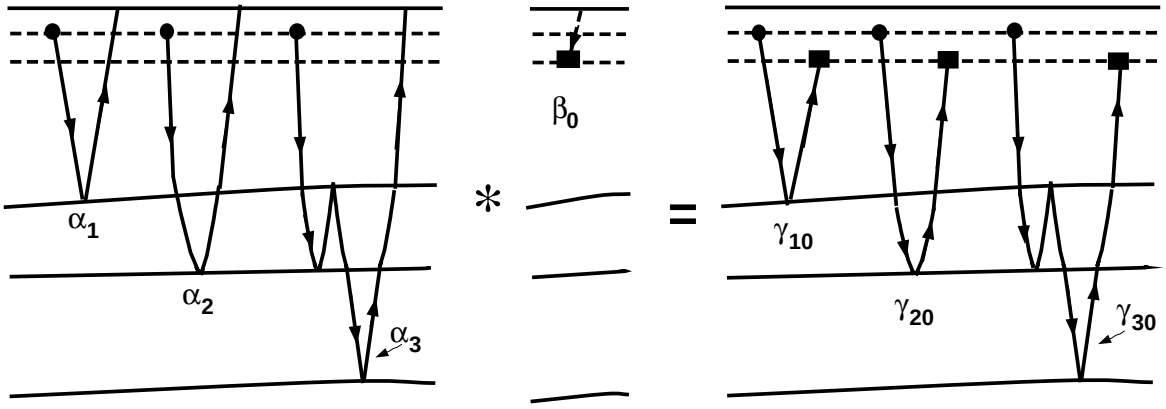

Fig. 33. Examples of the construction of internal multiples and primaries as a combination of pressure data containing only the direct wave (β_0) and the gradient of pressure (α_i). The scattering points connecting the two fields are located at the free surface. The nomenclature of seismic events described in Figure 32 is followed in all three parts of this figure.

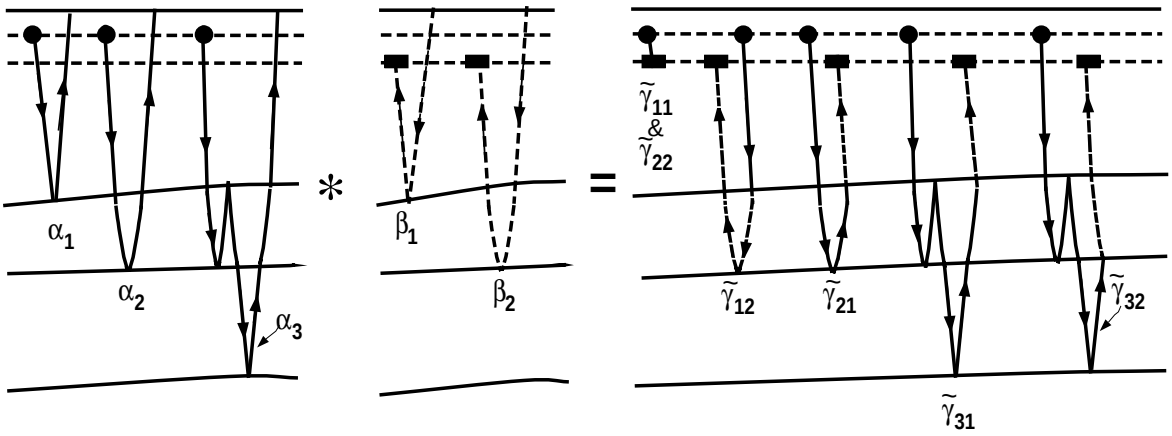

Fig. 34. Examples of the construction of virtual-reflection events as a combination of pressure data (β_j) containing primaries (no direct wave) and the gradient of pressure (α_i). Again, the scattering points connecting the two fields are located at the free surface. Note that we have used dotted lines to indicate the legs of scattering diagrams corresponding to the advanced waves which propagate backward in time. We will use this convention throughout the paper.

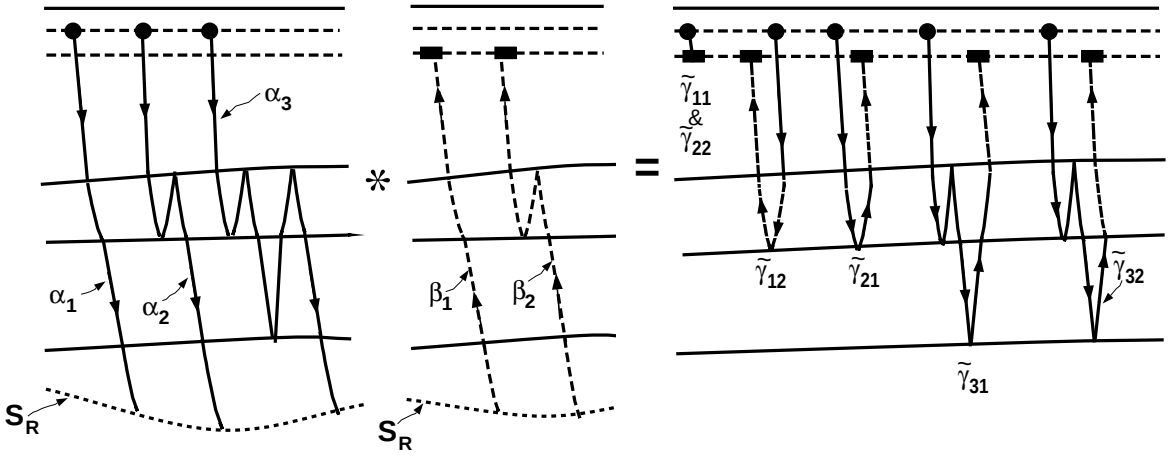

Fig. 35. Examples of the construction of virtual-reflection events as a combination of pressure data and the gradient of pressure. The scattering points connecting the two fields are now located on the surface S_R, defined in Figure 31.

in P_P (i.e., β_0) with v_3 (i.e., α_1, α_2, and α_3) allows us to create many events contained in P_0, including primaries and internal multiples. However, as we can see in Figure 34, where we crosscorrelate primaries contained in P_P (i.e., β_1 and β_2) with v_3 (i.e., α_1, α_2, and α_3), virtual events (i.e., $\tilde{\gamma}_{21}$, $\tilde{\gamma}_{31}$, and $\tilde{\gamma}_{32}$) and anticausal virtual events (i.e., $\tilde{\gamma}_{12}$) are also created during the integration over S_0. Again, note that wave-propagation paths of virtual events include bending in the opposite direction of the normal wave-propagation path, and they propagate backward in time. Our next task is to analyze how virtual events differ from real events. We will look at the traveltime and direction of propagation versus those of real events. Later in this section, we will contrast their seismograms with those of real events.

To explicitly analyze the traveltimes of virtual events versus those of real events, let us return to the 1D example discussed in the previous section [equations (5.8) through (5.15)]. Now we are interested in the crosscorrelation of v_3 and P_P (i.e., $v_3 P_P^*$) instead of their convolution. This crosscorrelation, which we will denote $\tilde{\gamma_{kl}}$, is given by

$$\tilde{\gamma}_{kl}(\omega) = \alpha_k \beta_l \exp\left\{-i\omega\left[\tau_k^{(z)} - \tau_l^{(z)}\right]\right\} \ . \tag{5.25}$$

In the time domain, these fields are

$$\tilde{\gamma}_{kl}(t) = \alpha_k \beta_l \delta \left[t - \tau_k^{(z)} + \tau_l^{(z)} \right] = \alpha_k \beta_l \delta \left[t - t_{kl}^{(0)} \right] \ , \tag{5.26}$$

where

$$t_{kl}^{(0)} = \tau_k^{(z)} - \tau_l^{(z)} \ . \tag{5.27}$$

$\tilde{\gamma}_{kl}(t)$ is the temporal Fourier transform of $\tilde{\gamma}_{kl}(\omega)$. Because $t_{kl}^{(0)}$ is no longer always positive as in (5.15), some events $\tilde{\gamma}_{kl}(t)$ are time-retarded and some are time-advanced. For example, the traveltime of $\tilde{\gamma}_{12}(t)$ is negative $[t_{12}^{(0)} = -2\tau_2]$; thus $\tilde{\gamma}_{12}(t)$ is an anticausal event. We still consider this anticausal event as a virtual event because its scattering diagram is a combination of solid and dotted lines, as depicted in Figure 34. Recall that τ_1, τ_2, and τ_3 are the one-way traveltimes in the first layer, second layer, and third layer, respectively. The traveltimes of $\tilde{\gamma}_{11}(t)$ and $\tilde{\gamma}_{22}(t)$ are zero $[t_{11}^{(0)} = t_{22}^{(0)} = 0]$; these two events describe the direct wave. The traveltimes of $\tilde{\gamma}_{21}$ and $\tilde{\gamma}_{31}$ are positive $[t_{21}^{(0)} = 2\tau_2$ and $t_{31}^{(0)} = 4\tau_2 + 2\tau_3]$, but they do not contain the two-way traveltime in the first layer—that is, the traveltime characteristic of virtual events whose negative bending (dotted lines in Figure 34) is limited to the first layer. In this case, virtual events are a result of the crosscorrelation of two primaries or a primary and an internal multiple in a 1D medium. Another virtual event is $\tilde{\gamma}_{32}$, but its negative bend (dotted line in Figure 34) now travels through the first and second layer. Yet its traveltime $[t_{32}^{(0)} = 2\tau_2 + 2\tau_3]$ includes the traveltimes through the second layer in addition to the traveltime through the third layer because the internal multiple, α_3, which is being crosscorrelated to the primary, β_2, bounces at the second layer, producing a traveltime of 4 τ_2 in this layer. Therefore, the crosscorrelation between a primary and this multiple cannot annul the traveltime of the resulting virtual events in the second layer; it can only reduce this traveltime to 2 τ_2. Notice that none of the events created by the crosscorrelation in (5.26) were

created by the convolution in (5.14). Furthermore, the only real events created by the crosscorrelation in this example are the direct waves. Actually, if v_3 contains only primaries, its multidimensional correlation with P_P will produce only direct waves, anticausal events, and virtual events; it does not create any primaries or internal multiples. On the other hand, the multidimensional convolution of v_3 (even if it contains both primaries and free-surface-reflection events) with P_P creates only free-surface-reflection events; this process does not create primaries or internal multiples.

As the new type of reflection events in Figure 34 is not part of the wave-scattering data, these events must be canceled out by some of the events created during the integration over S_R. By examining the scattering diagrams of the events created during the Kirchhoff scattering integral over S_R (see Figure 35), we can see that this integral also creates the same virtual and anticausal events as the Kirchhoff integral over S_0. So during the summation of the two terms on the right-hand side of (5.22), all the new reflection events, and all the anticausal events not present in P_0 or P_P^*, cancel out.

Let us also analyze the traveltimes of virtual and anticausal events described in Figure 35 with the 1D example introduced in the previous section [equations (5.8) through (5.15)]. The only difference between the previous discussion [equations (5.25) through (5.27)] associated with Figure 34 and the discussion associated with Figure 35 is that we have to modify the traveltime $\tau_k^{(z)}$ for Figure 35. By substituting in (5.26) the following new definitions of $\tau_k^{(z)}$,

$$\tau_1^{(z)} = \tau_1 + \tau_2 + \tau_3 + \tau_4$$

$$\tau_2^{(z)} = \tau_1 + 3\tau_2 + \tau_3 + \tau_4$$

$$\tau_3^{(z)} = \tau_1 + 5\tau_2 + 3\tau_3 + \tau_4 \ ,$$

where τ_4 denotes the traveltime through the fourth layer in Figure 35 up to the surface S_R, we obtain exactly the same events as in the Kirchhoff integral over S_0.

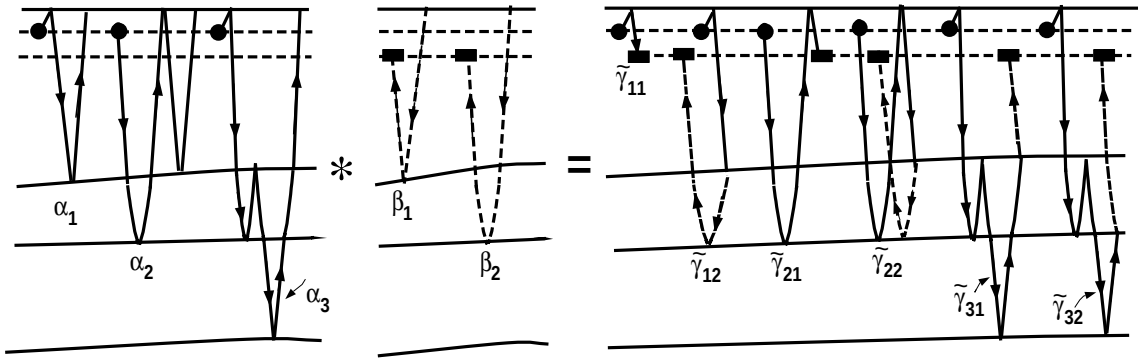

Fig. 36. Our construction of virtual events in Figures 33, 34, and 35 have not included the free-surface-reflection events. Here we illustrate what happens when we include them in the gradient of pressure. Examples of the construction of virtual-reflection events as a combination of pressure data (β_j) containing primaries, and the gradient of pressure (α_i) containing free-surface-reflection events (ghosts and free-surface multiples). Again the scattering points connecting the two fields are located at the free surface. Note that this combination produces new configurations of virtual events, sometimes strange-looking virtual events.

Our discussion in this section has not included the free-surface-reflection events so far. Figures 36 and 37 show what happens when we include them in the particle velocity field. In other words, our construction of events associated with the Kirchhoff scattering integral over S_0 and over S_R now includes the multidimensional correlation of free-surface-reflection events with primaries. As we can see in Figures 36 and 37, this correlation produces new configurations of virtual events, sometimes strange-looking virtual events. Nevertheless, these virtual events follow the same patterns as those in Figures 34 and 35. Basically, the first part of the wave-propagation path of these events follows the normal forward propagation, and the second part follows a backward propagation path, or vice versa. At this point, we cannot anticipate the practical usefulness of the new scattering diagrams in Figures 36 and 37. However, we believe that when one creates a scattering diagram based on sound physics, some useful purpose for such diagrams will be found in the long run. That is why we took

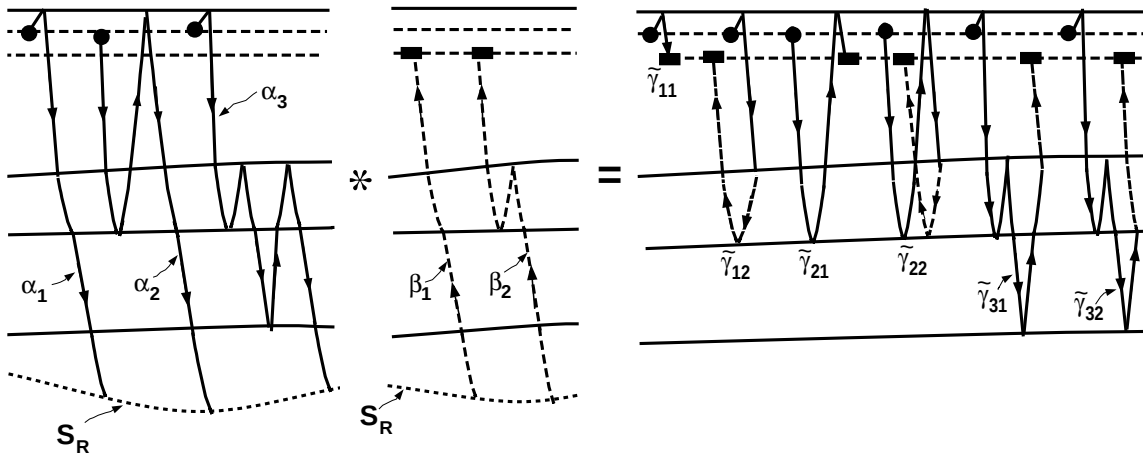

Fig. 37. Examples of the construction of virtual-reflection events as a combination of pressure data, and the gradient of pressure containing free-surface-reflection events. The scattering points connecting the two fields are now located on the surface S_R. This combination also produces the same strange-looking virtual events as in Figure 36.

the liberty of including them here.

Note also that in all the scattering diagrams of virtual events that we have presented so far, the negative bend is located on the receiver side. We will call such events "receiver-side" virtual events. By interchanging source and receiver locations in (5.21)-(5.23) and in Figures 33, 34, 35, 36 and 37, the negative bend (dotted line) of virtual events will move to the source side. We will call such events "source-side" virtual events. Figure 38 shows receiver-side and source-side virtual events. The multidimensional convolution of these two events produces another strange-looking event whose usefulness is yet to be established.

Snapshots of wave propagation of a virtual event

To aid in the understanding of the direction of wave propagation of the last leg (the negative bending leg) of the wave path of virtual events, we have simulated the wave propagation of this leg. Actually, our simulation includes both a virtual event and a real event to facilitate comparison. These events being simulated are depicted in Figure 39, along with the model used to generate the data. The model consists

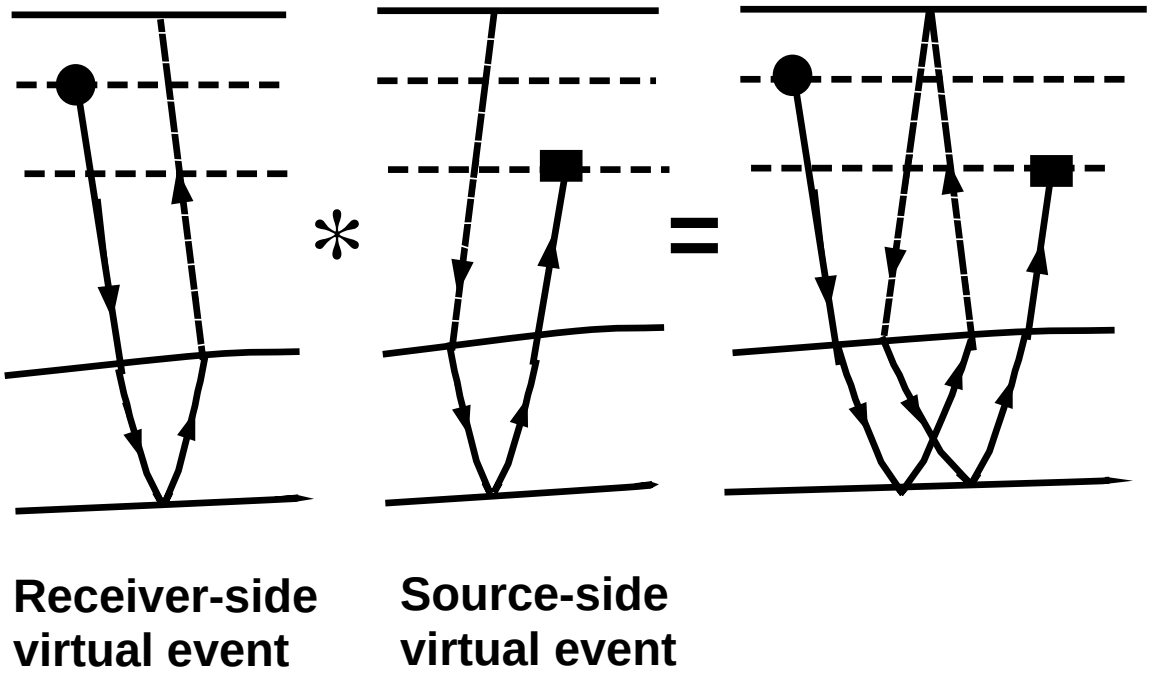

Fig. 38. An example of an event constructed as a combination of receiver-side and source-side virtual events. This is an another strange-looking event whose usefulness is yet to be established.

of a homogeneous dipping layer sandwiched between two homogeneous half-spaces (HS1/DL2/HS3).

We generated our snapshots based on Kirchhoff scattering integral over S_0 in (5.22). We computed P_P with finite-difference modeling for a model consisting of two homogeneous half-spaces with a dipping interface (HS1/DL2). We basically converted the dipping layer in Figure 39 into a half-space for the computation of P_P. For the computation of v_3, we used the actual model in Figure 39, but we retained only the reflection from the interface between the dipping layer and the bottom half-space of the model in Figure 39 (i.e., interface DL2/HS3). In other words, v_3 contained only one event: the reflection at the interface DL2/HS3. We then computed the following quantity:

$$M(x,z,\omega) = \frac{1}{s^*(\omega)} \int_{S_0} dx' \left[P_P^*(x,z,\omega;x') v_3(x',\omega;x_s) \right] \ . \tag{5.28}$$

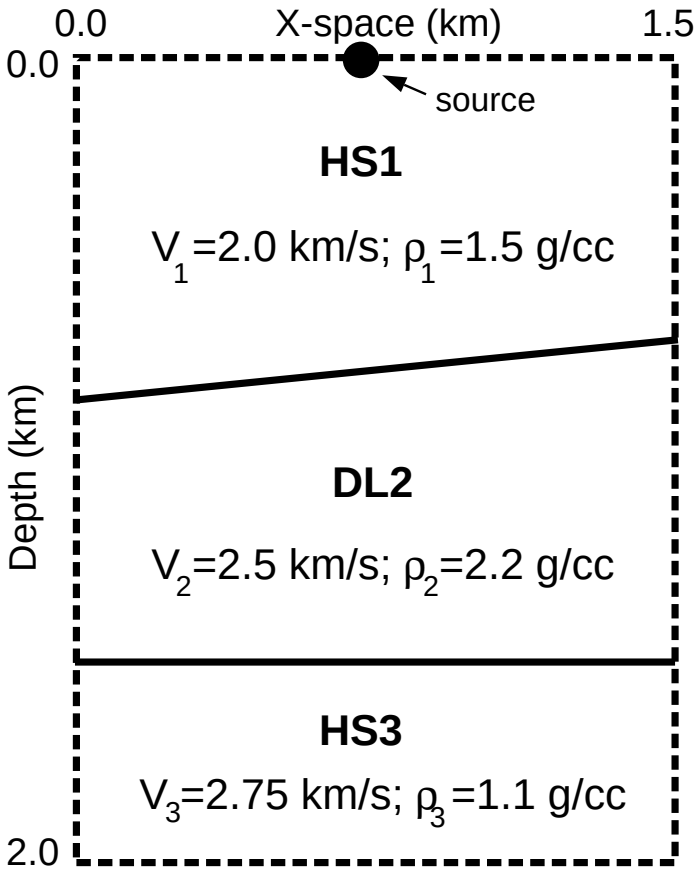

Fig. 39. The model used to simulate wave propagation. The dotted lines in our model are used to indicate nonreflecting boundaries. The model consists of two homogeneous half-spaces (HS1 and HS3) and one layer (DL2).

The snapshots in Figure 40 are the displays of $M(x, z, t)$, which is the temporal Fourier transform $M(x, z, \omega)$, for $x_s = 0.75$ km. We can effectively see that the virtual events propagate backward in time, in the opposite direction of the real event. Because the two events share the same paths until the upgoing wave hits the interface HS1/DL2, it is normal that the forward propagating event and backward propagating event arrive at the interface at the same time. The virtual event then ceases to propagate, whereas the real event continues its forward motion.

The snapshots in Figure 40 contained some smearing artifacts that we have indicated by A. These are caused by the multidimensional crosscorrelation invoked in (5.28) between the events contained in P_P and the event contained in v_3. The

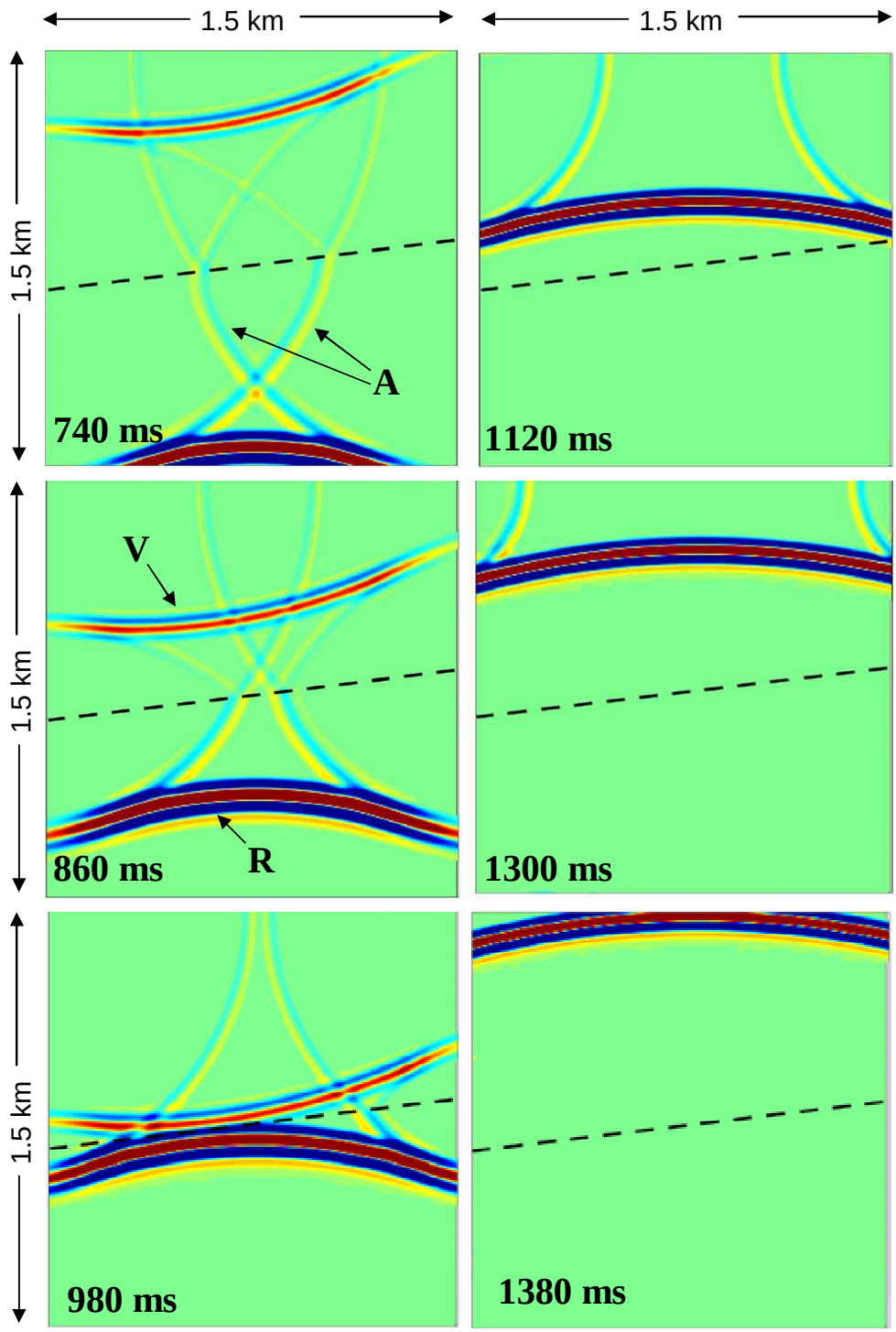

Fig. 40. Snapshots of virtual and real events. The source is located at $x_s = 0.75$ km. The event propagating backward in time in HS1 is the virtual event (snapshots 740 ms to 980 ms) and the events propagating forward in time in HS1 is the real seismic event. Notice also the correlation artifacts that are responsible for the notion of renormalization introduced in this paper (V = virtual event, R = real event, A = correlation artifacts).

reason why (5.28) produces the artifacts in Figure 40 can be traced to the fact that the crosscorrelation basically detects the similarity between the events contained in P_P and the event contained in v_3, including their relative time-delay variations with offsets. If there is a portion of data in which the variations of time delay with offsets between the two events are constant (i.e., in this portion of data, the crosscorrelation between the two events actually act as a shifted autocorrelation), we obtain the smearing artifacts (Figure 40) which acts as apparent "refracted wave", in addition to the normal wavefronts, which describe the portion of data in which the variation of time delays with offsets is not constant. The presence of these apparent refracted waves along with the virtual events is one of the reasons why it is difficult to design a model of the subsurface with positive stiffnesses and positive Poisson's ratios for which the classical modeling technique, like finite-difference methods, can produce snapshots of virtual event propagation such as those in Figure 40. Remember that positive stiffnesses imply that when a force deforms an elastic object, the resulting displacement will be in the same direction as the force. Negative stiffnesses imply a reversal of this directional relationship between force and displacement in deformed objects. The Positive Poisson's ratio implies that shrinking down materials in the cross-section when they are stretched. Negative Poisson's ratio implies the opposite; materials become fatter in the cross-section when they are stretched.

The snapshots in Figure 40 are now displayed in Figure 41 as a superposition of wavefronts to point out the difference in spatial direction between real and virtual events. Having superimposed the corresponding raypaths on these wavefronts, we can see that the virtual and real events, propagate not only in the opposite direction in time, but also in the opposite direction in space. In other words, for the virtual event, the wave entering the top half-space (HS1) from layer DL2 bends in the opposite direction of the usually observed direction, which is the direction of the real event. The direction of the virtual event is indicated by a dotted line, and that of the real

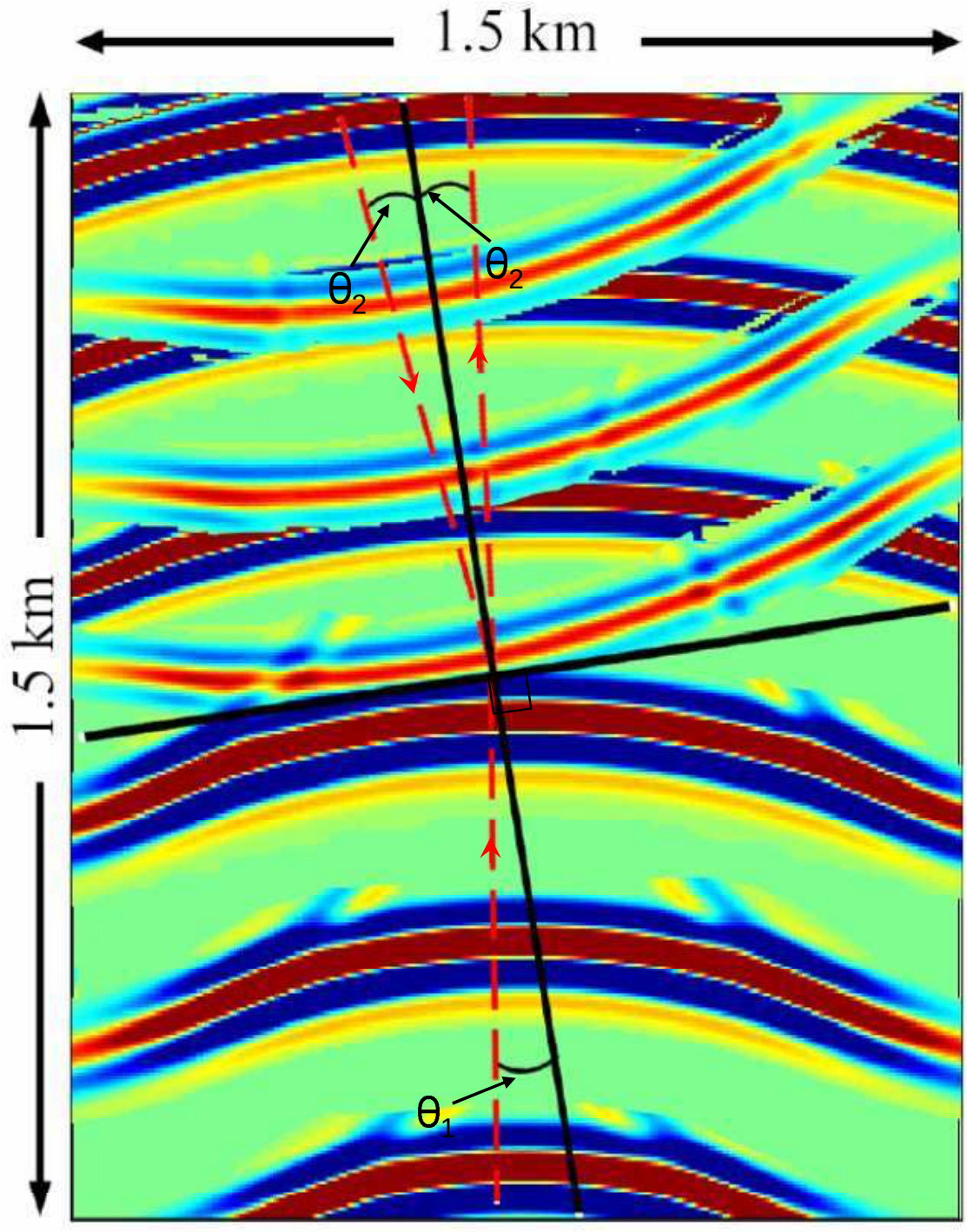

Fig. 41. The snapshots in Figure 40 are now displayed as a superposition of wavefronts. We have also superimposed the corresponding raypaths (red dotted lines) on these wavefronts. Notice the spatial direction between real and virtual events. In other words, the bend of the virtual event is opposite from that of the real event's direction.

event is indicated by a solid line. If θ_1 is the angle of the incident wave and θ_2 is the angle of the transmitted wave, as depicted in Figure 41 for the virtual event, they are related by Snell's law as follows:

$$\sin\theta_1 = \frac{V_2}{V_1}\sin\left(-\theta_2\right) \ . \tag{5.29}$$

For the real event they are related by Snell's law as follows:

$$\sin\theta_1 = \frac{V_2}{V_1}\sin\theta_2 \ , \tag{5.30}$$

where V_1 and V_2 are the velocities of half-space HS1 and of layer DL2, respectively.

Note that, for the sake of the clarity of Figure 41, the crosscorrelation-related artifacts that were pointed out in Figure 40 have been artificially attenuated before superposing the various snapshots to produce Figure 41.

Renormalization of virtual events

In physics, renormalization refers to a variety of theoretical concepts and computational techniques revolving either around the idea of rescaling transformation, or the process of removing infinities from calculated quantities. Renormalization is used here in the context of rescaling a transformation—more precisely, rescaling the cross-correlation operation in (5.28).

The first question is, why do we need to renormalize virtual events? The second question is how do we mathematically describe this renormalization? To answer the first question, we are first going to generate seismic data for the 2D model described in Figure 42 using a finite-difference scheme. The data consist of 241 sources and 241 stationary receivers corresponding to offsets between 0 m and 3000 m. Figure 43(a) describes a shot gather of the shot point at 2000 m and a zero offset section of the particle velocity v_3. Figure 43(b) represents the shot gather of the shot point at 2000 m and a zero-offset section of the pressure data, P_P. To facilitate our discussion,

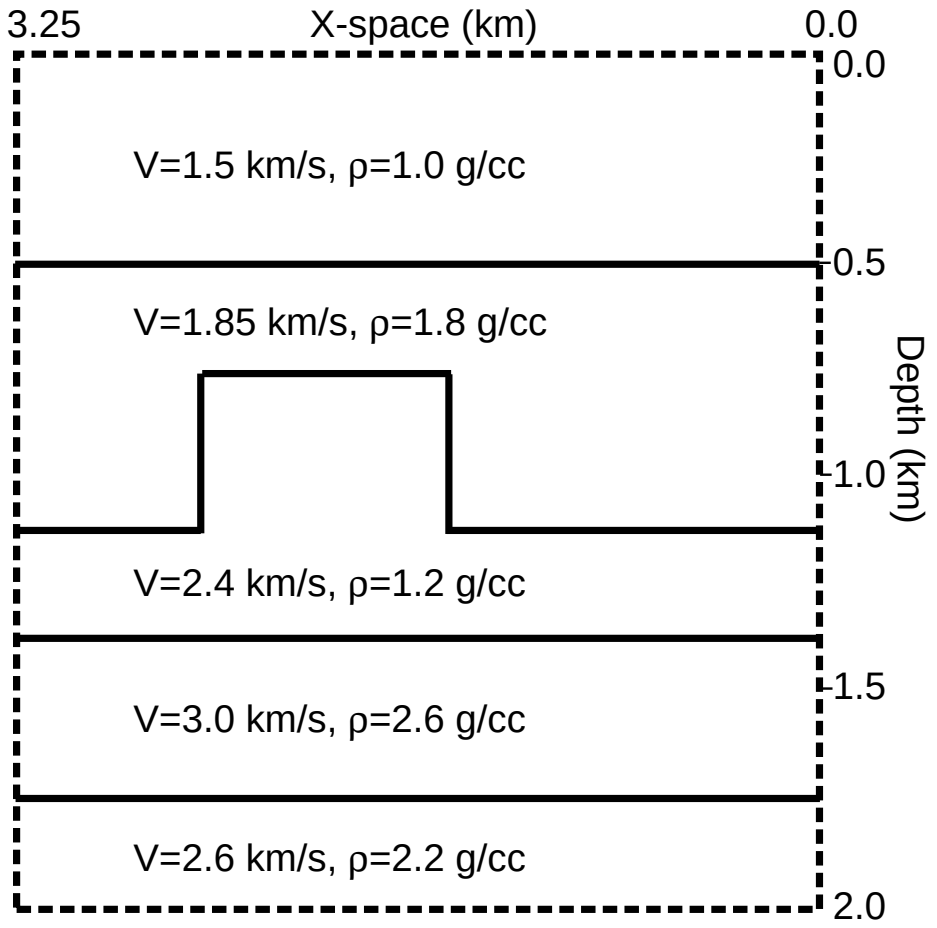

Fig. 42. The 2D model used to generate the data in Figures 43(a) and 43(b). Again, the dotted lines in this model are used to indicate nonreflecting boundaries.

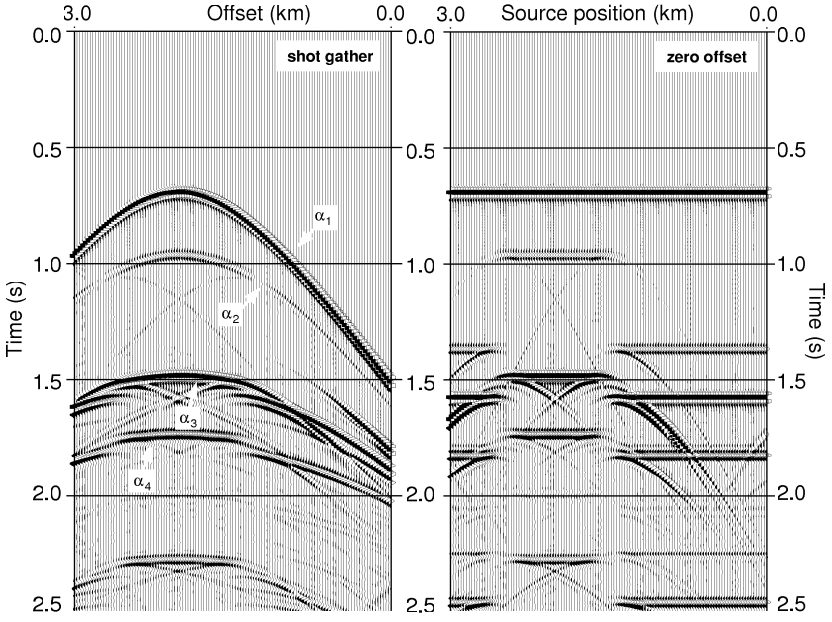

(a)

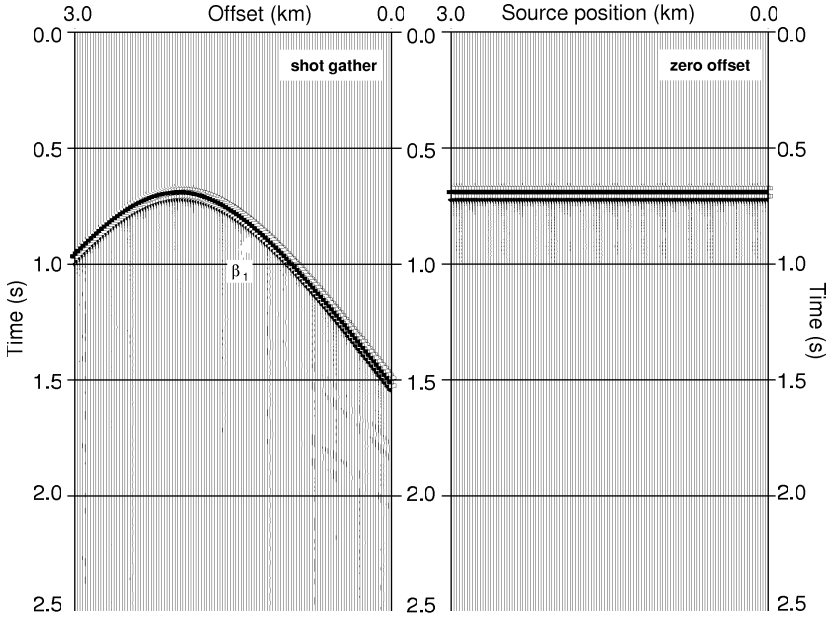

(b)

Fig. 43. Seismic data generated for the 2D model described in Figure 42 using a finite-difference scheme. The data consist of 241 sources and 241 stationary receivers corresponding to offsets between 0 m and 3000 m. (a) describes a shot gather of the shot point at 2000 m and a zero offset section of the particle velocity v_3. (b) shows the shot gather of the shot point at 2000 m and a zero-offset section of the pressure data, P_P. At this stage of the discussion of (5.31), we have limited ourselves to P_P containing one event.

we limited the pressure data to the sea-floor reflection only. In other words, the lone event β_1 of the field P_P (Figure 43(b) is identical to the event α_1 of v_3 in Figure 43(a). Again, we define the field of virtual events as follows:

$$P_A(\mathbf{x}_r, \omega; \mathbf{x}_s) \;=\; -a^*(\omega) \int_{S_0} dS(\mathbf{x}) \left[P_P^*(\mathbf{x}, \omega; \mathbf{x}_r) v_3(\mathbf{x}, \omega; \mathbf{x}_s) \right] \;, \qquad (5.31)$$

where P_A denotes the virtual data, P_P is the data in Figure 43(b), and v_3 are the data in Figure 43(a). Figure 44 shows a virtual shot gather for a shot at 2000 m and a virtual zero-offset section resulting from the computations in (5.31). We can first notice that the region of support of the virtual events (i.e., the region in which P_A has valid values—P_A being null or negligible outside the region of support) is smaller than that of the actual data. That is why the moveout of virtual events is almost horizontally flat for offsets greater than 2000 m. This reduction of the region of virtual events is due to the fact that the crosscorrelation invoked in (5.31) tends to compress data instead of expanding them as the convolution does. The results in Figure 44 also confirm that the autocorrelation of an event leads to an apparent direct wave (e.g., $\tilde{\gamma}_{11} = \alpha_1 * \beta_1$).

To point out why we need to renormalize the virtual data in Figure 43(a), let us try to use them to reconstruct data in Figure 43(a). As illustrated in Figure 29, the primaries and internal multiples can be constructed in two steps. The first step consists of generating the virtual events, as described in (5.31), and the second step is a convolution of virtual events with actual data, as follows,

$$P_0(\mathbf{x}_r, \omega; \mathbf{x}_s) \;=\; -a(\omega) \int_{S_0} dS(\mathbf{x}) \left[P_A(\mathbf{x}, \omega; \mathbf{x}_r) v_3(\mathbf{x}, \omega; \mathbf{x}_s) \right] \;, \qquad (5.32)$$

to obtain primaries and internal multiples. Figure 45 shows the results of the convolution of P_A with v_3 using (5.32). Despite some artifacts, we have now returned to a more familiar look at the data. By comparing the arrival times in Figure 45 to those in Figure 43(a), we can see that we have properly reconstructed the traveltimes of

all the events in Figure 43(a). However, the data in Figure 45 contain some artifacts not present in the actual data. Furthermore, the amplitudes are not properly reconstructed in the data in Figure 45, especially in large offsets. The renormalization is needed to address this problem.

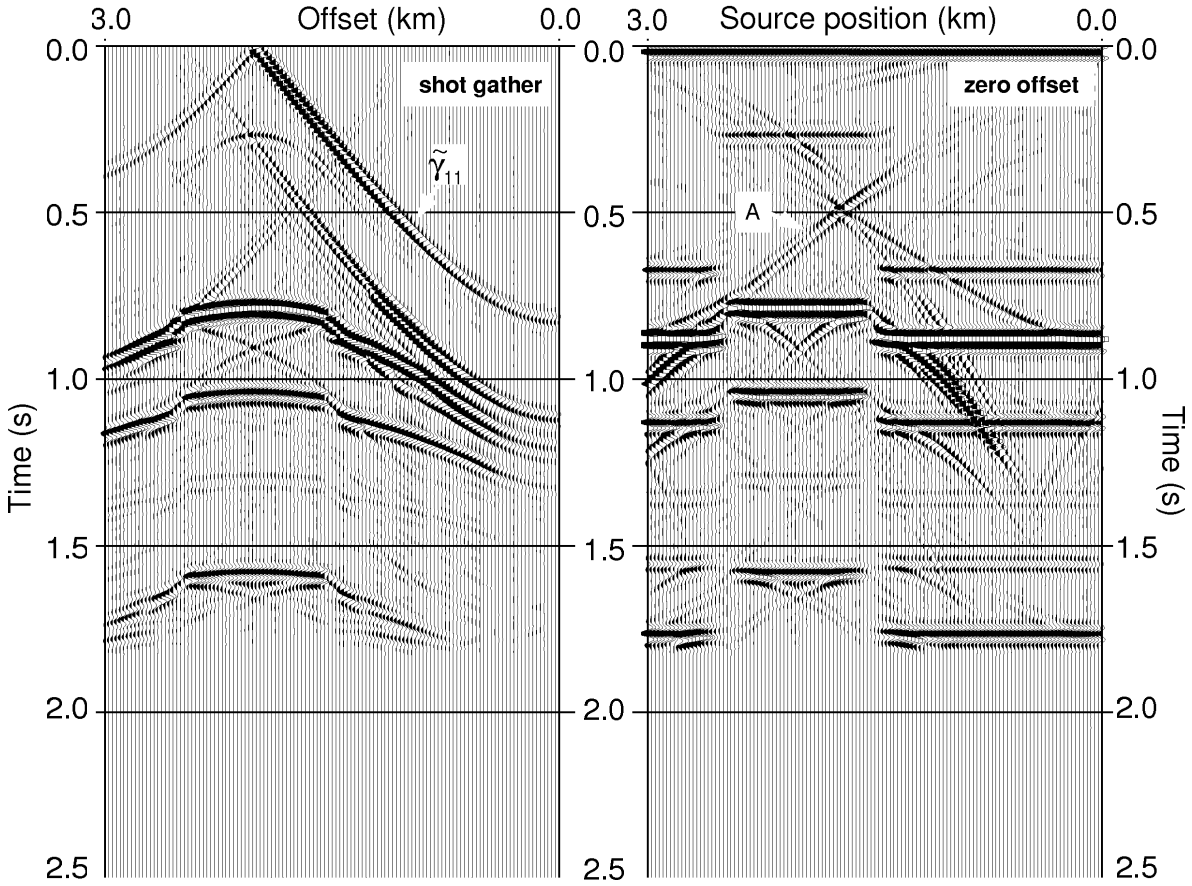

Fig. 44. The field of virtual events for a virtual shot gather with the shot at 2000 m and a virtual zero-offset section. It was generated using equation (5.31). We have indicated with the letter A some of the correlation artifacts in this plot.

So the results in Figure 45 show that the process of convolving the field of virtual events with the normal data fails to properly predict the amplitudes of primaries and internal multiples. This amplitude problem arises from the process of crosscorrelation in (5.31), followed by the convolution in (5.32). This process allows us to cancel out traveltimes of the backward-propagating legs of the virtual events with forward-propagating legs of the normal events to produce correct traveltimes of primaries and

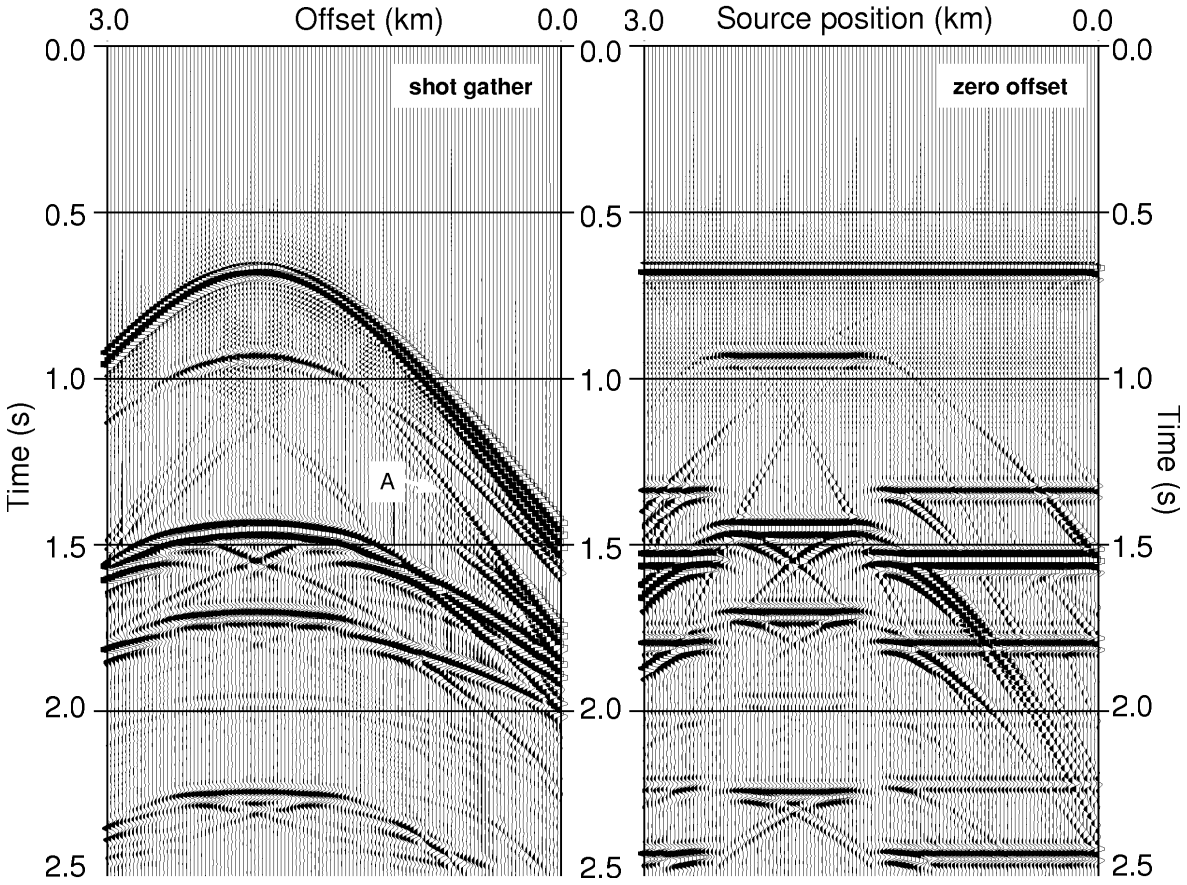

Fig. 45. The results of the convolution convolving the field of virtual events (Figure 44) with the normal data (Figure 43(a)).

internal multiples. However, it fails to produce the correct amplitude of these events. To ensure that the amplitudes of seismic events are also correctly predicted in this process, we have to renormalize either the crosscorrelation in (5.31) or the convolution in (5.32). For example, the renormalization of the crosscorrelation in (5.31) can be achieved by replacing P_P^* in the computation of virtual events with P_P^{-1}. The field P_P^{-1} is defined as follows:

$$\int_{S_0} dS(\mathbf{x})\, P_P^{-1}(\mathbf{x}_s, \omega, \mathbf{x})\, P_P(\mathbf{x}, \omega, \mathbf{x}_r) \;\; = \delta(\mathbf{x}_s - \mathbf{x}_r) \tag{5.33}$$

or its equivalent,

$$\int_{S_0} dS(\mathbf{x})\, A(\mathbf{x}_s, \omega, \mathbf{x}) P_P^{-1}(\mathbf{x}, \omega, \mathbf{x}_r) = \; P_P(\mathbf{x}_s, \omega, \mathbf{x}_r) \;, \tag{5.34}$$

where

$$A(\mathbf{x}_s, \omega, \mathbf{x}) = \int_{S_0} dS(\mathbf{x}')\, P_P^*(\mathbf{x}_s, \omega, \mathbf{x}')\, P_P(\mathbf{x}', \omega, \mathbf{x}) \;. \tag{5.35}$$

Thus, (5.31) becomes

$$P'_A(\mathbf{x}_r, \omega; \mathbf{x}_s) = \int_{S_0} dS(\mathbf{x}) P_P^{-1}(\mathbf{x}, \omega; \mathbf{x}_r) v_3(\mathbf{x}, \omega; \mathbf{x}_s) \;\; , \tag{5.36}$$

where P'_A denotes the field of normalized virtual events. Figure 46(a) shows the normalized virtual events. As expected, the traveltimes of virtual events in Figure 46(a) are unchanged compared to the traveltimes of the same events in Figure 44. The difference in amplitudes between the two figures is clearly visible. The usefulness of normalized virtual events is more evident in the data (in Figure 46(b)) produced by convolving P'_A and P_0, as described in (5.32). By comparing Figure 46(b) to Figure 45, we can see that all the artifacts indicated in Figure 45 are significantly reduced in Figure 46(b). Moreover, the amplitudes of primaries and internal multiples in Figure 46(b) have now been correctly reconstructed.

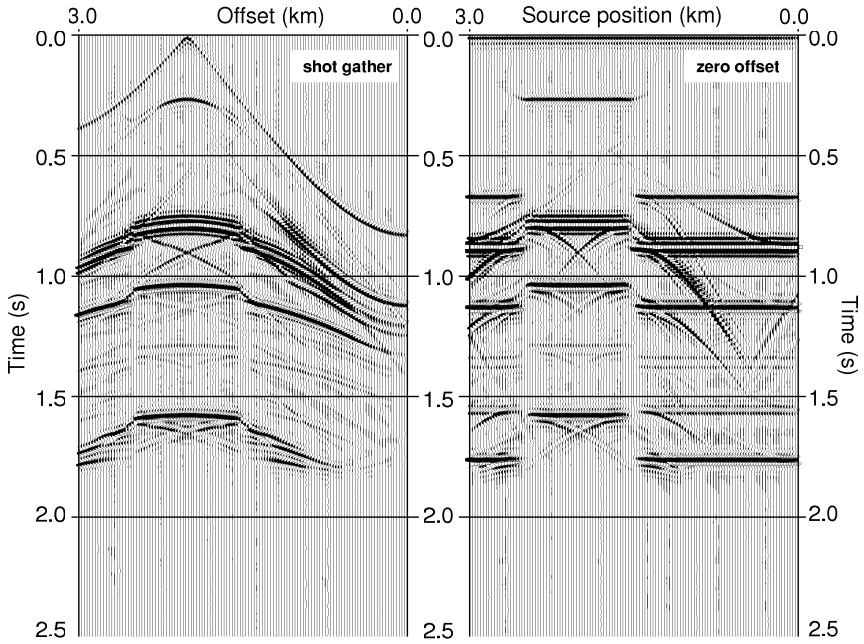

(a)

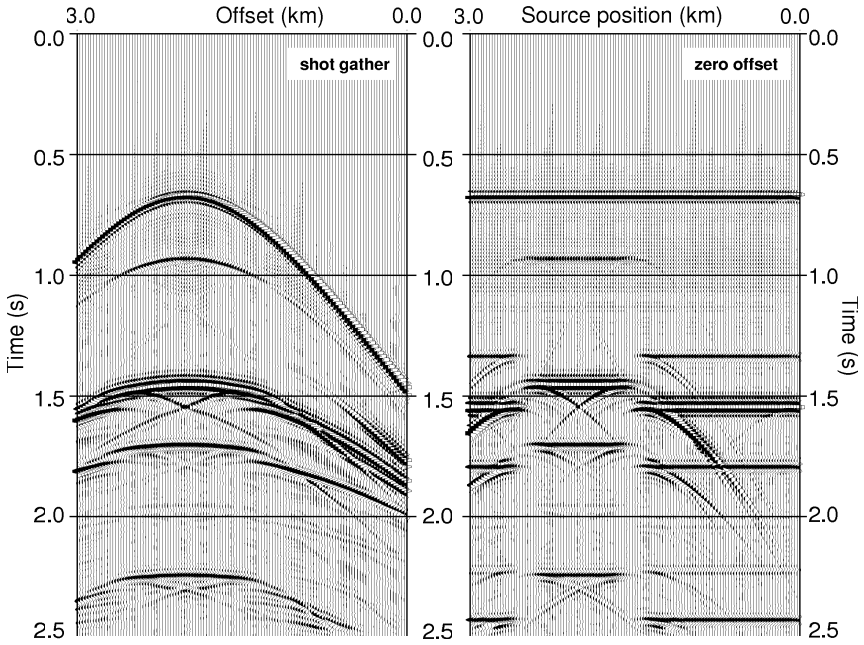

(b)

Fig. 46. The same as Figures 44 and 45 using the renormalized data i.e., equation (5.31) instead of (5.36) for the computation of virtual events. (a) The field of virtual events for a virtual shot gather with the shot at 2000 m and a virtual zero-offset section. (b) The results of the convolution convolving the field of virtual events with the normal data. Notice how significantly the correlation artifacts have been reduced.

The concept of virtual events in the attenuation of internal multiples

Notice that if α_1 is set to zero in Figure 43(a) (i.e., the sea-floor reflection event is muted from the data in Figure 43(a), the virtual data will not contain the apparent direct wave γ_{11}, and the data in Figure 46(b) will contain only internal multiples. Such a reconstruction of internal multiples is important for the purpose of attenuating internal multiples from the data. Let us first clarify this observation with scattering diagrams before illustrating it with data in Figure 43(a). As shown in Figure 47(a), the crosscorrelation of P_P (made of event β_1) with v_3 (made of events α'_1, α'_2, and α'_3) allows us to create only causal virtual events. Moreover, this correlation does not create the apparent direct wave. In fact, as long as the events in P_P arrive earlier than the events in v_3, without an overlap between the fields, the crosscorrelation of the two fields will not produce direct wave events. By convolving the field of virtual events in Figure 47(a) with v_3 (i.e., α'_1, α'_2), we obtained a field containing only internal multiples. Because P_P was limited to one event only, we obtained only internal multiples related to this event. In other words, if event β_1 corresponds to the sea-floor reflection, we only predicted sea-floor-related internal multiples. We will describe later how this process can be carried out iteratively to predict and attenuate all internal multiples included in seismic data.

To explicitly analyze the traveltimes of internal multiples predicted in Figure 47(b), let us use the 1D example discussed in the previous sections [equations (5.8) through (5.15); equations (5.25) through (5.27)]. The vertical component of the particle velocity, v_3, and the pressure, P_P, are now defined as follows:

$$v_3 = \alpha'_1 Y_1 + \alpha'_2 Y_2 + \alpha'_3 Y_3 \ , \tag{5.37}$$

$$P_P = \beta_1 Z_1 \ , \tag{5.38}$$

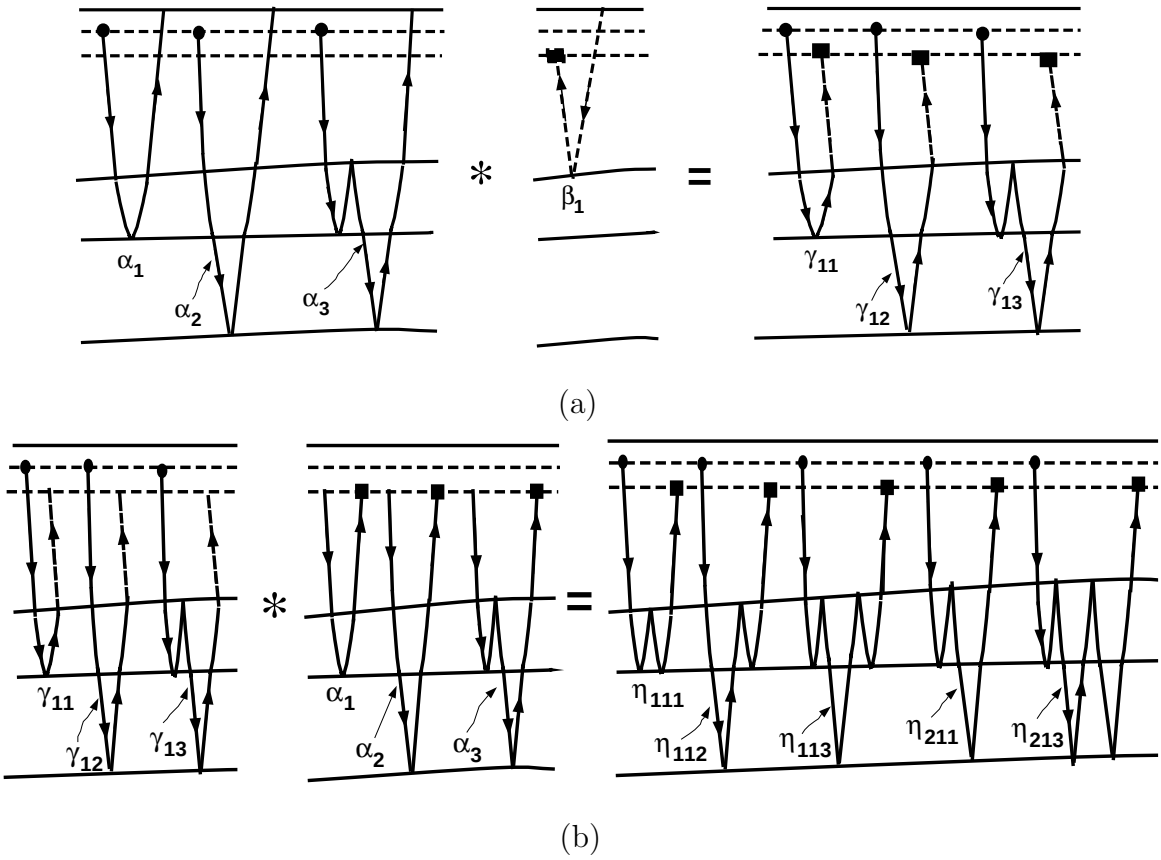

Fig. 47. An illustration with scattering diagrams of the two-step process for generating internal multiples. (a) The first step generates virtual events. (b) The second step generates internal multiples using the virtual events generated in the first step. Notice that the data in the first step are divided into parts which do not intersect. The earlier part contains only primaries, and the latter part contains primaries and internal multiples ($\gamma_{ij} = \alpha_i * \beta_j$ and $\eta_{ijk} = \alpha_i * \gamma_{jk}$).

where

$$Z_1 = \exp\left\{-i\omega\tau_1^{(z)}\right\} \ , \ Y_k = \exp\left\{-i\omega\tau_k^{(y)}\right\} \tag{5.39}$$

and k takes the values 1, 2, and 3. If τ_1, τ_2, and τ_3 denote the one-way traveltimes in the first layer, second layer, and third layer, respectively, then $\tau_1^{(z)} = 2\tau_1$, $\tau_1^{(y)} = 2\tau_1 + 2\tau_2$, $\tau_2^{(y)} = 2\tau_1 + 2\tau_2 + 2\tau_3$, and $\tau_3^{(y)} = 2\tau_1 + 4\tau_2 + 2\tau_3$. The crosscorrelation of v_3 and P_P, which we have denoted $\tilde{\gamma}'_{k1}$, is given by

$$\tilde{\gamma}'_{k1}(\omega) = \alpha'_k\beta_1 \exp\left\{-i\omega\left[\tau_k^{(y)} - \tau_1^{(z)}\right]\right\} \ . \tag{5.40}$$

In the time domain, this field is

$$\tilde{\gamma}'_{k1}(t) = \alpha'_k\beta_1\delta\left[t - \tau_k^{(y)} + \tau_1^{(z)}\right] = \alpha_k\beta_l\delta\left[t - t_k^{(yz)}\right] \ , \tag{5.41}$$

where

$$t_k^{(yz)} = \tau_k^{(y)} - \tau_1^{(z)} \ . \tag{5.42}$$

$\tilde{\gamma}'_{kl}(t)$ is the Fourier transform of $\tilde{\gamma}'_{kl}(\omega)$. Notice that $t_k^{(yz)} > 0$, thus all the virtual events in $\tilde{\gamma}'_{kl}(t)$ are causal. The convolution of $\tilde{\gamma}'_{k1}$ with v_3 for predicting internal multiples, which we have denoted η_{kl1}, is given by

$$\eta_{kn1}(\omega) = \alpha'_k\alpha'_n\beta_1 \exp\left\{-i\omega\left[\tau_k^{(y)} - \tau_1^{(z)} + \tau_n^{(y)}\right]\right\} \ . \tag{5.43}$$

In the time domain, this field is

$$\eta_{kn1}(t) = \alpha'_k\beta_1\delta\left[t - \tau_k^{(y)} - \tau_n^{(y)} + \tau_1^{(z)}\right] = \alpha_k\beta_l\delta\left[t - t_{kn}^{(yzy)}\right] \ , \tag{5.44}$$

where

$$t_{kn}^{(yzy)} = \tau_k^{(y)} + \tau_n^{(y)} - \tau_1^{(z)} \ . \tag{5.45}$$

$\eta_{kn1}(t)$ is the Fourier transform of $\eta_{kn1}(\omega)$. So the traveltimes of internal multiples, denoted η_{kn1} in Figure 47(b), are $t_{kn}^{(yzy)}$. We can verify, for example, that the traveltime

of η_{111} is $t_{11}^{(yzy)} = 2\tau_1 + 4\tau_2$, that the traveltime of η_{121} is $t_{11}^{(yzy)} = 2\tau_1 + 4\tau_2 + 2\tau_3$, and that the traveltime of η_{311} is $t_{31}^{(yzy)} = 2\tau_1 + 6\tau_2 + 2\tau_3$. All these traveltimes are consistent with the scattering diagrams for the particular case in which the reflectors are assumed to be horizontal and the data are limited to zero offset.

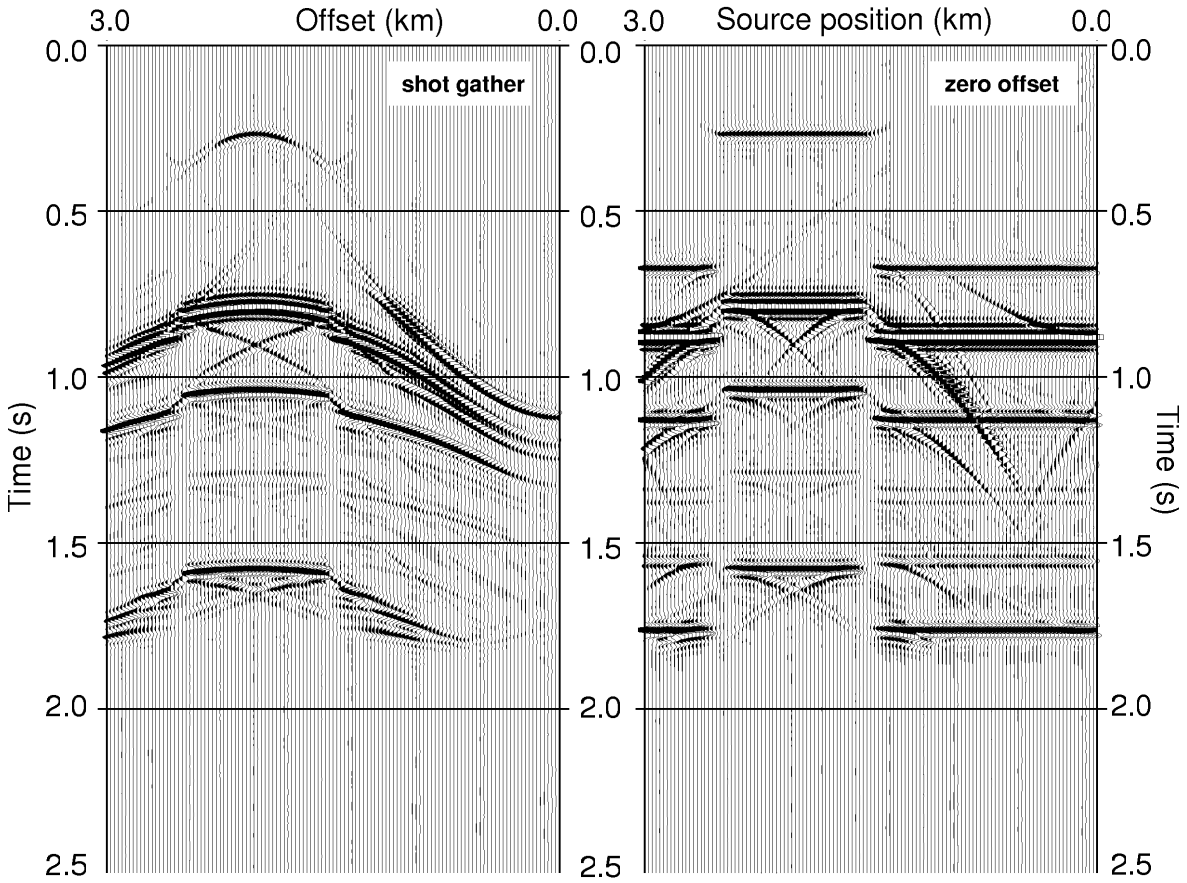

Fig. 48. The field of virtual events predicted. The field of virtual events predicted by using equation (5.31) for the particular case in which event α_1 has been removed from v_3 (Figure 43(a)) before applying equation (5.36). We need to remove this event from v_3 to avoid generating primaries. Notice that the field of virtual events does not contain an apparent direct wave.

Let us now use the data in Figure 43(a) to verify that the scheme described in Figures 47(a) and 47(b) not only accurately predicts the traveltimes of internal multiples but also accurately predicts their amplitudes. Figure 48 shows the field of virtual events predicted by using (5.31) for the particular case in which event α_1 has been removed from v_3 (Figure 43(a)) before applying (5.36). We need to remove this

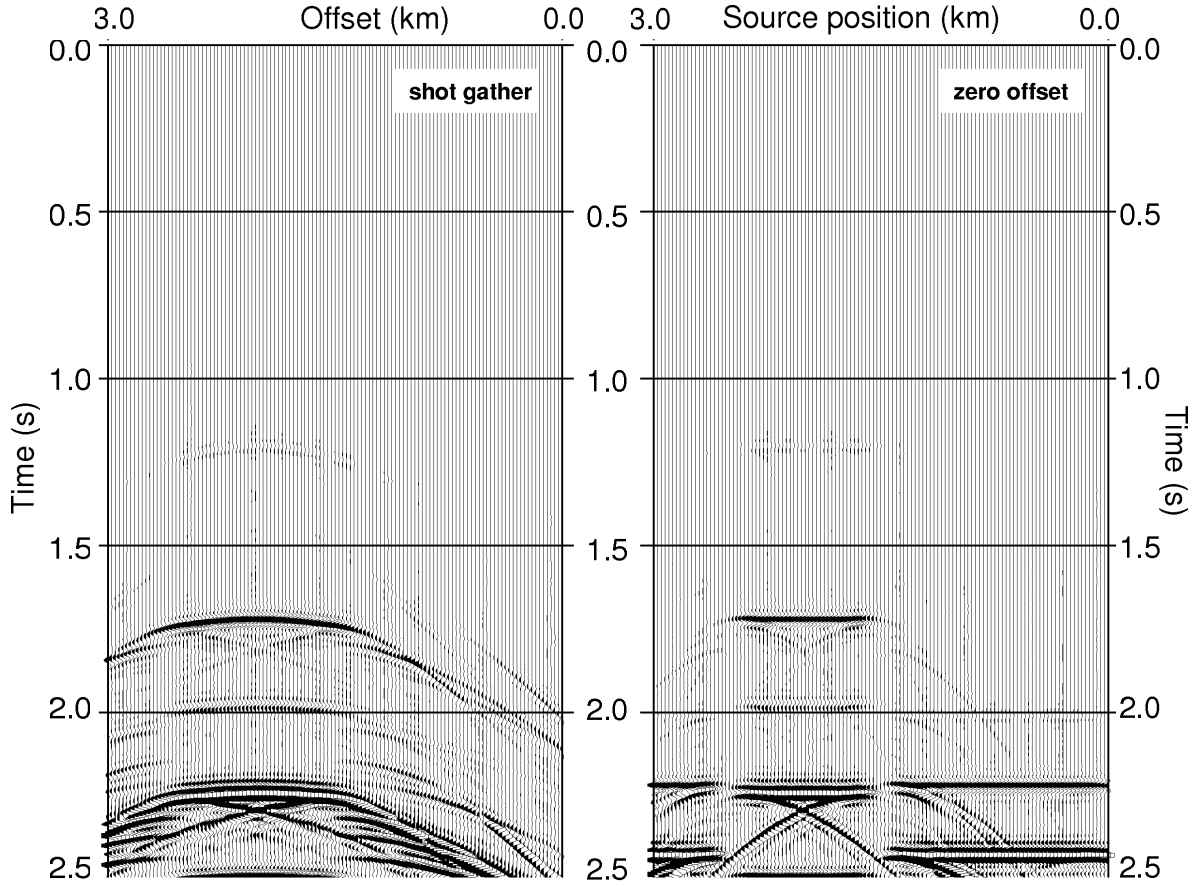

Fig. 49. The field of internal multiples obtained as the convolution of v_3 (Figure 43(a))—again without event α_1- with the field of virtual events based on equation (5.32).

event from v_3 to avoid generating primaries. Notice that the field of virtual events in Figure 48 does not contain an apparent direct wave. The convolution of v_3 (Figure 43(a))—again without event α_1—with the field of virtual events based on (5.32) produces the internal multiples in Figure 49. By using the subtraction technique described in (Ikelle et al., 1997), we then subtracted these predicted multiples from the data. The effectiveness of the internal-multiple-attenuation results in Figure 50(a) confirms that the amplitude of predicted internal multiples are consistent with that of the internal multiples in data.

The results in Figure 50(a) are limited to the attenuation of sea-floor internal multiples. Again, we can use the scheme in Figures 47(a) and 47(b) to iteratively remove any other internal multiples left in the data, as Figures 51, 52(a) and 52(b) show. The basic idea of the iteration process is to continuously segment the data at each iteration, as described in Figure 51. We call the boundary at which the data are segmented the *bottom internal-multiple generator* (BIMG) because, for a BIMG at a given iteration, all internal multiples with at least one bounce at the BIMG, or above the BIMG, are predicted and subtracted, as described in Figures 52(a) and 52(b). So at the first iteration, we predict and attenuate all the internal multiples which have at least one bounce above the first BIMG (which we denote BIMG1) and at least one below the BIMG1. In Figures 52(a) and 52(b) the data above the BIMG1 are denoted $P_{P1}(x_s, \omega, x)$ and $v_{31}(x_s, \omega, x)$, and the data below the BIMG1 are denoted $P'_{P1}(x, \omega, x_r)$ and $v'_{31}(x_s, \omega, x)$. The output of this iteration is used as the data for the next iteration.

In the second iteration, we move the BIMG deeper, to a new position, say, the BIMG2, and define new fields $P_{P2}(x_s, \omega, x)$, $v_{32}(x_s, \omega, x)$, $P'_{P2}(x, \omega, x_r)$, and $v'_{32}(x_s, \omega, x)$, as depicted in Figure 51. Notice that $P_{P2}(x_s, \omega, x)$i and $v_{32}(x_s, \omega, x)$ does not include data above the BIMG1. Then we predict and attenuate all the internal multiples which have at least one bounce between the BIMG1 and the BMG2, one bounce

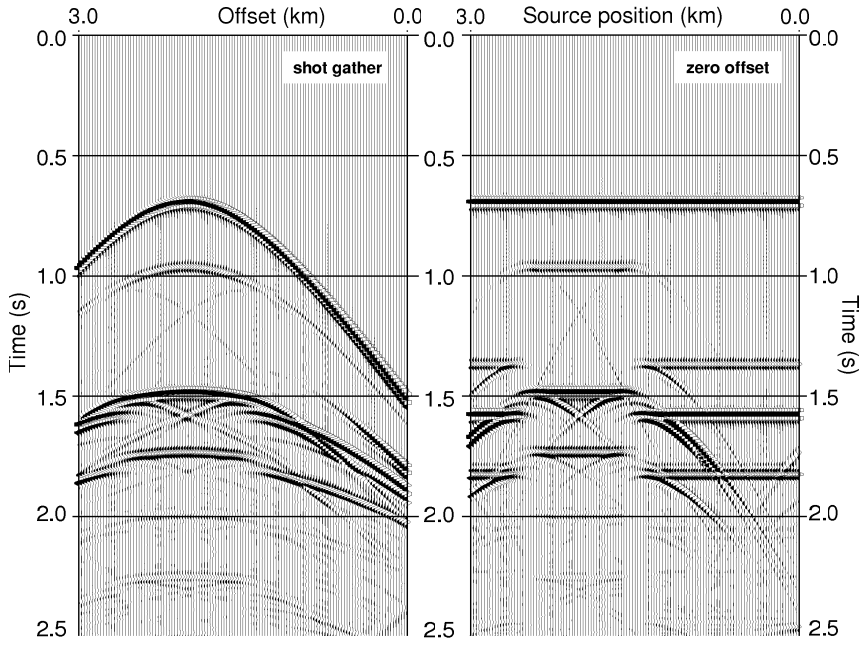

(a)

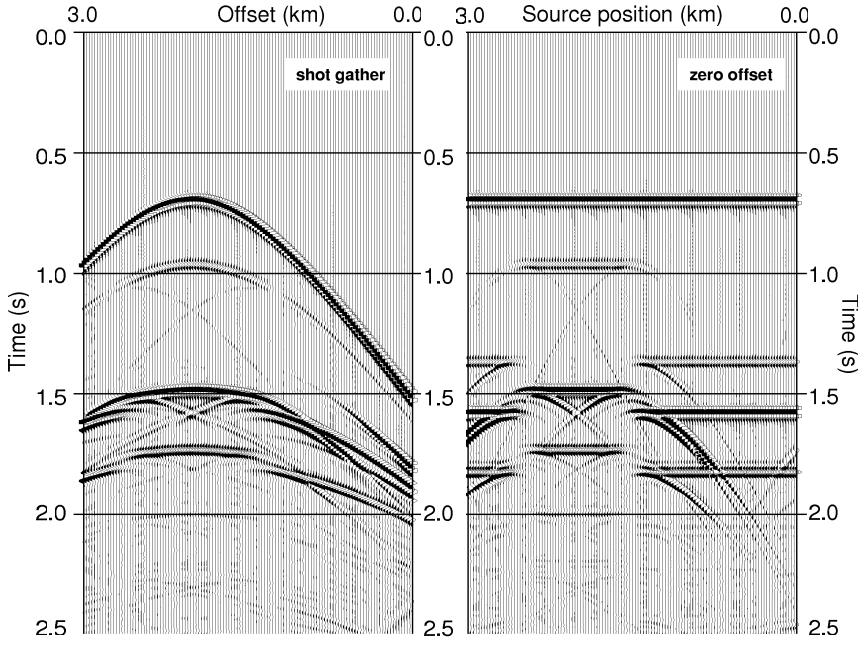

(b)

Fig. 50. By subtracting the predicted multiples in Figure 49 from the data, we obtained data without sea-floor-related multiples. (a) The first iteration results after subtraction. (b) A second iteration was performed based on the algorithm in Figures 51, 52(a), and 52(b). The BIMG in the second iteration was located above event α_4. Notice that we have attenuated the residual internal multiples.

below the BIMG2, and so on.

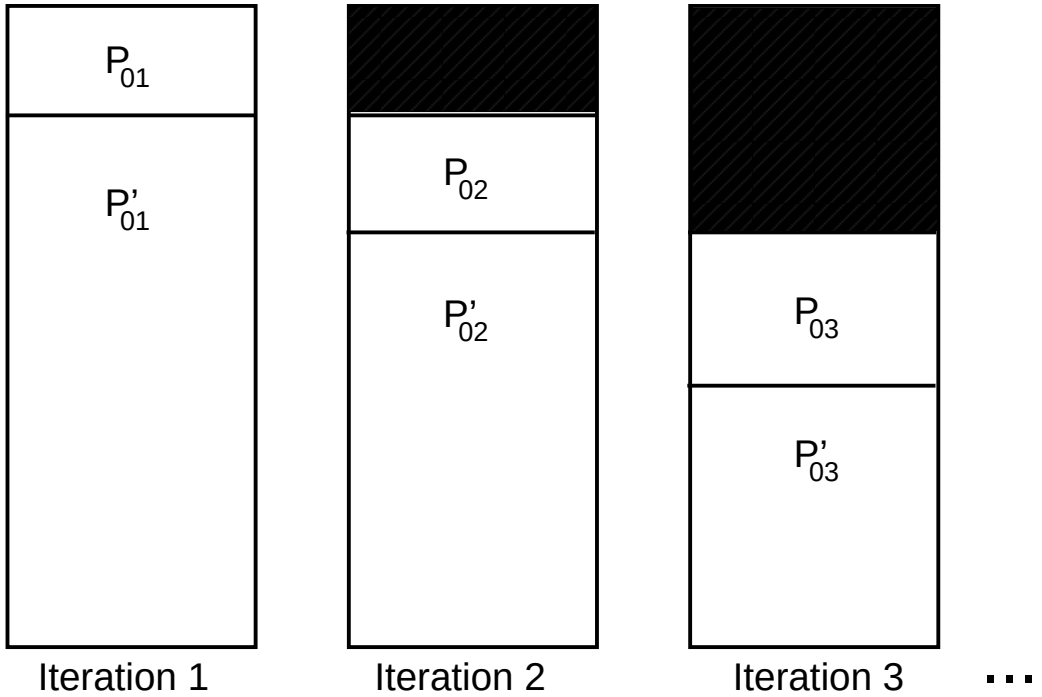

Fig. 51. An illustration of how we can progressively move the bottom internal-multiple generator (BIMG) to generate and attenuate several classes of internal multiples. This process is carried out iteratively. In the first iteration, we predict and attenuate all the internal multiples which have at least one bounce above the BIMG1 and at least one below the BIMG1. Using the output of this iteration as our new data, we then move the BIMG deeper to a new position: the BIMG2. We partition our new data in P_{02} and P'_{02}. Notice that P_{02} does not include data above the BIMG1. Then we predict and attenuate all the internal multiples which have at least one bounce located between the BIMG1 and the BIMG2, one bounce below the BIMG2, and so on.

Let us return to the data in Figure 43(a). We have applied the second iteration to demultiple result in Figure 50(a) to attenuate the residual internal multiples in this result. We select a BIMG2 location just above event α_4. We then repeat the process described in Figures 47(a) and 47(b),. Figure 50(b) shows the result of the second iteration. As we can see, the residual internal multiples located below 2 s have been attenuated even further.

Notice that arbitrary trajectories can be used for selecting the BIMG locations. In other words, one portion of an event may be located above the BIMG, and the other portion of the same event may be located below the BIMG. This separation

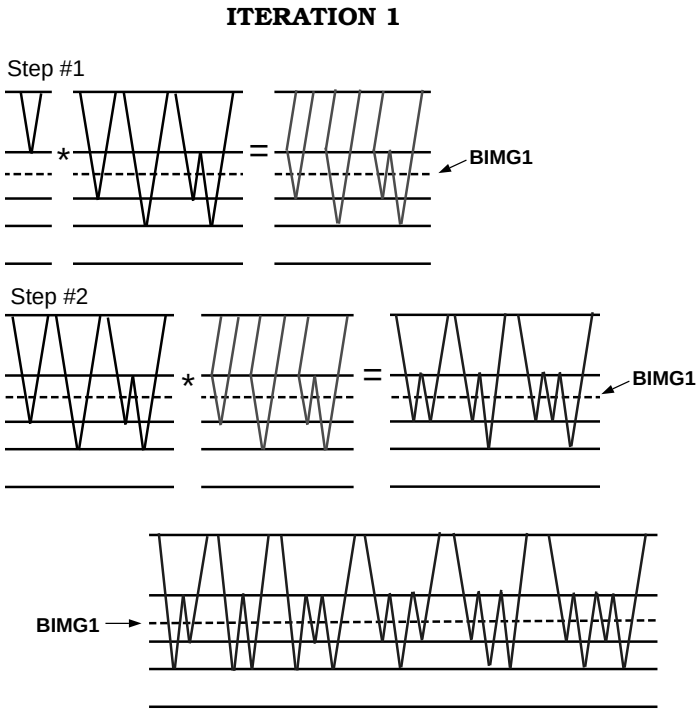

(a)

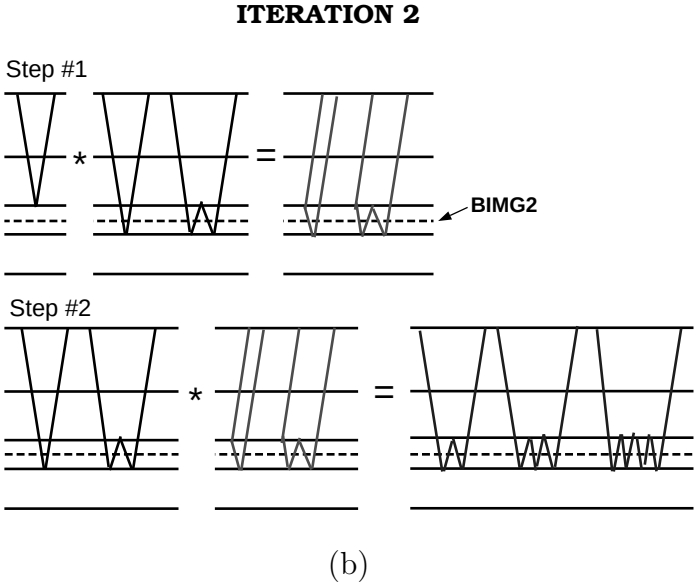

(b)

Fig. 52. An illustration with scattering diagrams of the first two iterations of the iterative process described in Figure 51. (a) The first iteration predicts and attenuates all the internal multiples which have at least one bounce above the BIMG1 and at least one below the BIMG1. The output of this iteration is used as the data for the second iteration. (b) In the second iteration, we predict and attenuate all the internal multiples which have at least one bounce located between the BIMG1 and the BIMG2, one bounce below the BIMG2, and so on.

is not a problem; the portion of the event located above the BIMG will be used to predict internal multiples in one iteration, and the second portion of the event located below the BIMG will be used in the next iteration to predict the second set of internal multiples associated with the event located below the BIMG. In other words, the fact that some complex events may not fall completely above the BIMG or completely below the BIMG is another reason why the iterative process described in Figures 51, 52(a) and 52(b) is necessary. (Ikelle et al., 2004), (Watts and Ikelle, 2005) and (Watts and Ikelle, 2006) show examples of this point for complex models containing salt bodies in the context of free-surface multiples. (Erez, 2006) in her thesis also makes this point for internal multiples.

CONCLUSIONS

We have described a diagrammatica of seismic events as they relate to Kirchhoff scattering integrals of the convolution- and crosscorrelation-type representation theorems. In particular, we pointed out that the crosscorrelation operation in the correlation-type representation theorem creates events which combine backward and forward-wave propagation in its wave-propagation paths. We have named these events virtual events. Furthermore, we show that seismic events can be created as either combinations of forward-propagating events or combinations of forward- and backward-propagating events. Other events, which are not recorded in seismic acquisition and not necessarily causal, can also be created by a combinations of forward and backward propagating events. We show that the construction of such events can be useful in the process of attenuating internal multiples. In a companion paper to this one, we also show the events which include forward and backward propagations can be used to derive new imaging algorithms which are less sensitive to the background velocity model.

CHAPTER VI

CONCLUSIONS

In this dissertation I have developed a 3D staggered-grid finite-difference modeling program. I have also applied an absorbing boundary condition and discussed the criteria which ensures the numerical stability. First I have verified the 3D finite-difference modeling code by comparing the modeled data with analytical solution in homogeneous medium; then I provided additional numerical examples to verify that the finite-difference modeling program can properly simulate reflections, transmission and converted-waves. I have also shown that the 3D finite-difference modeling program can simulate both marine and land seismic data acquisition.

First the application of the finite-difference modeling in improving the illumination of a complex salt model is shown. A complex salt model which describes a shallow marine environment in the Gulf of Mexico is used. The resulting data is quite complicated, direct wave, water bottom reflection, top salt reflection, bottom salt reflection, strong diffractions, and subsalt reflections are present in both shot gather and zero-offset data. The subsalt reflection is very weak in the shot gather data. The zero-offset data show a stronger signal for subsalt reflection where the salt body is thinner. I also point out that 3D finite-difference modeling is an expensive tool, which is the reason that it is still not a widely used in exploration and production industry.

I have shown the application of the 3D finite-difference program in anisotropic media. The synthetic data in both VTI and HTI models show travel time anisotropy for both P and S waves. I have also shown that we can successfully model shear-wave splitting and triplication.

I have described a diagrammatica of seismic events as they relate to Kirchhoff scattering integrals of the convolution- and crosscorrelation-type representation

theorems. In particular, I pointed out that the crosscorrelation operation in the correlation-type representation theorem creates events which combine backward and forward-wave propagation in its wave-propagation paths. I have shown the wave propagation of virtual events generated by crosscorrelation-type representation theorem.

Furthermore, I show that seismic events can be created as either combinations of forward-propagating events or combinations of forward- and backward-propagating events. Other events, which are not recorded in seismic acquisition and not necessarily causal, can also be created by a combinations of forward and backward propagating events. I show that the construction of such events can be useful in the process of attenuating internal multiples.

REFERENCES

Abramowitz, M., and Stegun, I., 1964, Handbook of mathematical functions with formulas, graphs, and mathematical tables: Dover.

Aki, K., and Richards, P. G., 1980, Quantitative seismology: Theory and methods: W.H. Freeman and Co.

Amundsen, L., Ikelle, L. T., and Berg, L., 2001, Multidimensional signature deconvolution and free-surface multiple elimination of 4C data: Geophysics, **66**, 1594–1604.

Amundsen, L., 2001, Elimination of free-surface related multiples without need of the source wavelet: Geophysics, **66**, 327–341.

Berkhout, A. J., and Verschuur, D. J., 2005, Removal of internal multiples with the common-focus-point (CFP) approach: Part1-Explanation of the theory: Geophysics, **70**, V45–V60.

Bojarski, N., 1983, Generalized reaction principles and reciprocity theorems for the wave equation, and the relationship between the time-advanced and time-retarded field: J. Acoust. Soc. Am., **74**, 281–285.

Cerjan, C., Kosloff, D., Kosloff, R., and Reshef, M., 1985, A nonreflecting boundary condition for discrete acoustic and elastic wave equations: Geophysics, **50**, 705–708.

Clayton, R., and Engquist, B., 1977, Absorbing boundary conditions for acoustic and elastic wave equations: Bulletin of the Seismological Society of America, **67**, 1529–1540.

de Hoop, A. T., 1966, An elastodynamic reciprocity theorem for linear, viscoelastic media: Appl. Sci. Res., **16**, 39–45.

——— 1995, Handbook of radiation and scattering of waves: Academic Press, San Diego, CA.

Derode, A., Larose, E., Campilllo, M., and Fink, M., 2003, How to estimate the green's function of a heterogeneous medium between two passive sensors? Application to acoustic waves: Applied Physics Letters, **83**, 3054–3056.

Erez, I., 2006, The concept of virtual events and its applications to the attenuation of internal multiples and the separation of reflected and refracted waves: M.S. thesis, Texas A&M University, College Station, Texas.

Fokkema, J. T., and van den Berg, P. M., 1990, Removal of surface-related wave phenomena: The marine case: 60th Ann. Internat. Mtg., Soc. Expl. Geophys., Expanded Abstracts, 1689–1692.

——— 1993, Seismic applications of acoustic reciprocity: Elsevier Science Publ.

Gangi, A. F., 1970, A derivation of the seismic representation theorem using seismic reciprocity: J. Geophys. Res., **75**, 2088–2095.

Graves, R. W., 1996, Simulating seismic wave propagation in 3D elastic media using staggered-grid finite difference: Bulletin of the Seismological Society of America, **86**, 1091–1106.

Ikelle, L. T., and Amundson, L., 2005, Introduction to petroleum seismology: Society of exploration Geophysicists.

Ikelle, L. T., and Gangi, A. F., 2005, New type of reflections in inhomogeneous media is revealed by an analysis of scattering diagrams of correlation-type representation theorem: Journal of Seismic Exploration, **55**, 1–12.

——— 2007, Negative bending in seismic reflection associated with time-advanced and time-retarded fields: Geophysical Prospecting, **55**, 57–69.

Ikelle, L. T., Roberts, G., and Weglein, A. B., 1997, Source signature estimation based on the removal of first-order multiples: Geophysics, **62**, 1904–1920.

Ikelle, L. T., Gangi, A. F., and Wyatt, S., 2003, Kirchhoff scattering series: Insight into the multiple attenuation method: Geophysics, **68**, 16–28.

Ikelle, L. T., Osen, A., Amundsen, L., and Shen, Y., 2004, Noniterative multiple-attenuation methods: Linear inverse solutions to nonlinear inverse problems ii - BMG approximation: Geophysical Journal International, **159**, 923–930.

Ikelle, L. T., 2004, A construct of internal multiples from surface data only: 74th Ann. Internat. Mtg., Soc. Expl. Geophys., Expanded Abstracts, 2164–2167.

——— 2006, A construct of internal multiples from surface data only: The concept of virtual seismic events: Geophysical Journal International, **164**, 383–393.

Kennett, B. L. N., 1979, The suppression of surface multiples on seismic records: Geophysical Prospecting, **27**, 584–600.

Levander, A. R., 1988, Fourth-order finite-difference P-SV seismograms: Geophysics, **53**, 1425–1436.

Madariaga, R., 1976, Dynamics of an expanding circular fault: Bulletin of the Seismological Society of America, **66**, 639–666.

Moczo, P., Kristek, J., and Halada, L., 2000, 3D fourth-order staggered-grid finite-difference schemes: Stability and grid dispersion: Bulletin of the Seismological Society of America, **90**, 587–603.

Rickett, J., and Claerbout, J., 1999, Acoustic daylight via spectral factorization: Helioseismology and reservoir monitoring: The Leading Edge, **18**, 957–960.

Roux, P., and Fink, M., 2003, Green's function estimation using secondary sources in a shallow water environment: J. Acoust. Soc. Am., **113**, 1406–1416.

Schuster, G. T., Yu, J., Sheng, J., and Rickett, J., 2004, Interferometric/daylight seismic imaging: Geophysical Journal International, **157**, 838–852.

Snieder, R., Yu, J., Sheng, J., and Rickett, J., 2004, Extracting the green's function from the correlation of coda waves: A derivation based on stationary phase: Physical Review E, **69**, 046610(1–8).

Sommerfeld, A., 1954, Optics: Academic Press, New York.

van Manen, D. J., Robertsson, J. O. A., and Curtis, A., 2005, Modeling of wave propagation in inhomogeneous media: Physical Review Letters, **94**, 164301.

Verschuur, D. J., and Berkhout, A. J., 2005, Removal of internal multiples with the common-focus-point (CFP) approach: Part2 - Application strategies and data examples: Geophysics, **70**, V61–V72.

Veselago, V. G., 1968, The electrodynamics of substances with simultaneously negative values of ε and μ: Soviet Physics Uspekhi, **10**, 509–514.

Wapenaar, K., 2004, Retrieving the elastodynamic green's function of an arbitrary inhomogeneous medium by crosscorrelation: Physical Review Letter, **93**, 254301.

Watts, A. O., and Ikelle, L. T., 2005, Linear demultiple solutions based on the concept of bottom multiple generator (BMG) approximation: Some new results: 75th Ann. Internat. Mtg., Soc. Expl. Geophys., Expanded Abstracts, 2134–2137.

——— 2006, Linear demultiple solutions based on the concept of bottom multiple generator (BMG) approximation: Some new results: Geophysical Prospective, in press.

Winterstein, D. F., 1989, Velocity anisotropy terminology for geophysicists: Geophysics, **55**, 1070–1088.

Ziolkowski, A. M., Taylor, D. B., and Johnston, R. G. K., 1999, Marine seismic wavefield measurement to remove sea-surface multiples: Geophysical Prospective, **47**, 841–870.

APPENDIX A

A FORTRAN 3D FINITE-DIFFERENCE CODE

In this appendix, a Fortran code of the 3D staggered-grid finite-difference modeling code that we have developed in chapter II will be provided. This code is for 3D heterogeneous, isotropic elastic media. Most of the numerical examples shown in chapter II are generated using this code. The extension to anisotropic case is very straightforward, we just have to deal with longer stress strain relationship equations.

Key parameters and physical quantities:

nx, ny, nz:	number of grid points in x, y and z-direction
dx:	grid spacing in meters
	(note that $\Delta x = \Delta y = \Delta z$ in this code)
dt:	timestep in seconds
nmax:	number of timesteps
xsrc, ysrc, zsrc:	source location in grid points
freq:	central frequency for Ricker wavelet
txx, tyy, tzz, tyz, txz, txy:	stress components $(\tau_{xx}, \tau_{yy}, \tau_{zz}, \tau_{yz}, \tau_{xz}, \tau_{xy})$
isotype:	specify the source type
	1=pressure source
	2=vertical source
	3=horizontal source
	4=shear source

nsnap:	maximum number of snapshots to be output
idsnap:	timestep increment between snapshots to be output
topbc:	specifies the type of boundary condition at $z = 0$
	topbc='free' indicates the free surface boundary condition
	topbc='abbc' indicates the absorbing boundary condition
iabmax:	width of the absorbing boundary in grid points

Fortran code:

```
c       ***********************************************
c       3D elastic FDM code
c       ***********************************************
        double precision eponge,vx,vz,vy,txx,tyy,tzz,txz,txy,tyz
        double precision exx, ezz, eyy, exy, exz, eyz, vp, vs, dens
        parameter (nx=300, ny=300, nz=300, dx=5)
        parameter (nmax=500, dt=0.5e-3, nstep=1)
        parameter (nsrc=1, xsrc=150, ysrc=150, zsrc=150, freq=25)
        parameter (nsnap=2, idsnap=500)
        parameter (isotype=1)                                          10
        parameter (iabmax = 30)
        parameter (topbc='abbc')
        parameter (eps=1.e-6)
c       topbc is either 'free' (model with fs) or 'abbc' (no fs)
c       [i.e., parameter (topbc='abbc')]
        dimension vx(nx,ny,nz), vy(nx,ny,nz)
        dimension vz(nx,ny,nz), txx(nx,ny,nz)
        dimension tyy(nx,ny,nz), tzz(nx,ny,nz)
        dimension txy(nx,ny,nz), txz(nx,ny,nz)
```

```
      dimension tyz(nx,ny,nz), vp(nx,ny,nz)
      dimension vs(nx,ny,nz), dens(nx,ny,nz)
      dimension source(nmax), eponge(iabmax)
c
      f1 = -1.0/24.0
      f2 = 9.0/8.0
c
      dtdx=dt/dx
      dtdxh = dtdx*0.5
      dtdxq = dtdx*4.0
      ixs=xsrc
      iys=ysrc
      izs=zsrc
c
c ... coordinates of shot point and scaling factor for the source
c
      soufac = dt/(dx*dx*dx)
      print *,' ixs=', ixs, iys, izs, soufac, dtdx
c
      isnap = 0
c
c ... source signature
c
      call ricker(nmax,dt,freq,source)
      print *,'wavelet'
c
c ... the damping coefficients for bc
```

```
c
      a0=0.3/float(iabmax)
      do ii=1,iabmax
         eponge(ii)=exp(-(a0*float(iabmax-ii))**2)
      enddo
c
c ...    initializes displacements, pressures, boundary conditions
c
      do i=1,nx
         do j=1,ny
            do k=1,nz
               vx(i,j,k) =0.0
               vy(i,j,k) =0.0
               vz(i,j,k) =0.0
               txx(i,j,k)=0.0
               tyy(i,j,k)=0.0
               tzz(i,j,k)=0.0
               txz(i,j,k)=0.0
               txy(i,j,k)=0.0
               tyz(i,j,k)=0.0
               vs(i,j,k)=0.0
            enddo
         enddo
      enddo
c
c ... reading the 3D model
c
```

```
      do i=1,nx
         do j=1,ny
            do k=1,nz
               vp(i,j,k) =2000.0
               vs(i,j,k)=1900.0
               dens(i,j,k)=1100.0
            enddo
         enddo
      enddo

c ========================================
c     Equations of momentum conservation
c ========================================
c
      do n=1,nmax
c
      do k=3,nz-2
         do j=3,ny-2
            do i=3,nx-2
c
               rhox   = 1./dens(i+1,j,k)
               rhoy   = 1./dens(i,j+1,k)
               rhoz   = 1./dens(i,j,k+1)
               rhoa   = 1./dens(i,j,k)
c
               bx     = dtdxh*(rhoa+rhox)
               by     = dtdxh*(rhoa+rhoy)
```

```
                bz      = dtdxh*(rhoa+rhoz)


                vx(i,j,k)=vx(i,j,k)+bx*
     *   (f1*(txx(i+2,j,k)-txx(i-1,j,k))+f2*(txx(i+1,j,k)-txx(i,j,k))+
     *    f1*(txy(i,j+1,k)-txy(i,j-2,k))+f2*(txy(i,j,k)-txy(i,j-1,k))+
     *    f1*(txz(i,j,k+1)-txz(i,j,k-2))+f2*(txz(i,j,k)-txz(i,j,k-1)))
c
                vy(i,j,k)=vy(i,j,k)+by*
     *   (f1*(txy(i+1,j,k)-txy(i-2,j,k))+f2*(txy(i,j,k)-txy(i-1,j,k))+
     *    f1*(tyy(i,j+2,k)-tyy(i,j-1,k))+f2*(tyy(i,j+1,k)-tyy(i,j,k))+
     *    f1*(tyz(i,j,k+1)-tyz(i,j,k-2))+f2*(tyz(i,j,k)-tyz(i,j,k-1)))
c
                vz(i,j,k)=vz(i,j,k)+bz*
     *   (f1*(txz(i+1,j,k)-txz(i-2,j,k))+f2*(txz(i,j,k)-txz(i-1,j,k))+
     *    f1*(tyz(i,j+1,k)-tyz(i,j-2,k))+f2*(tyz(i,j,k)-tyz(i,j-1,k))+
     *    f1*(tzz(i,j,k+2)-tzz(i,j,k-1))+f2*(tzz(i,j,k+1)-tzz(i,j,k)))
          enddo
        enddo
      enddo
c
      if(mod(n,100).eq.0) print *, 'Timestep=',n
c
c ...  absorbing bc (X-axis left and right)
c
      do ka=1,nz
        do ja=1,ny
          do ia=1,iabmax
```

```
                vx(ia,ja,ka)=vx(ia,ja,ka)*eponge(ia)
                vy(ia,ja,ka)=vy(ia,ja,ka)*eponge(ia)
                vz(ia,ja,ka)=vz(ia,ja,ka)*eponge(ia)
                vx(nx-ia+1,ja,ka)=vx(nx-ia+1,ja,ka)*eponge(ia)
                vy(nx-ia+1,ja,ka)=vy(nx-ia+1,ja,ka)*eponge(ia)
                vz(nx-ia+1,ja,ka)=vz(nx-ia+1,ja,ka)*eponge(ia)
             enddo
          enddo
       enddo
c
c ...  absorbing bc (Y-axis left and right)
c
       do ka=1,nz
          do ja=1,iabmax
             do ia=1,nx
                vx(ia,ja,ka)=vx(ia,ja,ka)*eponge(ja)
                vy(ia,ja,ka)=vy(ia,ja,ka)*eponge(ja)
                vz(ia,ja,ka)=vz(ia,ja,ka)*eponge(ja)
                vx(ia,ny-ja+1,ka)=vx(ia,ny-ja+1,ka)*eponge(ja)
                vy(ia,ny-ja+1,ka)=vy(ia,ny-ja+1,ka)*eponge(ja)
                vz(ia,ny-ja+1,ka)=vz(ia,ny-ja+1,ka)*eponge(ja)
             enddo
          enddo
       enddo
c
c ... absorbing bc (top and bottom)
c
```

```
      do ka=1,iabmax
         do ja=1,ny
            do ia=1,nx
               if(topbc.eq.'abbc') then
                  vx(ia,ja,ka)=vx(ia,ja,ka)*eponge(ka)
                  vy(ia,ja,ka)=vy(ia,ja,ka)*eponge(ka)
                  vz(ia,ja,ka)=vz(ia,ja,ka)*eponge(ka)
               endif
               vx(ia,ja,nz-ka+1)=vx(ia,ja,nz-ka+1)*eponge(ka)
               vy(ia,ja,nz-ka+1)=vy(ia,ja,nz-ka+1)*eponge(ka)
               vz(ia,ja,nz-ka+1)=vz(ia,ja,nz-ka+1)*eponge(ka)
            enddo
         enddo
      enddo
c
c .... add horizontal force in x axis
c
      if(isotype.eq.2) then
         addsou=0.25*soufac*source(n)
         vx(ixs,iys,izs)=vx(ixs,iys,izs)+addsou
      endif
c
c .... add vertical force source
c
      if(isotype.eq.3) then
         addsou=0.25*soufac*source(n)
         vz(ixs,iys,izs)=vz(ixs,iys,izs)+addsou
```

```
      endif
c =========================================
c     Stress-strain relations for an isotropic elastic medium
c =========================================
      do k=3,nz-2
        do j=3,ny-2
          do i=3,nx-2
c
            rho    = dens(i,j,k)                                    190
            xrlamu = vp(i,j,k)*vp(i,j,k)*rho
            xmu    = vs(i,j,k)*vs(i,j,k)*rho
            xrlam  = xrlamu-2.0*xmu
c
            rlamu  = dtdx*xrlamu
            rlam   = dtdx*xrlam
c
            xmu100  = vs(i+1,j,k)*vs(i+1,j,k)*dens(i+1,j,k)
            xmu010  = vs(i,j+1,k)*vs(i,j+1,k)*dens(i,j+1,k)
            xmu001  = vs(i,j,k+1)*vs(i,j,k+1)*dens(i,j,k+1)          200
            xmu110  = vs(i+1,j+1,k)*vs(i+1,j+1,k)*dens(i+1,j+1,k)
            xmu101  = vs(i+1,j,k+1)*vs(i+1,j,k+1)*dens(i+1,j,k+1)
            xmu011  = vs(i,j+1,k+1)*vs(i,j+1,k+1)*dens(i,j+1,k+1)
c
            xmu000 = 1./(xmu+eps)
            xmu100 = 1./(xmu100+eps)
            xmu010 = 1./(xmu010+eps)
            xmu001 = 1./(xmu001+eps)
```

```
                xmu110 = 1./(xmu110+eps)
                xmu101 = 1./(xmu101+eps)
                xmu011 = 1./(xmu011+eps)
c
                vmuxy  = dtdxq/(xmu000+xmu100+xmu010+xmu110)
                vmuxz  = dtdxq/(xmu000+xmu100+xmu001+xmu101)
                vmuyz  = dtdxq/(xmu000+xmu010+xmu001+xmu011)
c
                if(vmuxy.lt.1.0) vmuxy = 0.0
                if(vmuxz.lt.1.0) vmuxz = 0.0
                if(vmuyz.lt.1.0) vmuyz = 0.0
c
c...  calculate xx, yy, zz strains
c
      exx =f2*(vx(i,j,k)-vx(i-1,j,k))+f1*(vx(i+1,j,k)-vx(i-2,j,k))
      eyy =f2*(vy(i,j,k)-vy(i,j-1,k))+f1*(vy(i,j+1,k)-vy(i,j-2,k))
      ezz =f2*(vz(i,j,k)-vz(i,j,k-1))+f1*(vz(i,j,k+1)-vz(i,j,k-2))
c
c...  calculate yy strains
c
      exy =f1*(vy(i+2,j,k)-vy(i-1,j,k))+f2*(vy(i+1,j,k)-vy(i,j,k))+
     +     f1*(vx(i,j+2,k)-vx(i,j-1,k))+f2*(vx(i,j+1,k)-vx(i,j,k))
c
      exz =f1*(vz(i+2,j,k)-vz(i-1,j,k))+f2*(vz(i+1,j,k)-vz(i,j,k))+
     +     f1*(vx(i,j,k+2)-vx(i,j,k-1))+f2*(vx(i,j,k+1)-vx(i,j,k))
c
      eyz =f1*(vy(i,j,k+2)-vy(i,j,k-1))+f2*(vy(i,j,k+1)-vy(i,j,k))+
```

```
     +      f1*(vz(i,j+2,k)−vz(i,j−1,k))+f2*(vz(i,j+1,k)−vz(i,j,k))
c
c...  calculate stresses
c
      txx(i,j,k)=txx(i,j,k)+(rlamu*exx)+(rlam*(eyy+ezz))                    240
      tyy(i,j,k)=tyy(i,j,k)+(rlamu*eyy)+(rlam*(exx+ezz))
      tzz(i,j,k)=tzz(i,j,k)+(rlamu*ezz)+(rlam*(exx+eyy))
      tyz(i,j,k)=tyz(i,j,k)+(vmuyz*eyz)
      txz(i,j,k)=txz(i,j,k)+(vmuxz*exz)
      txy(i,j,k)=txy(i,j,k)+(vmuxy*exy)
         enddo
       enddo
      enddo
c
c ...  absorbing bc (X-axis left and right)                               250
c
      do ka=1,nz
       do ja=1,ny
        do ia=1,iabmax
          txx(ia,ja,ka)=txx(ia,ja,ka)*eponge(ia)
          tyy(ia,ja,ka)=tyy(ia,ja,ka)*eponge(ia)
          tzz(ia,ja,ka)=tzz(ia,ja,ka)*eponge(ia)
          tyz(ia,ja,ka)=tyz(ia,ja,ka)*eponge(ia)
          txz(ia,ja,ka)=txz(ia,ja,ka)*eponge(ia)
          txy(ia,ja,ka)=txy(ia,ja,ka)*eponge(ia)                            260
          txx(nx−ia+1,ja,ka)=txx(nx−ia+1,ja,ka)*eponge(ia)
          tyy(nx−ia+1,ja,ka)=tyy(nx−ia+1,ja,ka)*eponge(ia)
```

```
            tzz(nx−ia+1,ja,ka)=tzz(nx−ia+1,ja,ka)*eponge(ia)
            tyz(nx−ia+1,ja,ka)=tyz(nx−ia+1,ja,ka)*eponge(ia)
            txz(nx−ia+1,ja,ka)=txz(nx−ia+1,ja,ka)*eponge(ia)
            txy(nx−ia+1,ja,ka)=txy(nx−ia+1,ja,ka)*eponge(ia)
          enddo
        enddo
      enddo
c                                                                    270
c ...  absorbing bc (Y-axis left and right)
c
      do ka=1,nz
        do ja=1,iabmax
          do ia=1,nx
            txx(ia,ja,ka)=txx(ia,ja,ka)*eponge(ja)
            tyy(ia,ja,ka)=tyy(ia,ja,ka)*eponge(ja)
            tzz(ia,ja,ka)=tzz(ia,ja,ka)*eponge(ja)
            tyz(ia,ja,ka)=tyz(ia,ja,ka)*eponge(ja)
            txz(ia,ja,ka)=txz(ia,ja,ka)*eponge(ja)                   280
            txy(ia,ja,ka)=txy(ia,ja,ka)*eponge(ja)
            txx(ia,ny−ja+1,ka)=txx(ia,ny−ja+1,ka)*eponge(ja)
            tyy(ia,ny−ja+1,ka)=tyy(ia,ny−ja+1,ka)*eponge(ja)
            tzz(ia,ny−ja+1,ka)=tzz(ia,ny−ja+1,ka)*eponge(ja)
            tyz(ia,ny−ja+1,ka)=tyz(ia,ny−ja+1,ka)*eponge(ja)
            txz(ia,ny−ja+1,ka)=txz(ia,ny−ja+1,ka)*eponge(ja)
            txy(ia,ny−ja+1,ka)=txy(ia,ny−ja+1,ka)*eponge(ja)
          enddo
        enddo
```

```
      enddo                                                          290
c
c ...  absorbing bc (top and bottom)
c
      do ka=1,iabmax
        do ja=1,ny
          do ia=1,nx
          if(topbc .eq. 'abbc') then
            txx(ia,ja,ka)=txx(ia,ja,ka)*eponge(ka)
            tyy(ia,ja,ka)=tyy(ia,ja,ka)*eponge(ka)
            tzz(ia,ja,ka)=tzz(ia,ja,ka)*eponge(ka)                   300
            tyz(ia,ja,ka)=tyz(ia,ja,ka)*eponge(ka)
            txz(ia,ja,ka)=txz(ia,ja,ka)*eponge(ka)
            txy(ia,ja,ka)=txy(ia,ja,ka)*eponge(ka)
          endif
            txx(ia,ja,nz-ka+1)=txx(ia,ja,nz-ka+1)*eponge(ka)
            tyy(ia,ja,nz-ka+1)=tyy(ia,ja,nz-ka+1)*eponge(ka)
            tzz(ia,ja,nz-ka+1)=tzz(ia,ja,nz-ka+1)*eponge(ka)
            tyz(ia,ja,nz-ka+1)=tyz(ia,ja,nz-ka+1)*eponge(ka)
            txz(ia,ja,nz-ka+1)=txz(ia,ja,nz-ka+1)*eponge(ka)
            txy(ia,ja,nz-ka+1)=txy(ia,ja,nz-ka+1)*eponge(ka)         310
          enddo
        enddo
      enddo
c
c...  adds stress type sources
c
```

```
      if(isotype.eq.1) then
        addsou=soufac*source(n)
        txx(ixs,iys,izs)=txx(ixs,iys,izs)+addsou
        tyy(ixs,iys,izs)=tyy(ixs,iys,izs)+addsou                    320
        tzz(ixs,iys,izs)=tzz(ixs,iys,izs)+addsou
       endif
c
c... adds stress type sources: shear source
c
      if(isotype.eq.4) then
        addsou=soufac*source(n)
        txx(ixs,iys,izs)=txx(ixs,iys,izs)+addsou
        tyy(ixs,iys,izs)=tyy(ixs,iys,izs)+addsou
        tzz(ixs,iys,izs)=tzz(ixs,iys,izs)-(2.0*addsou)              330
       endif
c
       if(mod(n,idsnap).eq.0.and.isnap.lt.nsnap) then
         do i=1,nx
           do j=1,ny
             do k=1,nz
              bbb=txx(i,j,k)+tyy(i,j,k)+tzz(i,j,k)
                write(65+isnap,*) bbb
             enddo
           enddo                                                    340
         enddo
         isnap = isnap+1
       endif
```

```
      enddo
      stop
      end
c
c++++++++++++++++++++++++++++++++++++++++
c+   wavelet calculates the source signature                +
c++++++++++++++++++++++++++++++++++++++++
c
      subroutine ricker(nt,dt,freq,wav)
c
      dimension wav(*)
      dimension tmp(nt)

      timesh = 1.0/freq
      pi2 = 0.8862
      const = 6.2832*freq

      do i=1,nt
         wav(i) = 0.0
         tmp(i) = 0.0
      enddo
c
      wavmax=0.0
      do i=1,nt
         tim1 = (i-1)*dt
         tim2 = tim1-timesh
         uuu = const*tim2
```

```
      tmp(i) = (uuu**2/4.0 - 0.5)*pi2*(exp(-uuu**2/4.0))
      if(wavmax.lt.abs(tmp(i))) wavmax = abs(tmp(i))
    enddo
c
    do i=1,nt
      wav(i) = tmp(i)/wavmax
    enddo
c
    return
    end                                                    380
```

APPENDIX B

THE STAGGERED-GRID FORMULATION

The goal in this appendix is to show that the staggered-grid formulation in Figure 2 (chapter II) is not unique. By choosing one set of quantities for the reference grid, wave equations (2.15) and (2.16) automatically impose the grid positions of the other quantities as the derivatives must assign with the positions in the grids. In 3D, the staggered-grid formulation has eight possible combinations totally. In this appendix, we will provide all the other possible choices of stagger-grid formulation besides the one shown in Figure 2.

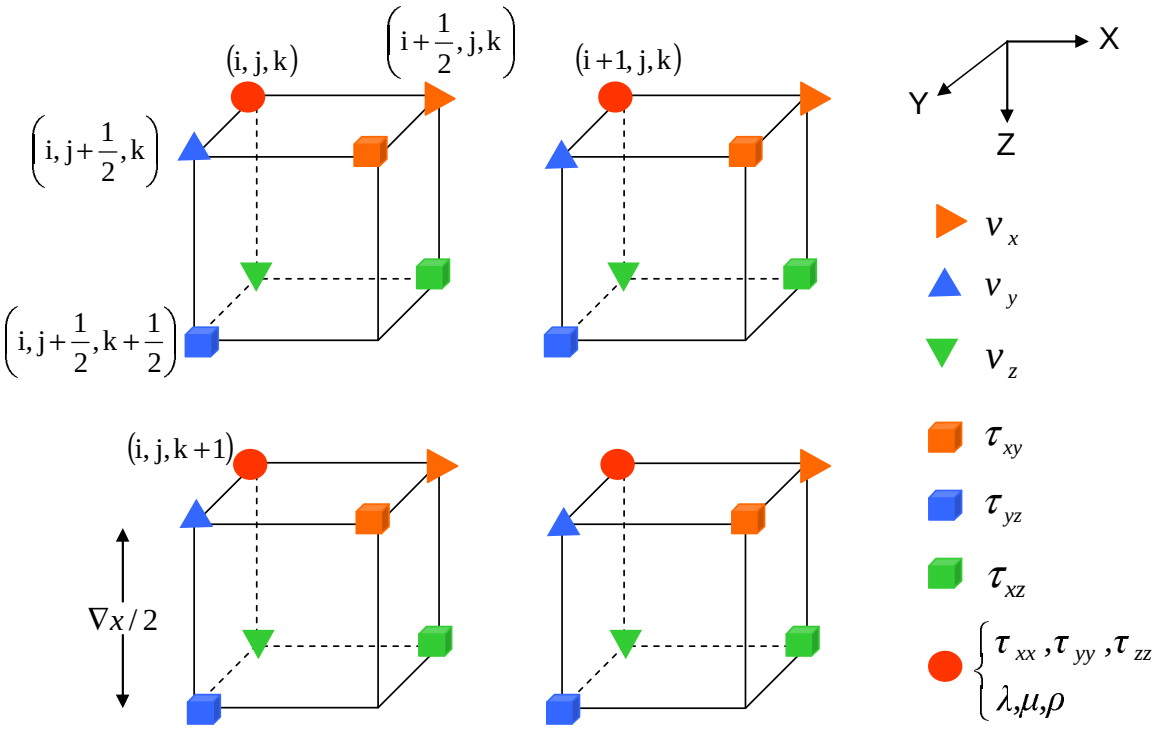

Fig. 53. Other staggered-grid formulation for 3D finite-difference modeling. (a) The indices (i, j, k) represent values at spatial coordinates (x, y, z) and the grid spacing Δx is defined as the length between the centers of two adjacent grids. The wavefield variables and media parameters are defined at a specific grid in a unit cell, the model space is make up of series of repeated unit cells that occupy a 3D space. Not all quantities are defined at the reference grid. The normal stresses τ_{xx}, τ_{yy}, τ_{zz} are defined at the reference grid, the horizontal component of particle velocity v_x is defined at half a grid off the reference grid on the X axis, the shear stress τ_{yz} is defined at half a grid off the reference grid on the X and Z axis. Notice that normal stresses, mass density, and the Lamé parameters are located at the same points.

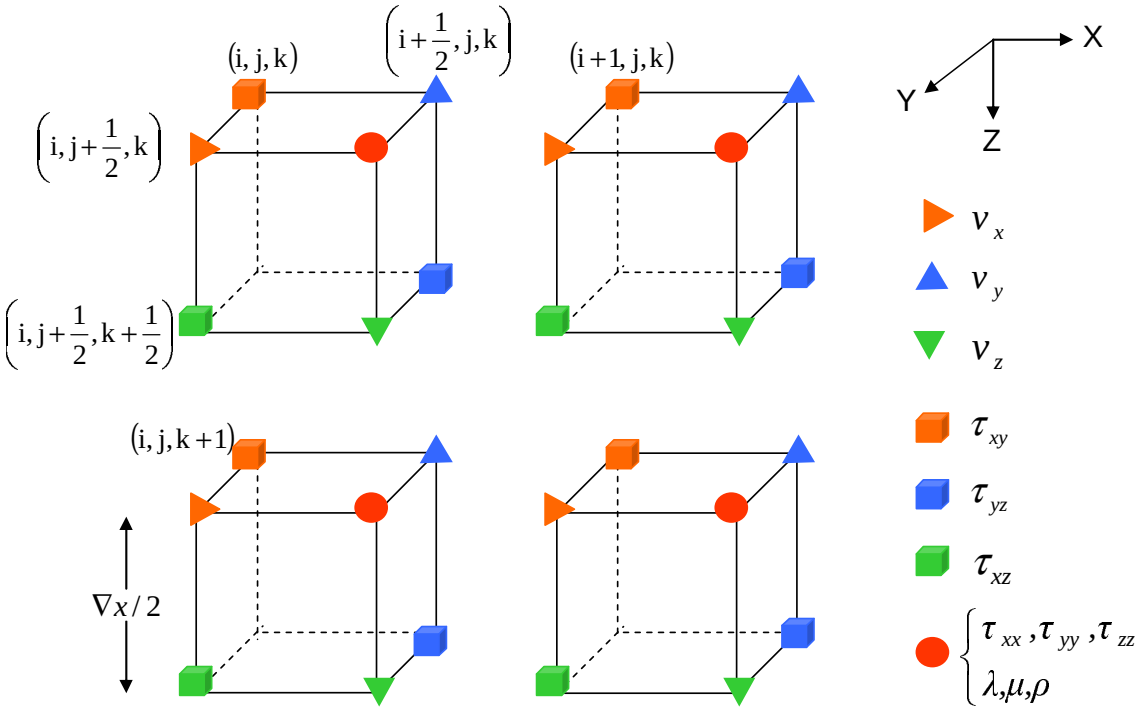

Fig. 53. (b) The indices (i, j, k) represent values at spatial coordinates (x, y, z) and the grid spacing Δx is defined as the length between the centers of two adjacent grids. The wavefield variables and media parameters are defined at a specific grid in a unit cell, the model space is make up of series of repeated unit cells that occupy a 3D space. Not all quantities are defined at the reference grid. The shear stress τ_{xy} is defined at the reference grid, the horizontal component of particle velocity v_x is defined at half a grid off the reference grid on the Y axis, the normal stresses τ_{xx}, τ_{yy}, τ_{zz} are defined at half a grid off the reference grid on the X and Y axis. Notice that normal stresses, mass density, and the Lamé parameters are located at the same points.

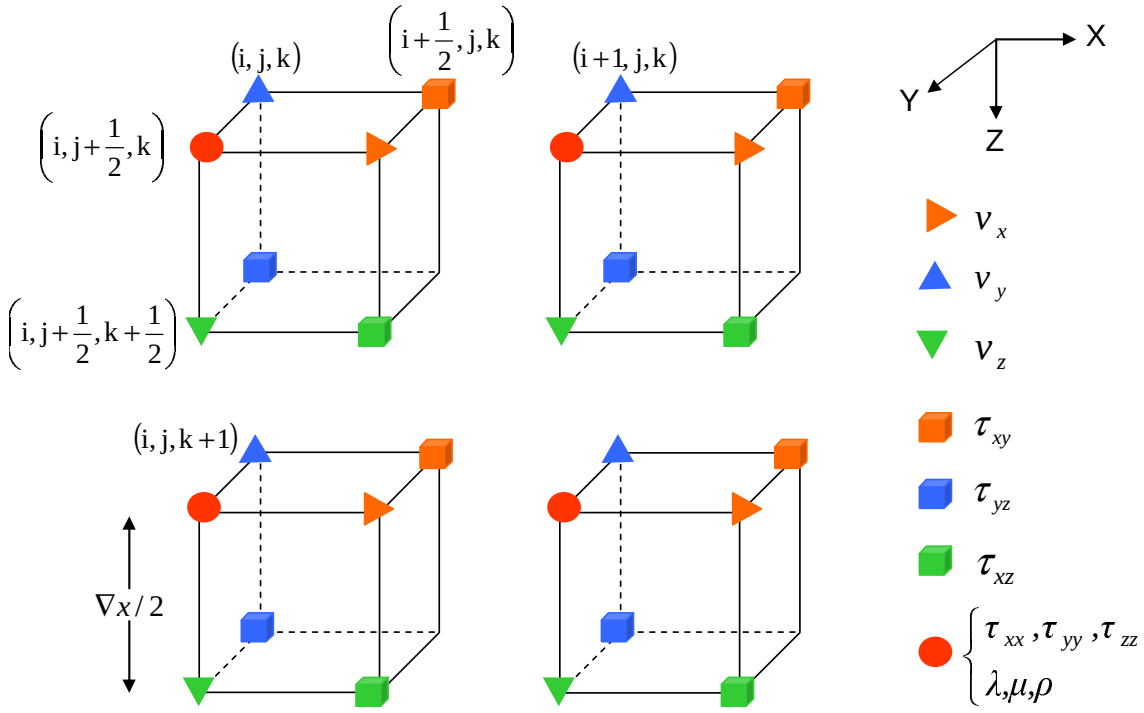

Fig. 53. (c) The indices (i, j, k) represent values at spatial coordinates (x, y, z) and the grid spacing Δx is defined as the length between the centers of two adjacent grids. The wavefield variables and media parameters are defined at a specific grid in a unit cell, the model space is make up of series of repeated unit cells that occupy a 3D space. Not all quantities are defined at the reference grid. The horizontal component of particle velocity v_y is defined at the reference grid, the shear stress τ_{xy} is defined at half a grid off the reference grid on the X axis, the normal stresses τ_{xx}, τ_{yy}, τ_{zz} are defined at half a grid off the reference grid on the y axis. Notice that normal stresses, mass density, and the Lamé parameters are located at the same points.

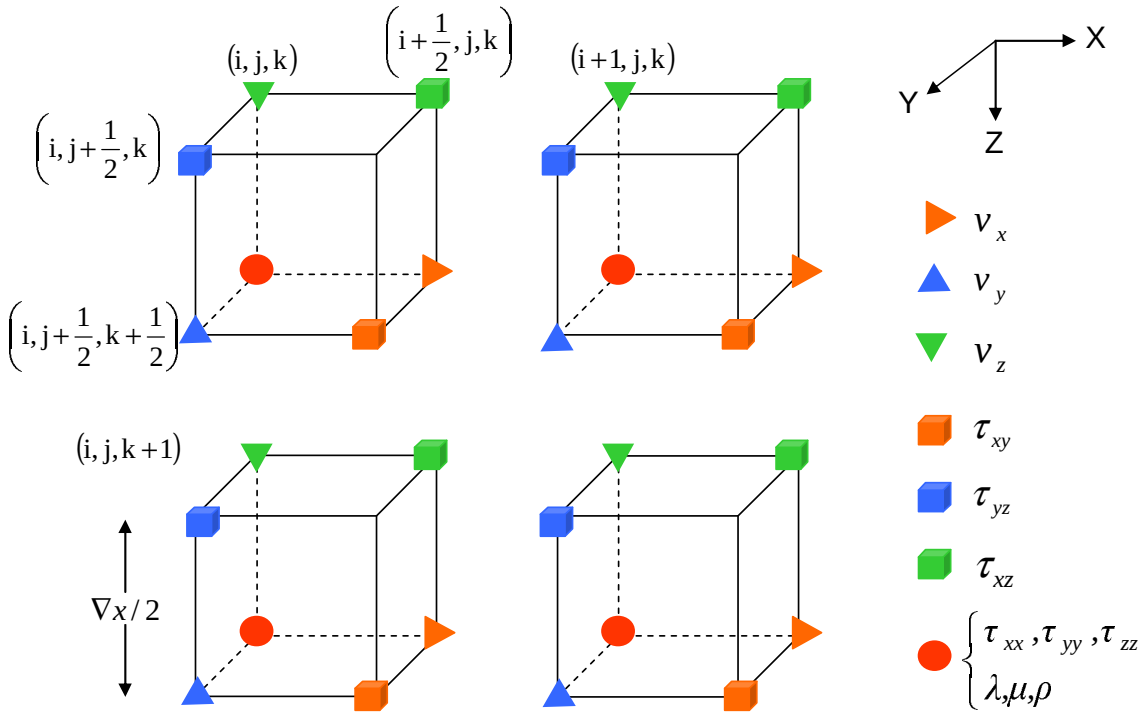

Fig. 53. (d) The indices (i, j, k) represent values at spatial coordinates (x, y, z) and the grid spacing Δx is defined as the length between the centers of two adjacent grids. The wavefield variables and media parameters are defined at a specific grid in a unit cell, the model space is make up of series of repeated unit cells that occupy a 3D space. Not all quantities are defined at the reference grid. The vertical component of particle velocity v_z is defined at the reference grid, the shear stress τ_{xz} is defined at half a grid off the reference grid on the X axis, the normal stresses τ_{xx}, τ_{yy}, τ_{zz} are defined at half a grid off the reference grid on the Z axis. Notice that normal stresses, mass density, and the Lamé parameters are located at the same points.

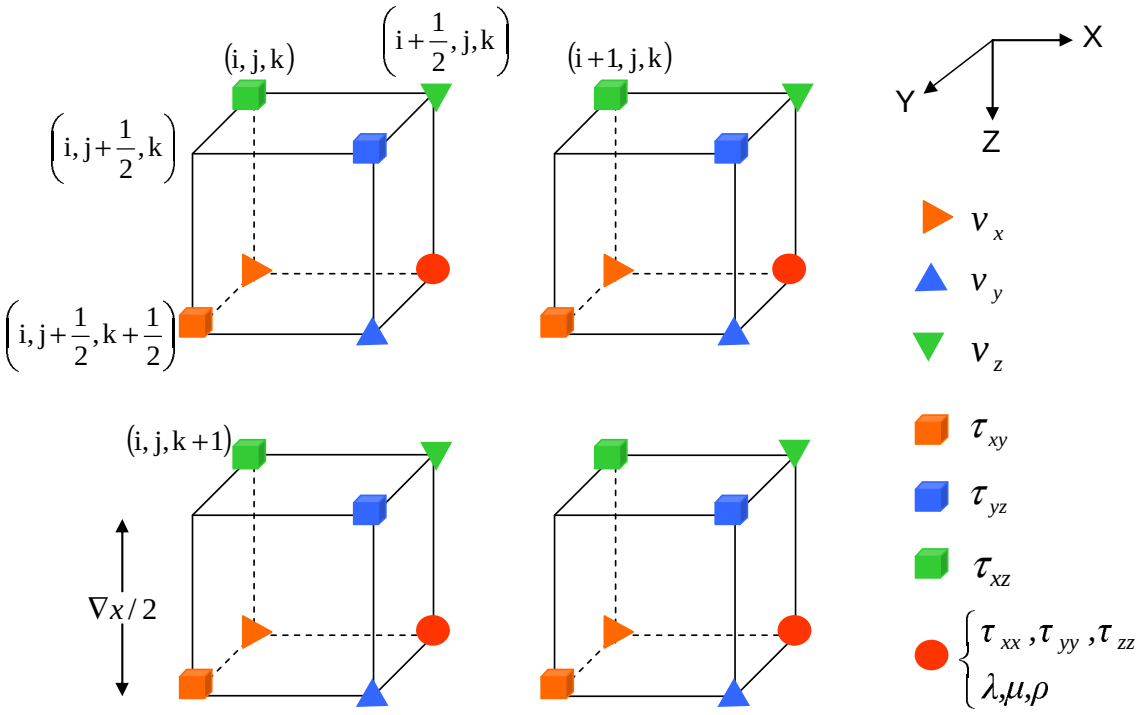

Fig. 53. (e) The indices (i, j, k) represent values at spatial coordinates (x, y, z) and the grid spacing Δx is defined as the length between the centers of two adjacent grids. The wavefield variables and media parameters are defined at a specific grid in a unit cell, the model space is make up of series of repeated unit cells that occupy a 3D space. Not all quantities are defined at the reference grid. The shear stress τ_{xz} is defined at the reference grid, the vertical component of particle velocity v_z is defined at half a grid off the reference grid on the X axis, the normal stresses τ_{xx}, τ_{yy}, τ_{zz} are defined at half a grid off the reference grid on the X and Z axis. Notice that normal stresses, mass density, and the Lamé parameters are located at the same points.

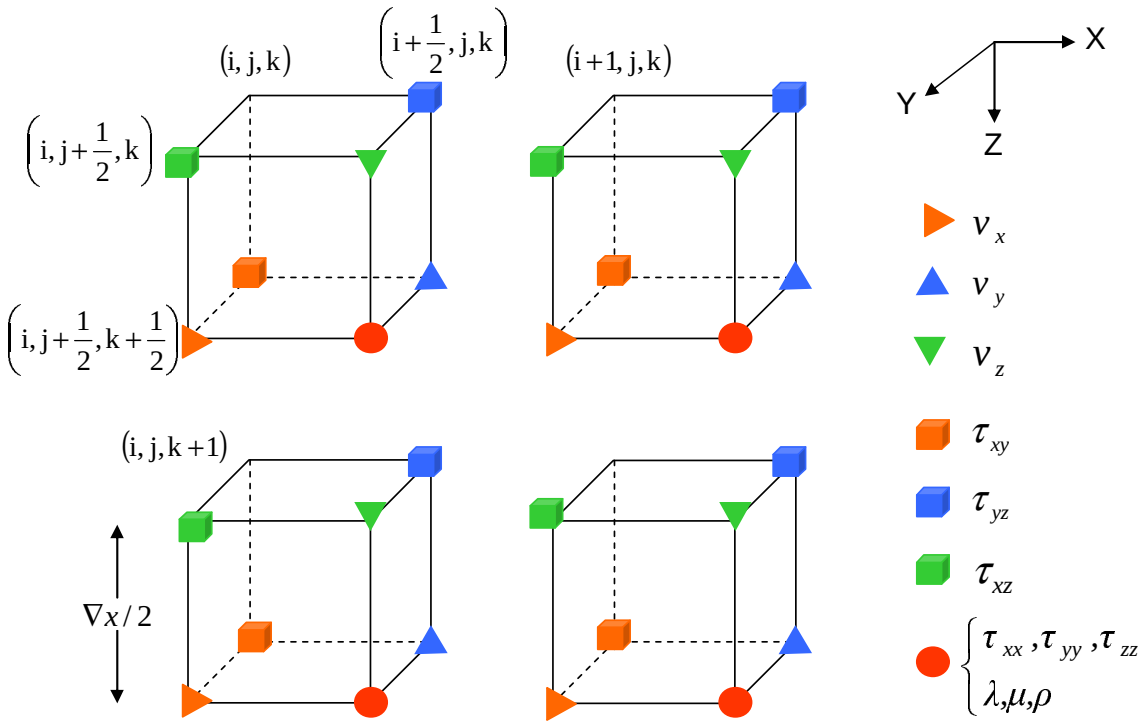

Fig. 53. (f) The indices (i, j, k) represent values at spatial coordinates (x, y, z) and the grid spacing Δx is defined as the length between the centers of two adjacent grids. The wavefield variables and media parameters are defined at a specific grid in a unit cell, the model space is make up of series of repeated unit cells that occupy a 3D space. Not all quantities are defined at the reference grid. The horizontal component of particle velocity v_x is defined at half a grid off the reference grid on the Y and Z axis, the shear stress τ_{yz} is defined at half a grid off the reference grid in x axis, the normal stresses τ_{xx}, τ_{yy}, τ_{zz} are defined at half a grid off the reference grid. Notice that normal stresses, mass density, and the Lamé parameters are located at the same points.

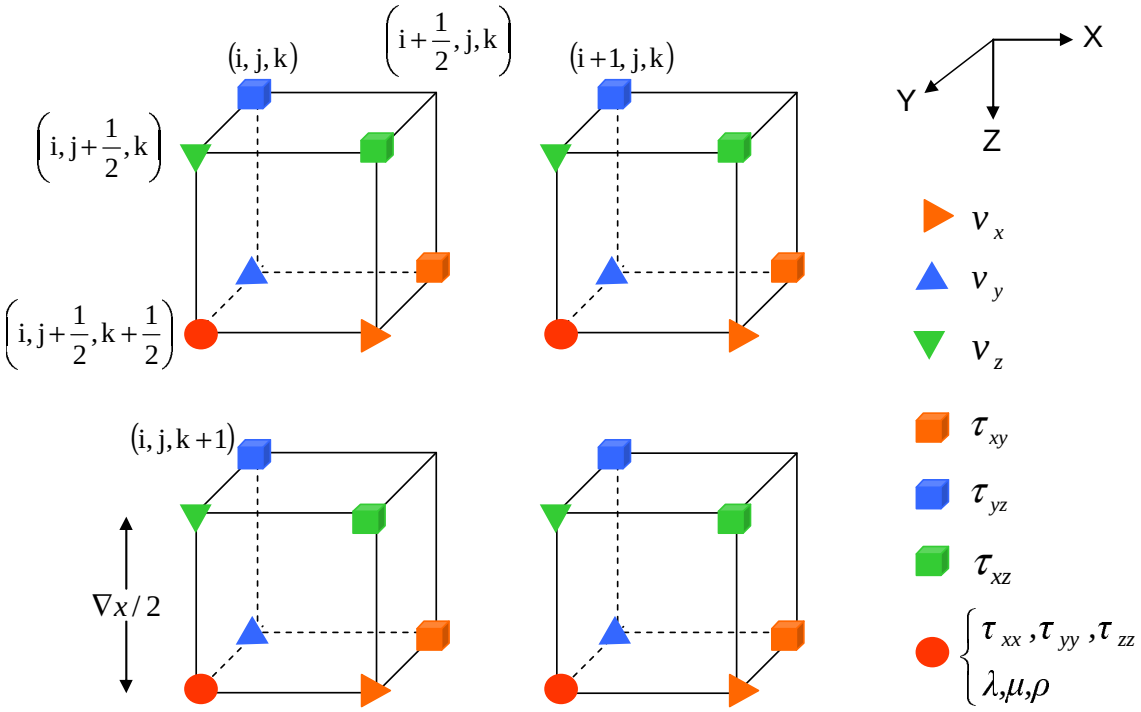

Fig. 53. (g) The indices (i, j, k) represent values at spatial coordinates (x, y, z) and the grid spacing Δx is defined as the length between the centers of two adjacent grids. The wavefield variables and media parameters are defined at a specific grid in a unit cell, the model space is make up of series of repeated unit cells that occupy a 3D space. Not all quantities are defined at the reference grid. The shear stress τ_{yz} is defined at the reference grid, the vertical component of particle velocity v_z is defined at half a grid off the reference grid on the Y axis, the normal stresses τ_{xx}, τ_{yy}, τ_{zz} are defined at half a grid off the reference grid on the Y and Z axis. Notice that normal stresses, mass density, and the Lamé parameters are located at the same points.

APPENDIX C

NUMERICAL ILLUSTRATION OF THE KIRCHHOFF SCATTERING INTEGRAL OVER S_R

Our goal in this appendix is to numerically demonstrate that the Sommerfeld's radiation boundary condition is not valid for the correlation-type representation theorem [i.e., the Kirchhoff scattering integral over S_R (see Figure 28) in (3) is nonzero]. We will also validate the simplification the Kirchhoff scattering integral that we made in (5.22).

We consider the acoustic model in Figure 54. The density is kept constant throughout the model. The dotted lines describe the surface $S = S_0 + S_R$, over which the Kirchhoff scattering integrals are carried out. For the convolution-type representation theorem, the specific integrals are computed as follows:

$$P_{S0}(\mathbf{x}_r, \omega; \mathbf{x}_s) = \int_{S_0} dS(\mathbf{x}) \left[P_P(\mathbf{x}, \omega; \mathbf{x}_r) \frac{\partial P_0(\mathbf{x}, \omega; \mathbf{x}_s)}{\partial n} - P_0(\mathbf{x}, \omega; \mathbf{x}_s) \frac{\partial P_P(\mathbf{x}, \omega; \mathbf{x}_r)}{\partial n} \right] \tag{C.1}$$

and

$$P_{SR}(\mathbf{x}_r, \omega; \mathbf{x}_s) = \int_{S_R} dS(\mathbf{x}) \left[P_P(\mathbf{x}, \omega; \mathbf{x}_r) \frac{\partial P_0(\mathbf{x}, \omega; \mathbf{x}_s)}{\partial n} - P_0(\mathbf{x}, \omega; \mathbf{x}_s) \frac{\partial P_P(\mathbf{x}, \omega; \mathbf{x}_r)}{\partial n} \right] . \tag{C.2}$$

The results of our computations of quantities are shown in Figure 55 for the case in which $\mathbf{x}_r = \mathbf{x}_s$. We used the finite-difference modeling technique to determine the various quantities needed in the computation of these integrations. More precisely, we used the finite-difference modeling technique with the model in Figure 54 containing the free surface in order to generate the data $P_0(\mathbf{x}, \omega; \mathbf{x}_s)$ and $\partial P_0(\mathbf{x}, \omega; \mathbf{x}_s)/\partial n$ for 900 receivers distributed along the surface S. The spacing between receivers is 10 m. The computations of the other two quantities, $P_P(\mathbf{x}, \omega; \mathbf{x}_r)$ and $\partial P_P(\mathbf{x}, \omega; \mathbf{x}_r)/\partial n$,

were also carried out by the finite-difference modeling technique but this time with the model in Figure 54 without the free surface. As we can see in Figure 55(ab), the contribution of the integral over S_0 is about 10^6 greater than that of the integral over S_R. This result confirms that the Sommerfeld's radiation boundary condition is valid in the case of the convolution-type representation theorem.

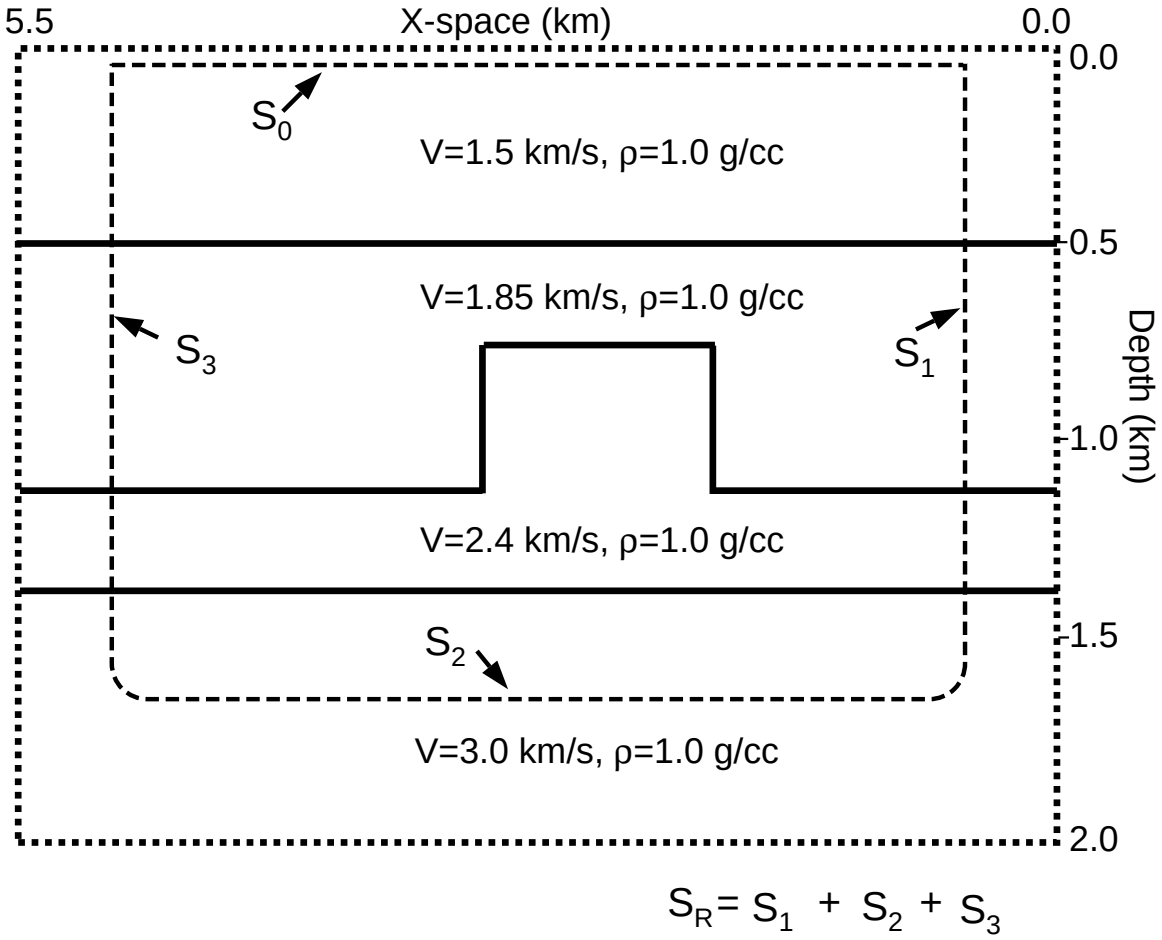

Fig. 54. Acoustic model used to generate the data shown in Figures 36, 37, and 38. The density is kept constant at 1000.0 kg/m^3. The dotted line is the surface $S = S_0 + S_R$, over which the Kirchhoff scattering integrals are carried out. The points $\mathbf{x}_s$ and $\mathbf{x}_r$ invoked in the computations of these integrals are both located at ($x = 2.75$ km, $z = 10$ m) inside the area bounded by the surface S.

To verify the accuracy of the computations we have just described, we also directly computed data $P_0(\mathbf{x}_r, \omega; \mathbf{x}_s)$ and $P_P(\mathbf{x}_r, \omega; \mathbf{x}_s)$ and compared their differences;

i.e.,

$$P_D(\mathbf{x}_r,\omega;\mathbf{x}_s) = P_0(\mathbf{x}_r,\omega;\mathbf{x}_s) - P_P(\mathbf{x}_r,\omega;\mathbf{x}_s) \ , \tag{C.3}$$

with the Kirchhoff scattering integral

$$P_S(\mathbf{x}_r,\omega;\mathbf{x}_s) = \frac{\sigma_0}{s(\omega)} P_{S0}(\mathbf{x}_r,\omega;\mathbf{x}_s) \ . \tag{C.4}$$

As illustrated in Figure 55(cde), P_D is almost indistinguishable from P_S, as one might expect.

Let us now turn to the correlation-type representation theorem. To confirm that this theorem does not satisfy the Sommerfeld's radiation boundary condition, we computed the following integrals:

$$P'_{S0}(\mathbf{x}_r,\omega;\mathbf{x}_s) = \int_{S_0} dS(\mathbf{x}) \left[P^*_P(\mathbf{x},\omega;\mathbf{x}_r) \frac{\partial P_0(\mathbf{x},\omega;\mathbf{x}_s)}{\partial n} + P_0(\mathbf{x},\omega;\mathbf{x}_s) \frac{\partial P^*_P(\mathbf{x},\omega;\mathbf{x}_r)}{\partial n} \right] \tag{C.5}$$

and

$$P'_{SR}(\mathbf{x}_r,\omega;\mathbf{x}_s) = \int_{S_R} dS(\mathbf{x}) \left[P^*_P(\mathbf{x},\omega;\mathbf{x}_r) \frac{\partial P_0(\mathbf{x},\omega;\mathbf{x}_s)}{\partial n} + P_0(\mathbf{x},\omega;\mathbf{x}_s) \frac{\partial P^*_P(\mathbf{x},\omega;\mathbf{x}_r)}{\partial n} \right] \ . \tag{C.6}$$

The quantities invoked in these integrals were obtained by finite-difference modeling, as we described earlier in the case of the convolution-type representation theorem. As we can see in Figure 56(ab), the contribution of the integral over S_R is not at all negligible compared to that of the integral over S_0. Actually, all the events in positive time, and even some negative-time events near $t = 0$, will be significantly erroneous if we were to neglect the contribution of the integral of S_R; only the noncausal primaries located in negative time would be accurate. In other words, the Sommerfeld's radiation boundary condition does not apply in the case of the correlation-type representation theorem.

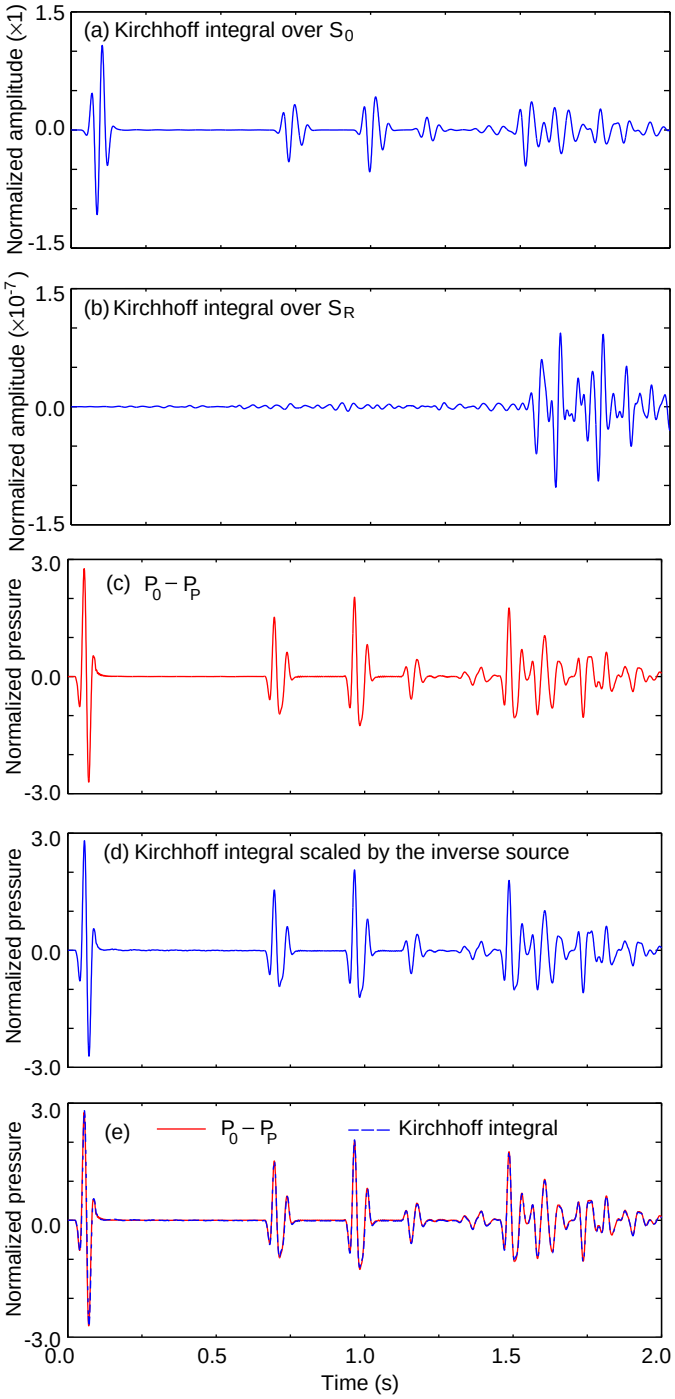

Fig. 55. Validation of Sommerfeld's radiation-boundary condition for the convolution–type representation theorem. (a) The Kirchhoff integral over S_0 [i.e., P_{S0}, equation (C.1)]; (b) the Kirchhoff integral over S_R [i.e., P_{SR}, equation (C.2)]; (c)$P_D = P_0 - P_P$ [see equation (C.3)], in which P_0 and P_P are data computed by the finite-difference modeling technique for the model in Figure 54 with and without a free surface, respectively; (d) the Kirchhoff integral over S_0, scaled by the inverse source signature [i.e., P_S in equation (C.4)]; (e) the superposition of P_D on P_S.

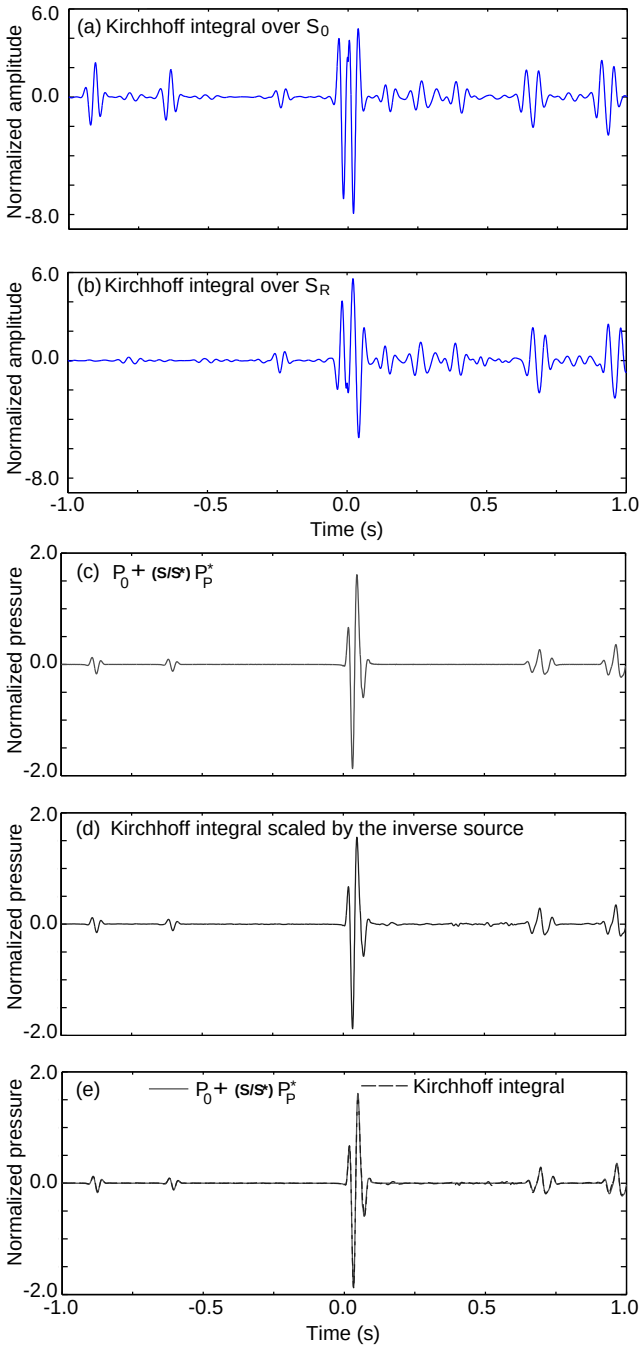

Fig. 56. Confirmation that the Sommerfeld's radiation-boundary condition is not valid for the correlation-type representation theorem. (a) The Kirchhoff integral over S_0 [i.e., P'_{S0}, equation (C.5)]; (b) the Kirchhoff integral over S_R [i.e., P'_{SR}, equation (C.6)]; (c) $P'_D = P_0 + (s/s^*)P_P^*$ [see equation (C.7)] in which P_0 and P_P are data computed by the finite-difference modeling technique for the model in Figure 54 with and without a free surface, respectively; (d) the Kirchhoff integral over S_0, scaled by the inverse source signature [i.e., P'_S in equation (C.8)]; (e) the superposition of P'_D on P'_S.

We have also verified the accuracy of the computations in Figure 56(cde) by comparing the field P'_D, defined as follows:

$$P'_D(\mathbf{x}_r, \omega; \mathbf{x}_s) = P_0(\mathbf{x}_r, \omega; \mathbf{x}_s) + \frac{s(\omega)}{s^*(\omega)} P^*_P(\mathbf{x}_r, \omega; \mathbf{x}_s) \ , \tag{C.7}$$

with the Kirchhoff scattering integral

$$P'_S(\mathbf{x}_r, \omega; \mathbf{x}_s) = \frac{\sigma_0}{s^*(\omega)} \left[P'_{S0}(\mathbf{x}_r, \omega; \mathbf{x}_s) + P'_{SR}(\mathbf{x}_r, \omega; \mathbf{x}_s) \right] \ . \tag{C.8}$$

As illustrated in Figure 56(cde), P'_D is again almost indistinguishable from P'_S, as one might expect.

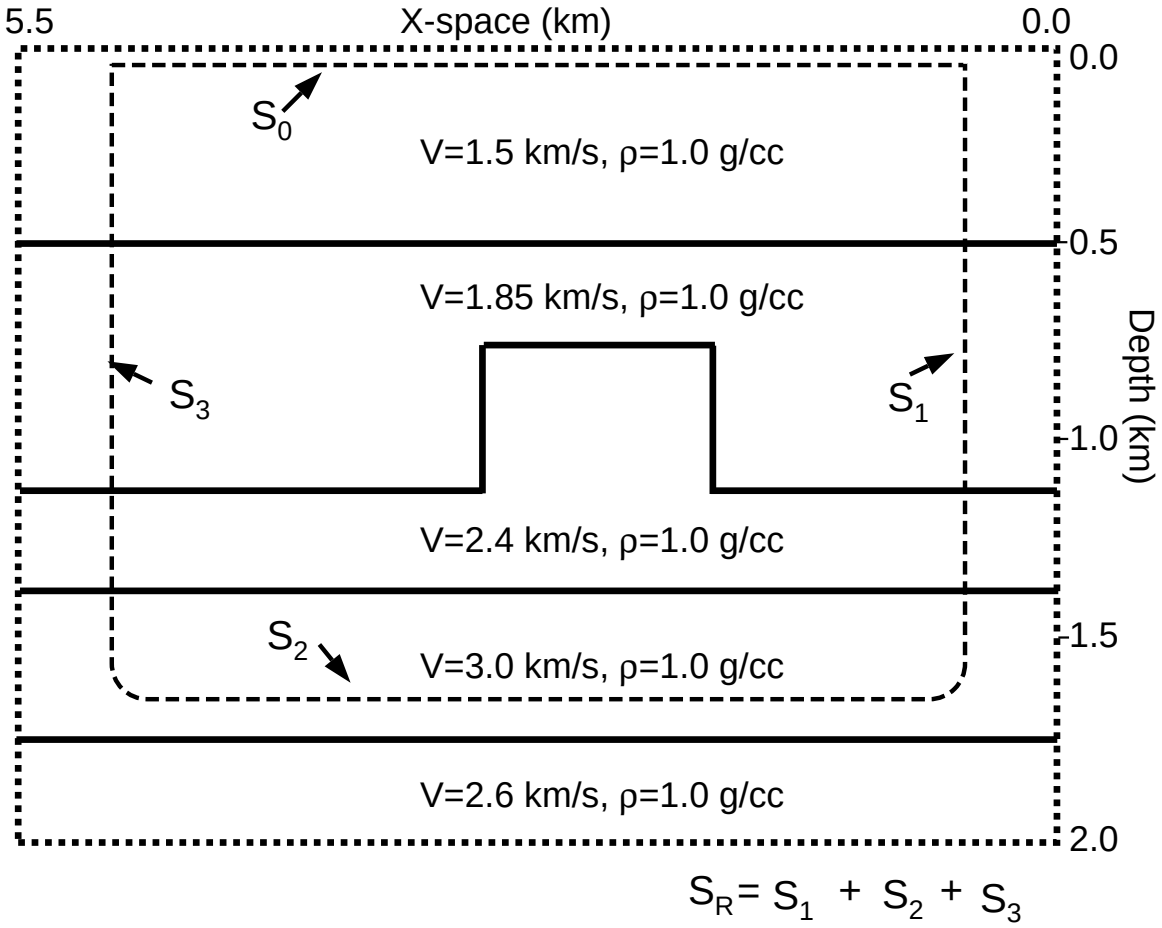

Fig. 57. One of the acoustic model used to generate the data shown in Figure 58; the other acoustic model is given in Figure 54. Notice that there is a reflector below S_2, whereas there is no reflector below S_2 in the model in Figure 54.

Let us now turn to the simplification that we made when passing from (5.22) to (5.23). We will use the models in Figures 54 and 57 to validate this simplification. Notice that in these two models we have divided the surface S_R into S_1, S_2, and S_3. Our discussion focuses on the correlation-type Kirchhoff integral over S_2. In fact, the difference between the two models in Figure 54 is that in Figure 57, there is a reflector below S_2 in Figure 57, whereas in Figure 54, there is no reflector below S_2. In other words, receivers located on S_2 will record both upgoing and downgoing in the case of the model in Figure 57, whereas in the case of the model in Figure 54, receivers will only record downgoing waves.

We computed the following integrals for the two models:

$$P'_{S2}(\mathbf{x}_r,\omega;\mathbf{x}_s)=\int_{S_2} dS(\mathbf{x})\left[P^*_P(\mathbf{x},\omega;\mathbf{x}_r)v_3(\mathbf{x},\omega;\mathbf{x}_s)+P_0(\mathbf{x},\omega;\mathbf{x}_s)v^*_{3(P)}(\mathbf{x},\omega;\mathbf{x}_r)\right] \tag{C.9}$$

and

$$\hat{P}'_{S2}(\mathbf{x}_r,\omega;\mathbf{x}_s)=2\int_{S_2} dS(\mathbf{x})\left[P^*_P(\mathbf{x},\omega;\mathbf{x}_r)v_3(\mathbf{x},\omega;\mathbf{x}_s)\right] \quad , \tag{C.10}$$

where

$$-i\omega v_3=\sigma_0\frac{\partial P_0(\mathbf{x},\omega;\mathbf{x}_s)}{\partial z} \tag{C.11}$$

$$-i\omega v_{3(P)}=\sigma_0\frac{\partial P_P(\mathbf{x},\omega;\mathbf{x}_r)}{\partial z} \ , \tag{C.12}$$

and where σ_0 is the specific associated with the models in Figures 54 and 57. The quantities invoked in these integrals were obtained by finite-difference modeling, as we described earlier. The results in Figure 58 show that P'_{S2} and $\hat{P}'_{S2}$ equals only for the model without the reflector below the surface S_2. So when passing (C.9) to (C.10), we have assume that R go to infinity which is the equivalent of assuming that the receivers located on S_R record only downgoing waves; therefore our simplification

in (5.23) is correct.

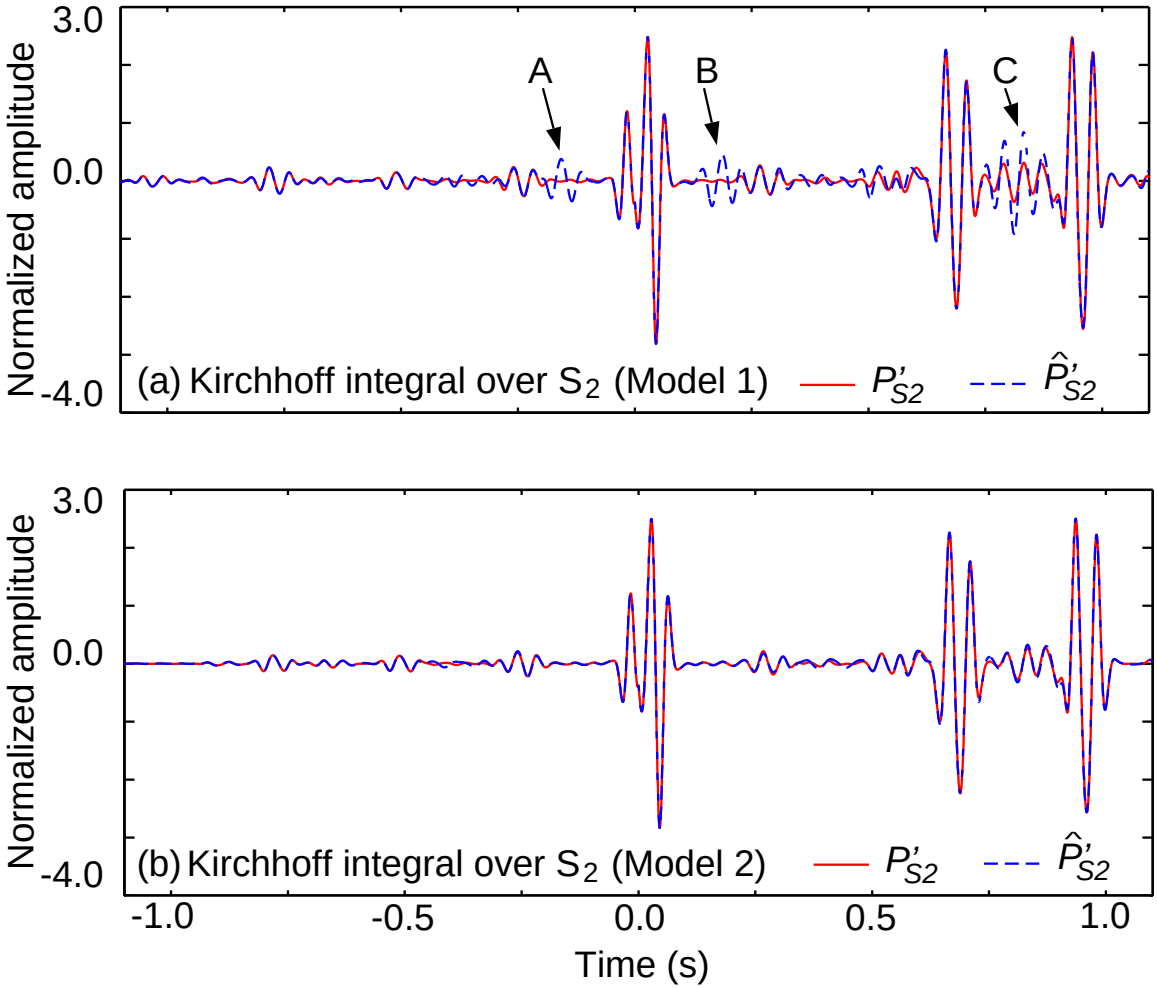

Fig. 58. The two forms of Kirchhoff integrals. (a) The two forms of Kirchhoff integrals over S_2 in equations (C.9) and (C.10) [i.e., P'_{S2} in equation (C.9), and $\hat{P}'_{S2}$ in equation (C.10)] for the model in Figure 57 (Model 1), which has a reflector below S_2. We pointed out by A, B, and C three examples of places where the two formulae differ. (b) The two forms of Kirchhoff integrals over S_2 in equation (C.9) and (C.10) for the model in Figure 54 (Model2), which has no reflector below S_2. So when passing from (C.9) and (C.10), we have to assume that R goes to infinity, which is the equivalent of assuming that the receivers located on S_R record only downgoing waves.

We can also show that (C.9) reduces to (C.10) by using scattering diagrams as (Ikelle and Amundson, 2005) (pages 441-442) did for a similar demonstration in the case of the convolution-type Kirchhoff integral. Figures 59(a) and 59(b) show that the scattering diagrams for the construction of P'_{S2} for two models: one model with

a reflector below S_2 and the other model without reflector below S_2. The signs convention adopted in these figures is as follows: the upgoing and downgoing events of pressure fields are assigned positive signs; the downgoing events of the vertical component of the particle are also assigned positive signs, whereas the upgoing events of the vertical component of the particle are assigned negative signs. This nomenclature is consistent with the basic relationship between the pressure field and the vertical component of the particle velocity.

By comparing the polarity of the events created by the multidimensional correlation of $P_P(\mathbf{x}, \omega, \mathbf{x}_r)$ and $v_3(\mathbf{x}, \omega, \mathbf{x}_s)$ with the events created by the multidimensional correlation of $P_0(\mathbf{x}, \omega, \mathbf{x}_s)$ and $v_{3(P)}(\mathbf{x}, \omega, \mathbf{x}_r)$, we can see these two multidimensional correlations are identical for the model without reflector below S_2 and they are different for the model with a reflector below S_2. Therefore, the scattering diagrams confirm the results in Figure 58.

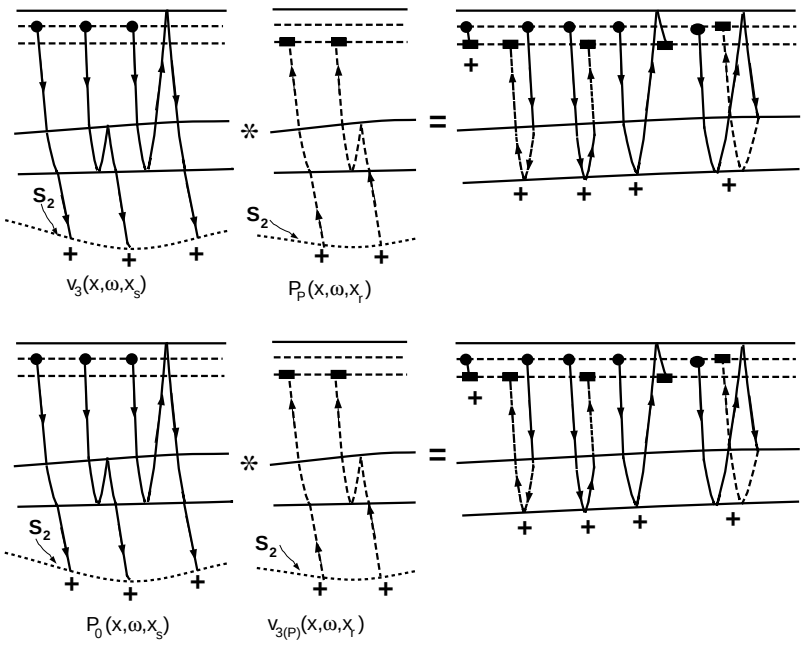

(a)

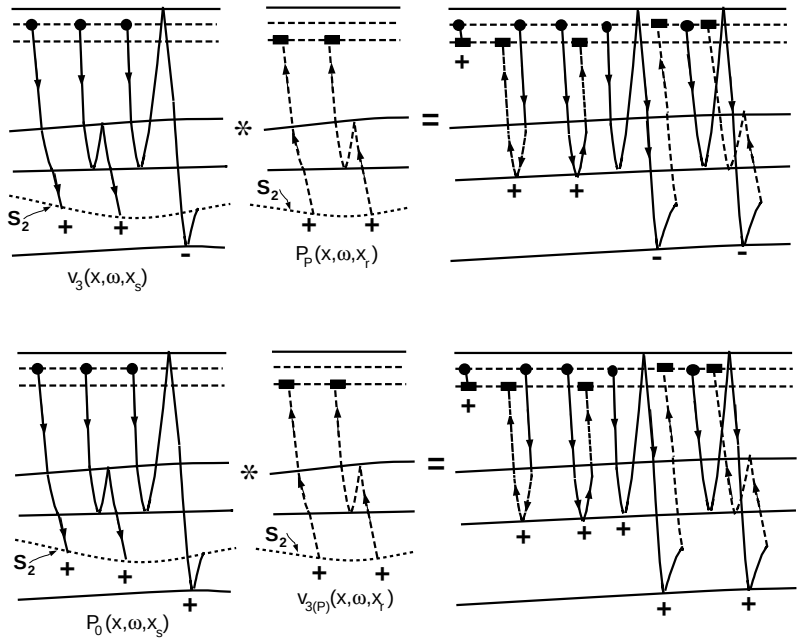

(b)

Fig. 59. A comparison of the scattering diagrams. A comparison of the scattering diagrams of the multidimensional correlation of $P_P(\mathbf{x}, \omega, \mathbf{x}_r)$ and $v_3(\mathbf{x}, \omega, \mathbf{x}_s)$ in equation (C.9) with those of the multidimensional correlation of $P_0(\mathbf{x}, \omega, \mathbf{x}_s)$ and $v_{3(P)}(\mathbf{x}, \omega, \mathbf{x}_r)$. (a) For the model without a reflector below S_2, these two multidimensional correlations are identical. (b) For the model with a reflector below S_2, the two multidimensional correlations are different.

VITA

Name: Xiujun Yang

Address: TAMU 3115

College Station, TX, 77843-3115

Email: xiujun.yang@gmail.com

Education: B.S., Geophysics, University of Science and Technology of China, Hefei, Anhui, 2001

M.S., Geophysics, Indiana University, Bloomington, IN, 2004

Ph.D., Geophysics, Texas A&M University, College Station, TX, 2008